ABSTRACT

Title of Document:	INDIVIDUAL AND COLLECTIVE DYNAMICS OF CHEMOTAXING CELLS
	Colin Patrick McCann Doctor of Philosophy, 2011
Directed By:	Professor Wolfgang Losert Department of Physics

The study of the dynamics of interacting self-propelled entities is a growing area of physics research. This dissertation investigates individual and collective motion of the eukaryote *Dictyostelium discoideum*, a system amenable to signal manipulation, mathematical modeling, and quantitative analysis. In the wild, *Dictyostelium* survive adverse conditions through collective behaviors caused by secreting and responding to chemical signals. We explore this collective behavior on size scales ranging from subcellular biochemistry up to dynamics of thousands of communicating cells.

To study how individual cells respond to multiple signals, we perform stability analysis on a previously-developed computational model of signal sensing. Polarized cells are linearly stable to perturbations, with a least stable region at about 60 degrees off the polarization axis. This finding is confirmed through simulations of the model response to additional chemical signals. The off-axis sensitivity suggests a

mechanism for previously observed zig-zag motion of real cells randomly migrating or chemotaxing in a linear gradient.

Moving up in scale, we experimentally investigate the rules of cell motion and interaction in the context of thousands of cells. Migrating *Dictyostelium discoideum* cells communicate by sensing and secreting directional signals, and we find that this process leads to an initial signal having an increased spatial range of an order of magnitude. While this process steers cells, measurements indicate that intrinsic cell motility remains unaffected. Additionally, migration of individual cells is unaffected by changing cell-surface adhesion energy by nine orders of magnitude, showing that individual motility is a robust process. In contrast, we find that collective dynamics depend on cell-surface adhesion, with greater adhesion causing cells to form smaller collective structures.

Overall, this work suggests that the underlying migration ability of individual *Dictyostelium* cells operates largely independent of environmental conditions. Our gradient-sensing model shows that polarized cells are stable to small perturbations, and our experiments demonstrate that the motility apparatus is robust to considerable changes in cell-surface adhesion or complex signaling fields. However, we find that environmental factors can dramatically affect the collective behavior of cells, emphasizing that the laws governing cell-cell interaction can change migration patterns without altering intrinsic cell motility.

INDIVIDUAL AND COLLECTIVE DYNAMICS OF CHEMOTAXING CELLS

By

Colin Patrick McCann

Dissertation submitted to the Faculty of the Graduate School of the
University of Maryland, College Park, in partial fulfillment
of the requirements for the degree of
Doctor of Philosophy
2011

Advisory Committee:
Professor Wolfgang Losert, Chair
Professor Michael Fisher
Professor John Fourkas, Dean's Representative
Adjunct Professor Carole Parent
Professor Arpita Upadhyaya

Acknowledgements

My advisors, Drs. Wolfgang Losert and Carole Parent, were a tremendous help in generating research ideas and insight, providing guidance, helping with presentations, and all the other thousand things that advisors do for their students. I owe them a tremendous debt of gratitude. Their collaboration between physics and biology brings together strengths from different fields; and it has been exciting working at that interface.

Bridging two disciplines brings you into contact with many people, and I have been very fortunate to make the acquaintances of both good physicists and good biologists. On the University of Maryland side, such people from the Losert lab include Rodica Bauer, Meghan Driscoll, Can Guven, Mark Herrera, Rael Kopace, Eleanor Ory (EchO), Josh Parker, John Platig, Corey Poole, Krisztian Ronaszegi, Steve Slotterback, Xiaoyu Sun, Chenlu Wang, as well as Drs. Beatriz Burrola, Seijin Han, Brian Koss, and Masahiro Toiya. Dr. Ron Skupsky was very obliging in helping me understand his model. Thanks also to Dr. Erin Rericha for guidance and helpful edits and suggestions. Ed Condon, Don Martin, and the IREAP staff keep things running smoothly in the lab. Jane Hessing has always been extremely gracious and helpful, even when I was late filling out forms or otherwise being difficult. Special thanks goes to Dr. Andrew Pomerance for continuing moral, fast-food, and pint support.

Outstanding people at the National Institutes of Health in the Parent Lab include Drs. Anna Bagorda, Frank Comer, Satarupa Das, Gene Garcia, Lunhua Liu, Christina Stuelten, and Michael Weiger. Dr. Paul Kriebel showed me how to work with *Dictyostelium* and has always been a reliable source of advice and friendship. Thanks to Dr. Vidya Vedham for editing and other advice; thanks also to Dr. Mirkka Janka-Junttila for ladybug coffee. Nancy Cruz, Carole Regan, and Dr. Valarie Barr all help ensure that research can get done – thanks

for your work! A big thanks to Dr. Philippe Afonso for great volumes of coffee, cheese, and various types of liquid nutrition that can be found at the Rock Bottom restaurant.

Other people who helped scientifically are Drs. Ralph Nossal, James Warren, and Dan Wheeler. Their expertise and suggestions went a long way in getting the stability analysis work completed, and they were quite friendly and accommodating to a computer science undergrad attempting to become a biophysicist!   Thanks to Dr. Alan Kimmel for the use of his microscope for self-aggregation experiments.

Graduate school can be an extremely difficult place at times, but I have been fortunate beyond all measure in making friendships with people also going through the process. Many of the following people let me ride their coattails through the difficult first-year classes and supported me morally afterwards. Our overtaxed brains gave rise to various short-lived clubs, such as 'D&D Friday' (note: not Dungeons and Dragons!) as well as the notorious 'Pregame Club' (aka "Protect the Homeland"). Sincere gratitude goes to Ryan Artuso, Brian Christy, Dr. Ryan Clary, Dr. Eric Engelson, Dr. Kyle Gustafson and Kate Gardner, Brian Layer, the newly-minted Dr. Chris and Jo Long, Dr. Chris and Angela Stark, and Vitaley Zaretsky. Dr. Nathan Orloff was instrumental in introducing me to pretty much all of these distinguished physicists, for which I still have deep thanks (for that as well as his occasional cooking!). The gang that kept me sane through regular group therapy is Lincoln Allard, Nicholas Boissoneault, Matt Christen, Dr. Brad and Kelly Conrad, Andrew Cutter, Justin Feaster, Peter Redl, and Simon Slutsky. I wouldn't have made it without you guys. Nick Mecholsky provided many long, interesting conversations. Friends who got me through the early days of grad school are Andrew Backhouse, Michael Figueroa, Wanna Sribunnak, and last but certainly not least, Tricia Tierney. Credit is also due to Matt Weaver, who provided many pizza and game nights.

Finally, family and friends have provided a critical bedrock of stability. I am extremely lucky to have a wonderful wife, Amy, who has seen me through all the ups and

downs of graduate school. Thank you! My parents, Eileen and Robert, have always been

there when I needed them. Thanks to my siblings Megan and Matt, and his wife Elizabeth,

for making my too-few visits home good ones. Marie and Buddy Fenstermaker, my in-laws,

have always been welcoming and supportive, as have my wife's sisters Ali and Lorrie, as

well as their husbands Brian and Mike. My friends Jacob and Monica Brunny, Jarrett and

Bethany Brunny, Micah and Jen Lewin, James and Samantha Ream, and Tony and Anitha

Rodriguez have always been, and continue to be, great friends. Thanks to anyone else I've

left out due to my own forgetfulness!

Table of Contents

List of Tables

List of Figures

1. Introduction and Background

In this thesis we examine the dynamics of individual and collective motion in the eukaryote *Dictyostelium discoideum*. This introductory chapter presents the current state of research in the fields of collective cell motion, the cell chemical sensing system, and cell-surface adhesion interactions. In Chapter 2 we investigate the rules of collective motion by performing stability analysis on a model of single-cell chemical sensing. Chapter 3 expands the spatial scale of the research by an order of magnitude and explores the effects of cell-to-cell chemical communication and physical interactions. Chapter 4 investigates how individual and collective behaviors are influenced by the ability of cells to adhere to a surface. Chapter 5 presents an outlook on the implications of these findings and suggests future research directions. Appendix A details the experimental methods and provides an introduction to the software used in this thesis.

1.1. *Overview*

The interaction of individual organisms to produce collective motion is of fundamental importance in nature. In animals, the process of collective motion is often called 'flocking' and applies to a variety of systems, such as birds, insects, fish, cattle, and even humans [1] (see Figure 1.1). Understanding the emergent collective motion that arises from the interactions of individual agents is an area of active research in physics, mathematics, and biology [2]. Studies of the dynamics of collective motion have been able to elucidate interaction laws from in-depth analysis.

This research has led to remarkable discoveries, such as the fact that many locust swarms are driven by cannibalism [3], fish in a school only match others' motion if a threshold number of co-moving neighbors is surpassed [4], and cow herd motion is influenced by a hierarchy, although there is no leader [5]. Furthermore, knowledge of how local interaction laws govern collective motion has many potential applications. For instance, a study on humans showed that a small number of knowledgeable individuals can successfully lead a large group [6], which has implications for emergency management preparation. Also, there is great interest in developing rules for swarms of robots to complete a given task autonomously, such as optimally foraging for objects over a given area [7]. Truly understanding the impact of individual interactions on collective motion requires quantitative mathematical modeling. For example, modeling revealed that swarms can transition between periodic circular motion and straight-line motion depending upon the angle at which individuals respond to one another [8], and the only interactions required for flocks to follow a leader successfully is short-range repulsion and slightly longer-range attraction [9]. In short, the study of collective motion is leading to an understanding of natural systems and the rules that governed them, which will in turn drive future applications.

In addition to animals, groups of cells also interact and display collective motion. For instance, some bacteria transition between individual and collective motion based on their density and external conditions [10]. In mammalian systems, tissues and other cells display collective motion, which is critical in embryogenesis, wound healing, and vascular (blood vessel) growth [11, 12] (see Figure 1.2 A). There
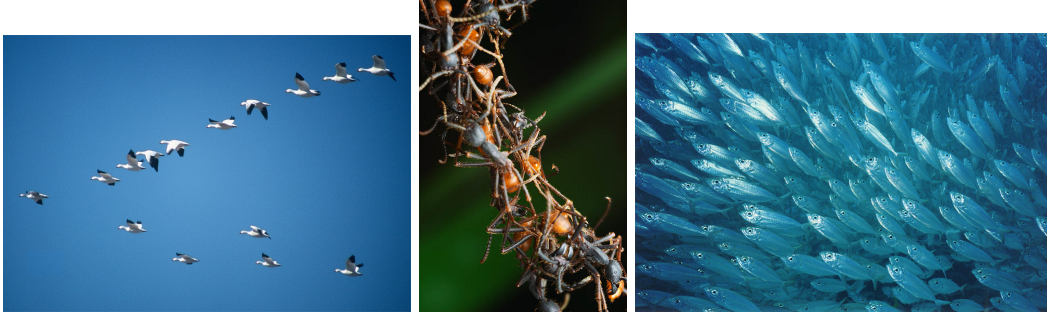
Figure 1.1 – Examples of Collective Animal Motion

Many animal systems perform collective motion, for a variety of reasons. (Left) Geese fly in a 'V' formation to provide energy savings to the flock. (Middle) Ants form bridges with their bodies to allow access to otherwise unreachable locations. (Right) Fish form schools to visually confound predators.
Left image copyright Robyn Waayer (2009) and found at
http://www.sdrp.org/resources/Ecology/Robyn%20Waayer/SnowGeese.jpg.
Middle image copyright Alexander Wild (2004) and found at
http://www.myrmecos.net/ants/EciBur11.JPG. Right image copyright R. Kent
Wenger (2000) and found at
http://pages.cs.wisc.edu/~wenger/images/bonaire2k/school.jpg.
All images reprinted with permission.

is also increasing evidence that collective migration may be important in the response

of immune cells to infection [13]. Finally, group migration plays a role in the

metastasis of a wide range of cancer types [14] (see Figure 1.2 B), such as cancer

cells that move collectively out of a tumor along blood vessels [15] or follow in the

path of a non-cancerous cell [16]. Observations of these processes can lead to

successful inferences regarding the interaction rules that individual cells follow [17].

Cell-cell adhesion, cell-surface adhesion, crawling or swimming speed, cell division

ability, cell internal states, and cell-cell communication via chemical or other signals

all potentially play a role in collective cell motion [15]. Knowledge gained from

these studies has potential applications for therapeutic treatments. For instance, some

bacterial species initiate the infection process through communicating a collective

(A)

(B)
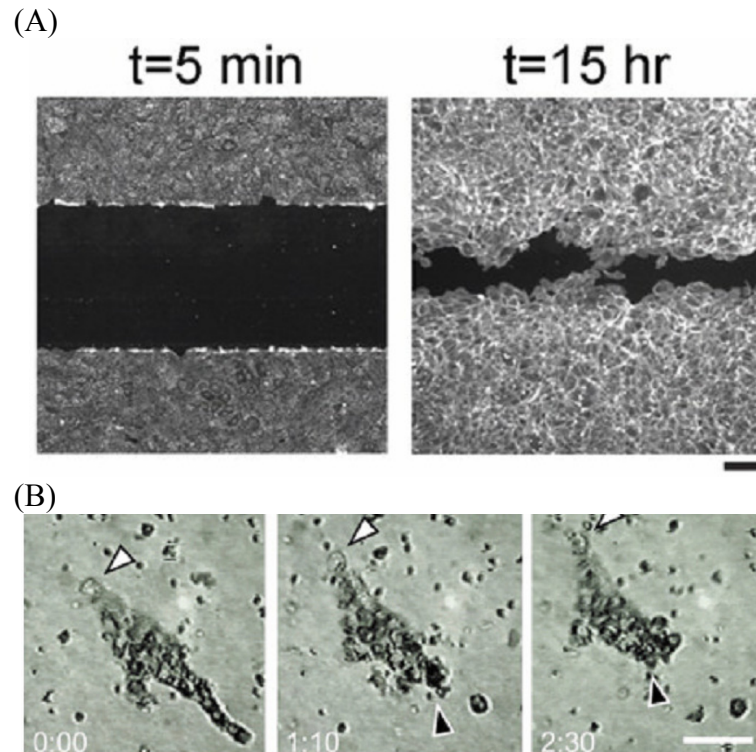
Figure 1.2 – Examples of Collective Cell Motion
(A) A sheet of endothelial cells (gray) collectively migrates to close a gap (black).
Scale bar = 150 μm (image from [17]) (B) A group of oral squamous cell carcinoma
(cancer) cells migrating collectively. Indicated time is in hours. Scale bar = 80 μm
*Reproduced from Fig. 1D of [20], copyright 2004 International Journal of
Developmental Biology (Int. J. Dev. Biol.). Used with permission.*

motion signal [18], and cancer metastasis may be hindered by disruption of cell

adhesion molecules [19].   Collective cell motion is therefore an interesting and

important problem that is worthy of extensive study.

Sensing and responding to chemical signals with directed motion (chemotaxis)

is a driving factor in many collectively migrating cell systems. While in some

instances (e.g. densely-packed bacteria) cell-generated motion through a fluid and

cell-cell repulsion are enough to generate collective behavior [21], in other instances

(e.g. embryogenesis), the ability of cells to communicate with one another via

secreted signals is considered vital [22]. As an example, the collectively migrating

4

cells of the eukaryote *Dictyostelium discoideum* sense a chemical signal in the environment and respond by moving in the direction of the source [23]. These cells begin at too great a distance from one another to communicate effectively using any other method, and they therefore must be able to properly interpret and respond to the cues that their neighbors are secreting into the environment. As another example, cancer cells migrating as an adhered group can act as a single unit to follow chemical signals [15]. Consequently, studying chemotaxis will lead to greater knowledge about collective motion in natural biological systems and cancer.

For a cell to successfully perform chemotaxis, it must be able to transduce an often noisy and shallow external chemical gradient into a strong intracellular biochemical response, which in turn mobilizes its internal structure to cause directed migration. The migration process itself must be spatio-temporally regulated in order to produce the right forces in the correct places and at the proper times to propel the cell in a given direction. The method whereby a cell is able to accomplish this task has been under active investigation for several decades, and the identities and interactions of many of the molecules have been discovered [24]. However, quantitative data on the dynamics of these molecules are still actively being collected, and theoretical models are still not fully consistent with experiments [25]. To better understand these systems, we now provide an overview of the current knowledge of cells, chemotaxis, and group dynamics.

1.2. *An Introduction to Cells and Collective Behavior*

1.2.1. The Cell as a Physical System

A comprehensive treatise on cell biology can be found in Alberts et al [26].

The cell is the fundamental unit of life. Generally, a cell consists of a phospholipid membrane bilayer that separates 'inside' from 'outside'. The cell contains genetic material in the form of DNA, which it uses as a template to create proteins to perform a variety of functions. Cells use various processes to intake and process energy, which they then utilize for various tasks, such as motion, maintenance, intake and excretion of particles, etc. In general, a cell is a vastly complex and regulated system with a variety of functions, and as research progresses the picture of cellular structure and function becomes more and more complex. Entire scientific careers can be spent elucidating a single cellular process in a given cell type.

Ultimately, a cell is also a physical system subject to physical constrains, and it can be understood in physical and chemical terms, e.g. proteins are often enzymes catalyzing reactions with particular rates, structural elements of cells have bending rigidities and elastic properties, cells exert forces on their environment in order to move, and the laws of thermodynamics must be obeyed. Biophysical/biochemical theories and measurements have provided valuable tools to quantify and explain processes of the cell (see Table 1-1). In this vein, this thesis aims to bring quantitative measurements to bear on the physical processes of individual and collective motion.

Table 1-1 – Typical Physical Properties of Cells

Size	0.5 µm (bacteria) – 10 µm (eukaryote)
Young's Modulus	0.01 – 1 GPa
Speed (Crawling)	10 µm/min (eukaryote)
Speed (Swimming)	25 µm/sec (bacteria)
Mass	$1 - 500 *10^{-15}$ kg
Density	1100 kg / m^3
Internal pH [27]	7.3 (cytosol)
Transmembrane Potential	60 mV
Forces Exerted	1 nN

Values (except for pH) are adapted from [28].

1.2.2.   Chemotaxis and Collective Behavior

To understand the collective motion of cells, we must first understand cell-cell communication as well as the rules of cell motion. The primary method of collective behavior in *Dictyostelium discoideum*, as well as in many other cell systems, is a chemotactic response to secreted signals. There are many potential molecular methods of communication, which can vary across cell types or even within an individual cell for different signals [29].

Bacterial cells generally swim up (or down) a chemical gradient via a 'run-and-tumble' mechanism: the cells spin their flagella to move in a straight line when they sense a temporally increasing (or decreasing) concentration of ligand [30]. When the concentration does not increase, they spin their flagella in a way that randomizes their direction, and then they once again switch to moving straight, continuing in that direction longer if the external concentration increases (or decreases). This method leads to overall directed motion, such as towards a source of food or away from harmful conditions [31].

Eukaryotic cells, in contrast, use a different method to sense concentration gradients. Eukaryotic cells in general are larger than prokaryotes such as bacteria (~10 μm versus ~2 μm typical diameter) and are better able to detect spatial concentration differences between their front and back. The sensitivity of some gradient-sensing eukaryotes is high enough to detect front-to-back differences in concentration of ~1% [32]. The cells then are able to amplify this signal to produce a steep concentration gradient of internal molecules, which leads to filamentous actin (F-actin) polymerization in the direction of the signal. This F-actin network generates force to bend the membrane and form protrusions at the cell front, pushing the cell in that direction. In addition, the cell back contracts through the action of molecular motors, resulting in net forward motion [33]. The process of chemotaxis can lead to directed motion in chemical gradients that vary in strength and absolute concentration over many orders of magnitude [34].

Although the identities and interactions of many molecules involved in chemotaxis have been discovered, quantitative data on the dynamics of these molecules are still actively being collected, and theoretical models that accurately reproduce the entire chemotactic process, from gradient sensing to motion, are non-existent [24]. Instead, chemotaxis is often separated into two modules that are more easily tractable: the chemical-sensing module, and the motility module [35]. Generally, the output of the chemical-sensing module feeds into the motility module (and not vice versa). The molecules involved in the chemotactic pathways have been under active investigation for years at the scale of the single cell. However, additional complications arise when cells use a system of chemical release and

sensing as a form of communication to drive a population of cells toward a particular goal. To understand the complexity of the resultant process, we study the soil-dwelling amoeba *Dictyostelium discoideum*, which provides an ideal system to study the individual and group dynamics of collective chemotaxis. In this organism, chemotactic-mediated group migration allows cells to move towards neighbors during starvation conditions to aid in survival. We now provide an introduction to *Dictyostelium discoideum* and highlight the current state of research.

1.2.3. *Dictyostelium discoideum* as a Model System

Studying chemotaxis in mammalian cells is a difficult proposition for many reasons. Experimental conditions must attempt to reproduce the complex environment found in the body, and so extreme care must be taken with factors such as temperature, pH, proteins and nutrients found in the surrounding fluid, specialized materials to place cells upon, etc [36]. For this reason, from a basic science point of view, a system that is well-characterized, hardy, and provides knowledge directly relevant to mammalian cells, without the drawbacks, is desirable.

The soil-dwelling amoeba *Dictyostelium discoideum* is one such system for studying chemotaxis. Officially recognized by the NIH as a "Model Organism for Biomedical Research", *Dictyostelium* chemotaxis uses similar molecular mechanisms as mammalian amoeboid cells, such as neutrophils (a subset of white blood cells) [37, 38]. Research findings in *Dictyostelium* have been shown to be generally applicable to other systems, and experimental work is much easier [39]. Thus, *Dictyostelium* provides a good balance of experimental ease and translatable results. Its genome has
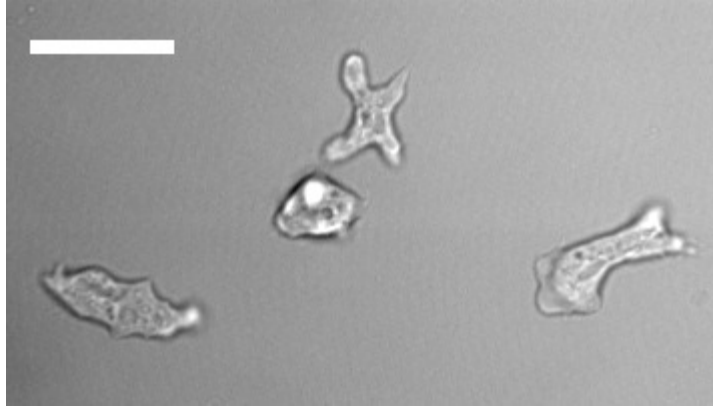
Figure 1.3 – Microscope Image of Individual *Dictyostelium discoideum* Cells
Individual cells as seen under bright-field microscopy. Scale bar = 20 μm.

been sequenced, many stable genetic mutants have been engineered, and it has been actively studied for over 30 years [40].

The physical properties of *Dictyostelium* are similar to those of amoeboid mammalian cells [41]. An individual *Dictyostelium* cell is around 10 μm in diameter and feeds on bacteria. As part of their natural life cycle, *Dictyostelium* cells are able to perform chemotaxis toward a number of chemical signals, such as bacterial byproducts, or the small signaling molecule cyclic adenosine monophosphate (cAMP) [42]. Figure 1.3 shows a microscope image of representative cells, and Table 1-2 lists some properties of this remarkable organism. All work in this thesis was carried out with *Dictyostelium discoideum* cells.

In this thesis, we focus on group migration during the aggregation of *Dictyostelium*. During this process, cells sense, migrate towards, and secrete the small molecule cAMP as a method of communicating the location of the aggregation center. In order to understand how aggregation works, we first investigate how an individual cell is able to sense a cAMP signal, and then we move on to cell motion and collective behavior.

Table 1-2 – Properties of Individual *Dictyostelium discoideum* Cells

Genome Size [43]	34 Mbp
Predicted Protein-Encoding Genes [43]	12,500
Division Time [44]	10 hr
Elongated Length [45]	20 μm
Gradient Sensitivity [34]	10^{-3} – 10 nM/μm
Speed [45]	10 μm / min

1.3. *Model of Gradient Sensing*

1.3.1. Decoupling Gradient Sensing from Chemotaxis

To understand the rules governing collective motion in *Dictyostelium*, we first

seek to understand how cells take an external communication signal and transduce it

into an appropriate internal response. This process is termed 'gradient sensing' and

has been actively studied for over a decade.

A critical tool used in studying gradient-sensing molecules is Green Fluorescent

Protein (GFP) technology (and its variants), which revolutionized the use of optical

microscopy in biology [46] (and led to a Nobel Prize [47]). Many intracellular

proteins of interest can be linked to GFP, allowing for time-resolved visualization of

the spatial concentration of protein in cells [48]. Scientists were able to apply this

technology to the gradient-sensing components of *Dictyostelium*, allowing them to

visualize the fusion proteins involved in gradient sensing in cells that had been treated

with a drug inhibiting their motion [49]. These studies showed that the ability of cells

to sense an external signal was still active even though the ability to move was

eliminated, effectively showing that to some extent gradient sensing could be

decoupled from motion [50]. With this knowledge, a number of experiments investigated the ability of cells to sense gradients in various conditions: time-varying gradients [51], strong and weak sources [52], etc. In addition, this knowledge allowed the generation of simplified computational models of the dynamics of the molecules involved, as it was no longer necessary to account for cell motion [53]. These models in turn led to the design of experiments to test these models. We now take a closer look at the molecular signaling pathways that allow a cell to transduce an external chemical gradient into a strong internal signal.

1.3.2. The Biochemistry of Gradient Sensing in *Dictyostelium*

Many molecules involved in gradient sensing have been discovered over the past two decades. Below we highlight current knowledge about the most-studied gradient-sensing pathway in *Dictyostelium*, that of phosphoinositide 3-kinase (PI3K) (shown in Figure 1.4). The model studied in this thesis focuses solely on this pathway.

Dictyostelium cells are able to sense the concentration of cAMP in their surroundings by the binding of cAMP to receptors on the external face of their membranes. These receptors, called G-protein coupled receptors (GPCRs), span the membrane seven times and are bound on the intracellular side to heterotrimeric G-proteins containing α, β, and γ subunits. Upon cAMP binding, the GPCRs change their conformation [54], resulting in the dissociation of the coupled G-proteins into Gα and Gβγ subunits. These subunits in turn activate a wide array of other signaling molecules.

Chemoattractant stimulation of GPCRs leads to the rapid activation of Ras, which, in turn, activates PI3K. Once activated, PI3K converts membrane-bound phosphatidylinositol-4,5-biphosphate (PIP_2) into phosphatidylinositol-3,4,5-triphosphate (PIP_3) [15]. PIP_3 acts as a membrane docking site for molecules containing pleckstrin homology (PH) domains, such as Akt/Protein Kinase B (PKB), as well as nucleotide exchange factors for Rac and other small GTP binding proteins. These molecules in turn recruit actin polymerization and stabilization proteins to the fronts of cells [13].

At the back and side of gradient-sensing cells, the phosphoinositide 3' phosphate phosphatase (PTEN), which de-phosphorylates PIP_3 into PIP_2, is recruited [55]. This recruitment effectively eliminates the binding and activation of PH domain-containing proteins at the back and sides of cells, further ensuring that PIP_3 is localized exclusively at the cell front. The phosphorylation state of PIP_2/PIP_3 can therefore be viewed as an effective means to determine the gradient-sensing state of a cell [56, 57], and the local concentrations of these intracellular molecules will be a main readout for the model explained in Chapter 2. Proteins with PH domains will localize to the cell membrane when PIP_3 is present, and when these proteins are coupled to GFP they provide a readout of PIP_3 levels (and hence PI3K/PTEN activity).

While the PI3K pathway has been viewed for many years as the key gradient sensing pathway, recent work in *Dictyostelium* has indicated that other pathways may be acting in parallel [58, 59]. These pathways include phospholipase A2 (PLA2) [60], guanylyl cyclase (GC) [61], and target of rapamycin complex 2 (TORC2) [62].
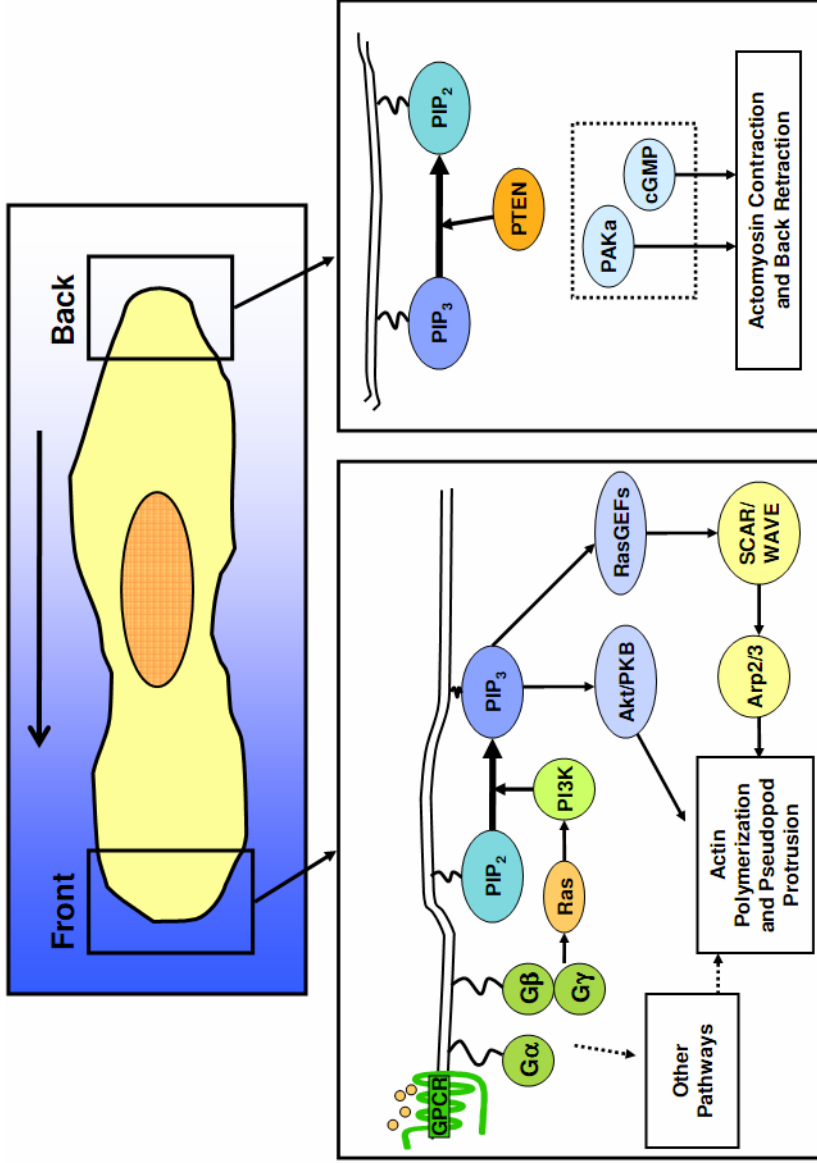
Figure 1.4 - Diagram of the Gradient-Sensing Machinery of *Dictyostelium discoideum*

The chemotaxis signaling pathway. (Top) Scheme showing a polarized cell in a chemoattractant gradient. The front of the cell is oriented toward the higher concentration of chemoattractant. The black arrow indicates the direction of motion. (Bottom, Left) At the front of the cell, GPCR activation initiates an intracellular signaling cascade directing actin polymerization and pseudopod protrusion. The PI3K pathway, in which PIP_2 is converted into PIP_3, is shown in detail; other pathways are explained in the text and are not shown. (Bottom, Right) At the back of the cell PIP_3 signaling molecules are converted back into PIP_2. In addition, further molecules are recruited to cause actomyosin contraction leading to retraction of the cell back. Note that the pathways at the cell back are only now becoming understood, and therefore few links are drawn between the components

Interestingly, these pathways may not have identical roles. For example, the PI3K pathway has been proposed to confer specific sensitivity to shallow extracellular gradients as PI3K inhibited cells can still perform chemotaxis toward steep gradients [63]. Finally, it remains to be seen if lessons learned from the PI3K pathway are generally applicable to other parallel pathways.

1.3.3.   Classes of Gradient-Sensing Models

Although many of the key players regulating chemotaxis have been identified, a thorough understanding of the system requires knowledge of the timescales, binding rates, binding locations, and regulation of each of the molecules. To clarify this process, mathematical modeling has been used to determine if experimentally observed cell behavior can be understood entirely using known molecules and their spatiotemporal dynamics [64]. This approach has many advantages, including suggesting quantitative experiments, classes of new molecules to look for, and measurements that should be made.

Current mathematical models of gradient sensing generally follow the PI3K pathway and model the cell as a 2D circular object [65], although shape itself can play a role in sensing ability [66] (e.g. in a gradient, elongated cells will have a larger concentration difference between front and back than a rounded cell). There are several characteristic responses of cells to chemical signals that models must account for, as shown in Figure 1.5. When exposed to a uniform dose of chemoattractant, PI3K is activated at the entire cell membrane within seconds, but it then returns to basal levels in tens of seconds. This process is termed 'adaptation'. In a gradient,

PI3K is activated strongly at the up-gradient end of the cell, for gradient strengths differing by many orders of magnitude. This process is termed 'amplification'. As adaptation and amplification have been observed in cells lacking an actin cytoskeleton, gradient-sensing models must, at a minimum, explain these two processes without resorting to actin-based processes.

A variety of proposed mechanisms of gradient sensing have been mathematically modeled, and some of these models are illustrated in Figure 1.6. One of the earliest proposed models is the "Pilot Pseudopod" model, in which a cell continuously extends small pseudopods in many directions, only keeping and enlarging those that experience an overall positive temporal change in chemoattractant-bound receptor [67]. While this model can account for motion in response to a gradient, it does not explain the observed enrichment of PH domain-containing proteins at the front of cells treated with agents that inhibit pseudopod formation.

Another gradient-sensing model is the Local Excitation, Global Inhibition (LEGI) model [68]. In this model there are three chemical species: one is a stationary membrane-bound excitation molecule that is quickly activated by the binding of chemoattractants to GPCRs; another is a diffusible slowly-activating global inhibitor whose concentration is set by the average cell exposure to chemoattractants; the final molecule is the read-out of the sensing system.
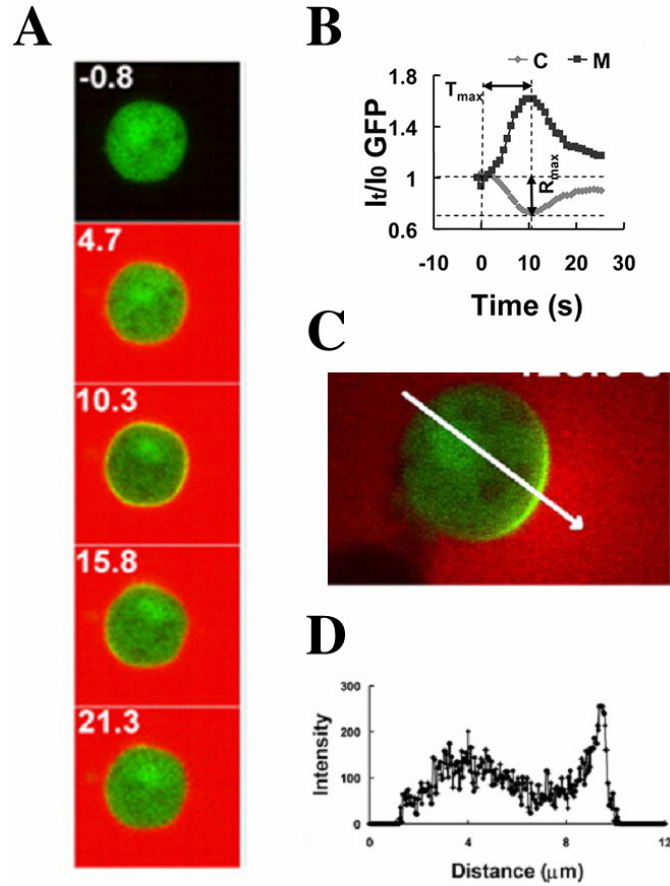
Figure 1.5 – Characteristic Responses of Cells to Chemoattractants
Dictyostelium cells treated with Latrunculin A cannot polymerize actin and so
remain round, but they are still able to respond to the chemoattractant cAMP.
Membranes of cells expressing the PH_{CRAC}-GFP protein glow green to indicate
their response to the chemoattractant. Chemoattractant is shown in red. (A)
Time-lapse images show that about 10 seconds after stimulation with a uniform
cAMP dose, the cells uniformly respond on their membrane. The response dies
down after 20 seconds. This process is called 'adaptation'. Numbers are time in
seconds. (B) Quantification of the cell response. "C" = cell center, "M" = cell
membrane. The response to the uniform dose, where labeled protein leaves the
cytosol and moves to the membrane, peaks around 10 seconds. (C) Steady-state
response of cell to a stable cAMP gradient. The gradient is strongest at the
bottom-right and declines moving to the top-left. Note the strong crescent shape
of the membrane response on the bottom right of the cell, which is steeper than
the gradient itself. This process is termed 'amplification'. The arrow indicates
the line of pixels used for quantification in (D). (D) Pixel intensity values,
showing a marked increase toward the gradient source. The bump in the middle
is most likely due to autofluorescence of the nucleus (noticeable also in (A)).
*Figure reproduced from Figs 1A, 1E, 7A of [51], copyright 2005 American
Society for Cell Biology. Used with permission.*
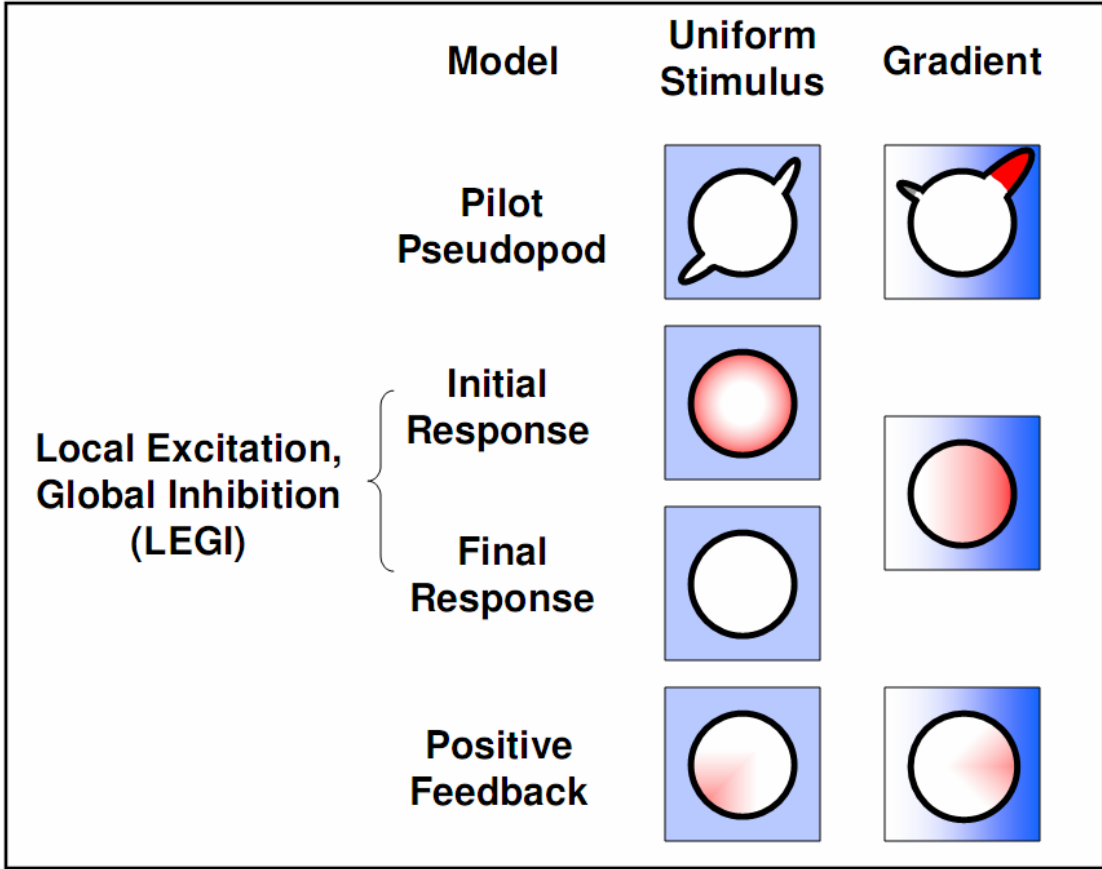
Figure 1.6 - Schematic Representation of Mathematical Models for Gradient Sensing.

Cells (round) are exposed to either a uniform stimulus (left column) or a gradient (right column). The resulting spatial intracellular stimulation level of the cell is shown in red. In the Pilot Pseudopod model, cells detect a gradient by extending small pseudopods that sense a temporal change in chemoattractant receptor occupancy. In the Local Excitation, Global Inhibition (LEGI) model, the response of the cell to a uniform stimulus is initially along the periphery but diminishes with time. In a gradient, the response matches the strength of the external gradient. In the positive feedback model, the cell has a region of strong excitation. When uniformly stimulated, this region is randomly located, whereas in a gradient it follows the direction of, but is much stronger than, the external gradient.

Mathematically, we have

$$\frac{\partial E}{\partial t} = -k_{-e}E + k_e S + D_M \nabla_M^2 E \qquad (1.1)$$

$$\frac{\partial R}{\partial t} = -k_{-r}IR + k_r E + D_M \nabla_M^2 R \tag{1.2}$$

$$\frac{\partial I}{\partial t} = -k_{-i}I + k_i S + D_c \nabla^2 I \tag{1.3}$$

where E, R, I are the excitation, read-out, and inhibition molecules, respectively. S is the chemical signal. The rate constants k are decay and production constants for their respective molecules. D_M is the membrane diffusion constant for E and R, which *are* membrane-bound. D_c is the cytosolic diffusion constant of I, and is generally at least 2 orders of magnitude greater than D_m [69]. A uniform stimulus of chemoattractant causes a rapid activation of the excitation molecule all around the cell periphery, quickly causing an increase in the read-out response. However, this response is dampened by the slow activation of the inhibitor molecule, which eventually lowers the read-out molecule concentration back to baseline (see Figure 1.7). A steady gradient of chemoattractant, however, causes the excitation molecule to be more active at the front, while the inhibitor is present equally everywhere. This situation leads to net read-out increase at the front of the cell. While Ras or PI3K can play the role of the local exciter, a candidate molecule for the global inhibitor has yet to be identified. While this model therefore explains adaptation and gradient-sensing, it is not able to address amplification, as the internal molecule gradients do not reach levels observed in experiments.
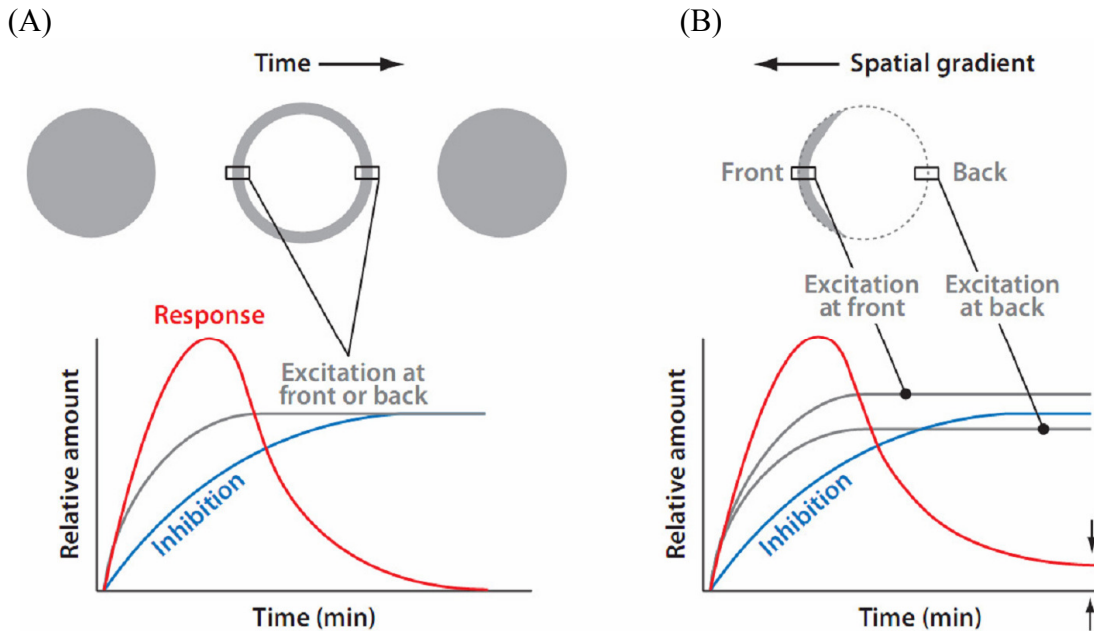
Figure 1.7 – Illustration of Local Excitation, Global Inhibition (LEGI) Model of Gradient Sensing
(A) When exposed to a uniform dose of chemoattractant, the cell initially produces the excitation molecule everywhere (gray line). The inhibitor molecule concentration, which is dependent on the average chemoattractant concentration and acts globally, grows more slowly (blue line). Eventually, the activities of the two molecules equalize, canceling each other out. The overall response (red) essentially equals the excitation minus the inhibition, and therefore initially the cell responds everywhere, but the response eventually subsides. (B) When exposed to a chemical gradient, the dynamics are similar to exposure to a uniform signal, with one major difference: the local excitation molecule is produced more at the up-gradient side than at the down-gradient side. Since the inhibitor molecule is based on the average chemoattractant concentration and acts everywhere, it eventually cancels out the excitation at the back but not the front. When steady-state is reached, the cell remains responsive at the front, as shown by the arrows. *Figure reproduced from [24] with permission.*

Another model is that of activation driven by positive feedback loops, so that a small external gradient is amplified into a large internal response [70]. This model, however, is very sensitive to spontaneous activation, and it displays a switch-like response that is not observed in cells. Therefore, while addressing amplification, this model does not properly address adaptation.

Some recent models, such as 'balanced inactivation' [71] or LEGI coupled to a

feedback loop [72], have been proposed to address shortcomings in previous

mathematical models. Similarly, in Chapter 2 we describe a mathematical model that

combines both LEGI-type mechanisms as well as positive feedback loops. In

addition, our model contains tunable parameters allowing it to emphasize or de-

emphasize either of these mechanisms, leading to qualitatively different behavior for

different parameter choices [69, 73].

1.3.4.   Model with an Intermediate Level of Detail

Chapter 2 explains a gradient-sensing model developed fully in previous work

[35] that contains two positive feedback loops and one negative feedback loop. The

term 'intermediate' level of detail is used to designate that the model explicitly treats

the time dynamics of six intracellular signaling molecules. However, this model is

not as simple as those presented previously, which generally explicitly model two or

three molecules. The model also does not track the dynamics of all possible players

in the system. Instead, it balances modeling the dynamics of six molecular species

with the ability to adjust parameters to change the output enough to explain observed

experimental behaviors.

Previous models of cell behavior generally make predictions about a cell's

response to a gradient, but are themselves are not well-characterized in terms of

responses to perturbations or sensitivity to additional signals. In Chapter 2 we

address these concerns through a linear stability analysis to determine the robustness

to noise that may arise from a number of biological or physical sources, such as

stochasticity in receptor activity. In addition, simulations are performed to test the

response of the model to temporally and spatially localized sources of

chemoattractant. Both analytically and in numeric simulations, the model is most

responsive to signals located off-axis to its initial polarization, which is suggestive of

the zigzag type motion that real chemotaxing cells display. We envision that similar

treatments of other gradient-sensing models should help to elucidate the

characteristics of those models, aiding in determining their validity.

1.4. *Dynamics of Individual Cell Motion*

Together with the rules underlying how a cell senses a chemical signal,

understanding collective motion depends upon also knowing how a cell generates

motion due to a sensed signal. Tying together gradient-sensing with cell motility is

not a trivial problem; in the following subsection we briefly explain what is known

about motility in *Dictyostelium* and how gradient sensing fits into the overall picture.

1.4.1. Biochemistry of Cell Motion in *Dictyostelium discoideum*

The gradient-sensing signaling pathway leads to actin polymerization at the up-

gradient side of the cell and myosin contraction at the down-gradient side, as shown

in Figure 1.4. This process is involved in localizing actin network cross-linking in a

proper spatio-temporal fashion to drive the membrane forward. Biochemical

experiments have revealed many of the proteins involved in this process in

Dictyostelium, although many of these proteins also exist in other motile cell systems. Now we briefly touch on the biochemistry of cell motion.

The output molecules of gradient sensing recruit WASP (Wikott-Aldrich syndrome protein) and members of the SCAR (suppressor of cAMP receptor) complex, such as SCAR, Nap1, PIR121, Abl2, and HSPC300, to the cell front. These molecules, in turn, bind Rac proteins, which then lead to pseudopod extension via F-actin assembly. In addition to binding Rac, these molecules cause the Arp2/3 (actin related proteins 2 and 3) complex to bind locally to actin polymers. This complex causes new actin polymers to branch off of existing polymers at a 70 degree angle with respect to the previous polymer. The repeated action of these complexes causes the up-gradient side of the cell to contain a meshwork of actin polymers able to support pseudopod protrusion. At the cell back, PAKa and the nucleotide cyclic GMP cause myosin II assembly and phosphorylation. This process eventually leads to acto-myosin based cell contraction [13].

It should be noted, however, that the molecules acting as a result of the gradient-sensing pathways can themselves feed back into the activity of the gradient-sensing pathways. For example, polymerized actin at a cell front can locally reinforce the action of PI3K, even when a gradient disappears [56]. Evidence for these signaling networks often arises from examining phenotypes and protein expression levels in genetic knockouts or knockdowns, and therefore usually does not lead to insights regarding the temporal aspect of motility regulation. Additionally, cells can display the ability to move without an external gradient [74]. In order to understand motion, models of cell motion are required that integrate the biochemistry

with these known phenotypes, in order to elucidate how motility emerges from these signals and to make quantitative predictions.

1.4.2. Models of Cell Motion

There are several putative ways in which gradient sensing can feed into directed cell motion. One of the simplest ways is the local accumulation of PIP_3, which drives local recruitment of actin, and therefore motion in that direction. This model cannot account for the motion of cells exposed to a uniform chemoattractant gradient unless positive feedback leads to polarization due to noise. Even then, local PIP_3 levels still drive actin polymerization. There is recent evidence that such positive feedback loops may exist, which could support this type of excitation and motion model [75].

An alternative model that has recently been gaining recognition is that of a biased excitable actin network [76, 77]. In this model, the actin in a cell is an excitable system that can be driven quickly to polymerization by a signal, which is self-driving until a large fraction of the cell's actin is polymerized. In this case, there must also be a depolymerization step, either self-driven or regulated by another molecule, in order to reset the system. PIP_3 levels in this model would be used as the initiating signal and its levels would then be relatively irrelevant (as long as the initiation threshold was crossed). If the polymerization signal takes a finite time to travel through the cell, subsequent polymerization events would be biased toward starting at locations of previous initiation events (as depolymerization would occur at the initiation sites first). Thus, a cell receiving a signal to polymerize from all directions would pick a direction randomly at first, but the excitable actin network

24

would then self-enforce persistence in that direction even though the gradient-sensing ability of the cell is quiescent. This is termed the 'Pseudopod Centric' model of cell motility [77].

Compelling evidence for this type of model is emerging. Spreading *Dictyostelium* cells display actin 'waves' in which polymerization of actin begins at a particular point of cell-surface contact and propagates throughout the cell on the timescale of 5 minutes [76, 78]. In addition, experiments have shown that two stable pools of actin exist in cells: non-polymerized and polymerized. Both types of actin are stable, and some of the gradient-sensing molecules are able to drive the transition from one stable type to another [79]. Finally, quantification of time-lapse images of cell motion [74] indicate that cells display 'curvature waves,' which could be actin waves pushing against the cell membrane.

1.4.3. Quantification of Cell Motion

The vast majority of previous studies on cell motility restricted their analysis to center-of-mass motion, mostly due to the difficulty in quantifying large numbers of cell boundaries from image data sets. Only recently has work been undertaken that attempts to dissect sub-cell scale behavior (e.g., localized protrusions) using parameterized cell boundaries [80].

A semi-automated cell boundary tracking method developed in the Losert Lab is described in [74]. By applying this method to datasets of cells moving in a uniform chemoattractant field, Driscoll and others find that cells form successive protrusions at their fronts in a zigzag type manner. Cells cause motion through the simultaneous

translation of these protrusions along the side of the cell and coupling them to the substrate. Finally, cells not in contact with the substrate still display these protrusions and subsequent translation, suggesting that the biasing of naturally occurring protrusive activity is the main function of gradient sensing. This work expands our understanding of the mechanisms regulating cell motion, which is consistent with the results of Chapter 3, described below.

1.5. *Collective Motion of Cell Systems*

1.5.1. Collective Motion during *Dictyostelium* Aggregation

Having investigated some of the physical rules followed by cells in sensing and responding to chemical signals, we turn our attention to understanding how these cells act in a complicated, collective environment. We now explain aggregation in *Dictyostelium discoideum* to understand in more detail how the collective regulation of behavior can lead to remarkable results.

In the wild, *Dictyostelium discoideum* cells chemotax toward bacteria by sensing byproducts of bacterial metabolism, such as folic acid, and then engulf the bacteria upon contact. After enough material has been metabolized, the cell is able to divide into two identical cells and then continue the feeding process. During this process, the quorum-sensing molecule Pre-Starvation Factor (PSF) is secreted, and cells sense its concentration in order to 'estimate' the cell density in the environment. Eventually, however, the food supply runs out, and the cells are unable to find enough nutrients in their environment. In this case, *Dictyostelium* cells enter a developmental
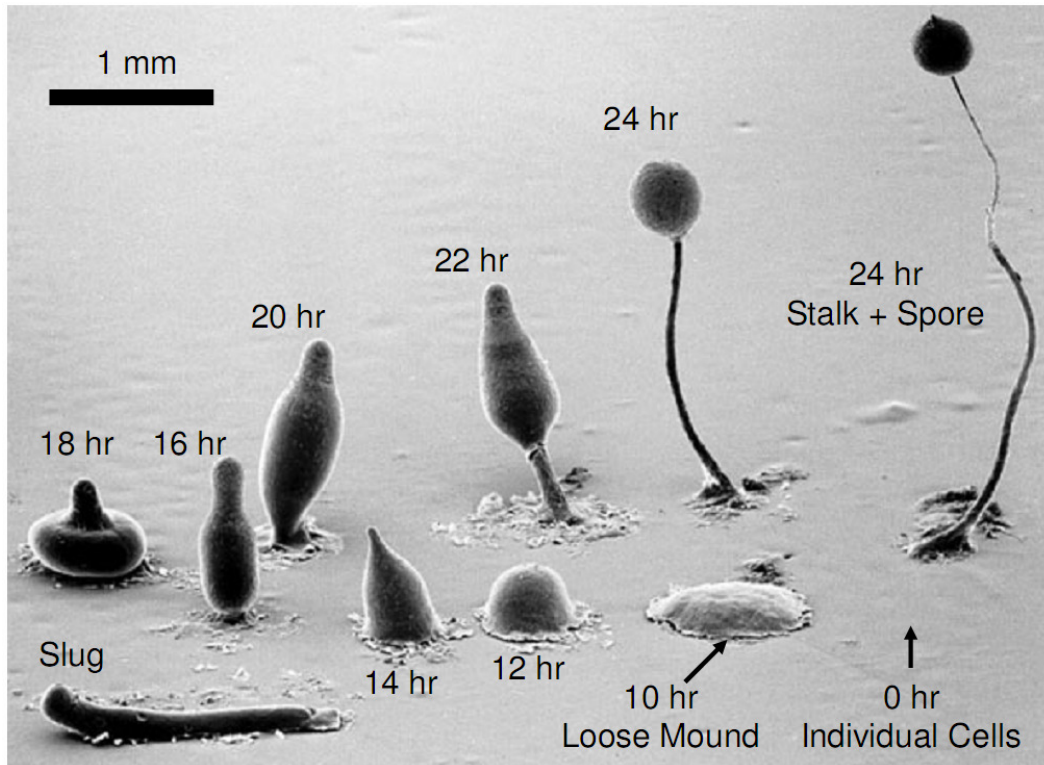
Figure 1.8 – Life Cycle of *Dictyostelium discoideum*
Scanning electron micrograph of the different stages of *Dictyostelium discoideum*
from the initiation of starvation to 24 hours later.
Adapted from image by M.J. Grimson & R.L. Blanton, Biological Sciences
Electron Microscopy Laboratory, Texas Tech University at www.dictybase.org.

program that will eventually result in the formation of a fruiting body composed of a

stalk and spore [81], as shown in Figure 1.8.

Starving cells estimate the number of nearby starving cells through secretion

and sensing of Conditioned Media Factor (CMF), a quorum-sensing molecule that, at

high enough concentrations, indicates that there are enough starving cells to begin the

aggregation process [82]. Individual *Dictyostelium* cells change their protein

expression levels and enter a genetic program specific to the aggregation phase. As

part of this process they eliminate the bacteria-sensing receptors from their surface

and create the cAMP surface receptor cAR1 (cyclic-AMP receptor 1), as well as the

membrane-bound protein adenylyl cyclase A (ACA), which gives them the ability to create large amounts of cAMP. After 4-5 hours of starvation, the cells are ready to aggregate. To initiate the process, a few cells spontaneously emit a small amount of cAMP [83], which nearby cells sense. These cells then, over the course of 2-3 minutes, desensitize their cAMP receptor, move toward the source of the signal, and release their own cAMP in a process called 'signal relay'. Afterwards the cell receptors are resensitized, and they are ready to perform the process once again [84].

This remarkable system results in waves of cAMP that can be transmitted over millimeter distances, resulting in striking patterns of migration [85]. After aggregation is complete, the cells continue to change their set of expressed proteins, and undergo morphogenesis into a series of characteristic structures. The end result is a spore containing ~80% of cells atop a vacuolated stalk of the remaining ~20% of cells, which essentially sacrifice themselves to lift the spore up to a height of over 3 mm. There are between 10,000 and 100,000 cells in the final structure, and this number is regulated throughout the morphogenesis process via secreted quorum-sensing factors [86, 87].

The portion of the life-cycle that is addressed in this thesis is the single-to-collective transition (from 0 – 10 hours in Figure 1.8). It is during this process that cells communicate and move as individuals, and so the motion of all cells can be tracked.
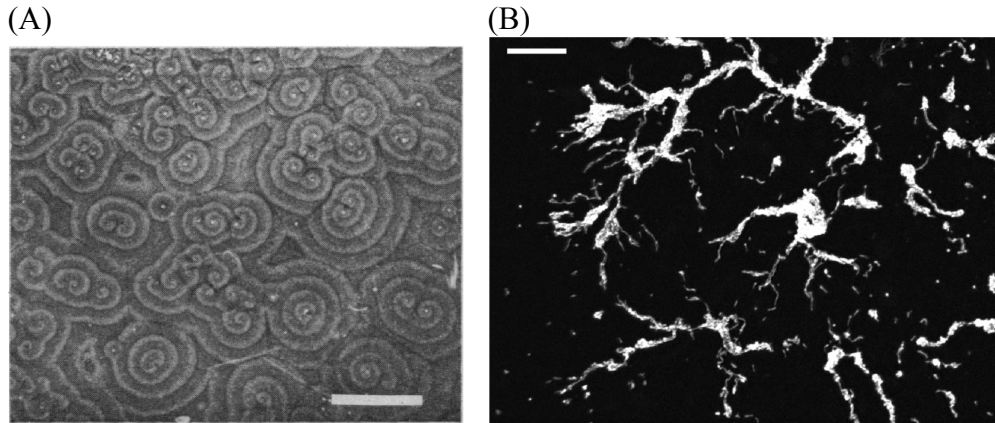
Figure 1.9 – Aggregation patterns in *Dictyostelium discoideum*
(A) *Image reproduced from [85] with permission*. Early aggregation signals in *Dictyostelium discoideum* produce traveling waves of cAMP, here seen through isotope-dilution fluorography. Scale bar = 1 cm. (B) Dark-field image of aggregating cells. cAMP waves lead to the formation of aggregation territories, as well as head-to-tail chains of migrating cells ('streams'). Scale bar = 200 μm. Note the vastly different scale on the two images.

1.5.2. Models of Collective Motion

The cell-to-spore life cycle of *Dictyostelium* has been a consistent source of experimental questions and computational models for two decades. The first quantitative experiments focused on the initial signaling pattern in a field of aggregation-competent *Dictyostelium* cells [85], in which large-scale traveling waves of cAMP move through the population, eventually leading to aggregation at signaling centers (see Figure 1.9 A).

During aggregation, cells move in response to the cAMP waves, causing the formation of patterns of head-to-tail chains of cells, called 'streams', that move toward the aggregation centers (see Figure 1.9 B). This process has provided the basis for a number of mathematical models. Initial models were continuum models of aggregation, in which the cell distribution was treated as a concentration field [88-

90]. Next came cellular automata (CA) and cellular Potts models, which are discrete but do not model cells as physical objects *per se* [91-93], and then discrete models in which the cells were individual entities with collision repulsion [94-98] (see Figure 1.10 for illustrations of the models). As an example of a mathematical model of aggregation, we present below a model formulated by Palsson [96] where cells are physical objects, subject to physical forces .

Every cell is subject to physical forces, and as cells exist in viscous fluid, acceleration is neglected. Cell i is subject to viscous drag forces from the substrate and other cells as follows:

$$\vec{F}_i^D = \mu_s \frac{A_{is}}{A} \vec{v}_i + \mu_c \sum_{j \in N(i)} \frac{A_{ij}}{A} (\vec{v}_i - \vec{v}_j) \tag{1.4}$$

$\vec{F}_i^D$ is the drag force, μ_s and μ_c are the coefficients of friction for cell-surface and cell-cell contacts, respectively. The μs are of order 10^{-7} N s / μm. A is the cell surface area, and A_{is} and A_{ij} are the areas of surface contact between cell i and the substrate, or cell i and cell j, respectively. $\vec{v}_i$ is the velocity of cell i, and the sum is over all neighbors of cell i.

As there is no acceleration, there must be a balance of forces on the cell. Therefore, the drag force on a cell is balanced by the active force generated by the cell, the forces generated by other cells acting on that cell, and the elastic forces acting on that cell (caused by collision with other cells). Separating out $\vec{F}_i^D$ we have

$$\mu_s A_{is} \frac{d\vec{x}_i}{dt} = \vec{F}_{i(j/s)}^{\text{act}} + \sum_{j \in N(i)} \vec{F}_{ij}^{\text{pass}} - \sum_{j \in N(i)} \vec{F}_{ij}^{\text{act}} - \mu_c \sum_{j \in N(i)} \frac{A_{ij}}{A} (\vec{v}_i - \vec{v}_j) \tag{1.5}$$

The sums are over all neighbors. $\overset{\vee}{F}_{ij}^{\mathrm{pass}}$ are the elastic forces between cells i and j,

which in this model are attractive for distances slightly greater than one cell diameter

and repulsive for distances smaller than one cell diameter. This force is on the order

of tens of nN. $\overset{\vee}{F}_{i(j/s)}^{\mathrm{act}}$ is the active force of cell i on either neighboring cells j or the

surface s. These active forces are on the order of 50 nN, pointed in the direction up

the cAMP gradient. A small random noise force, of order 10 nN, is added in a

random direction to the active force to add some stochasticity.

    The cAMP field is modeled as

$$\frac{\partial c}{\partial t} = D\nabla^2 c - \frac{\alpha c}{c + \beta} + \sum_i \delta(\overset{\vee}{x} - \overset{\vee}{x_i})\left(\gamma_i - \frac{\lambda c}{c + \kappa}\right), \qquad (1.6)$$

where c is the cAMP concentration and D is the diffusion constant of cAMP (D=400

$\mu\mathrm{m}^2$/sec). The second term on the right hand side is degradation due to extracellular

phosphodiesterase (which catalytically degrades cAMP). Phosphodiesterase is

assumed to be at constant concentration and acts with Michaelis-Menten reaction

kinetics with constants α and β. Finally, the last term on the right hand side

represents the actions of cells: there is a cell-specific secretion rate γ_i as well as cell-

bound phosphodiesterase degradation, again acting with an activity depending on

parameters λ and κ. The sum is over all cells i. The secretion rate γ_i itself follows

very complex dynamics; the equations are not reproduced here but can be found in

[102], as can values for the phosphodiesterase parameters. The direction of the

gradient of this cAMP field directs the active motion of the cells. Sample output of

the model is shown in Figure 1.10 C.

A

B

C
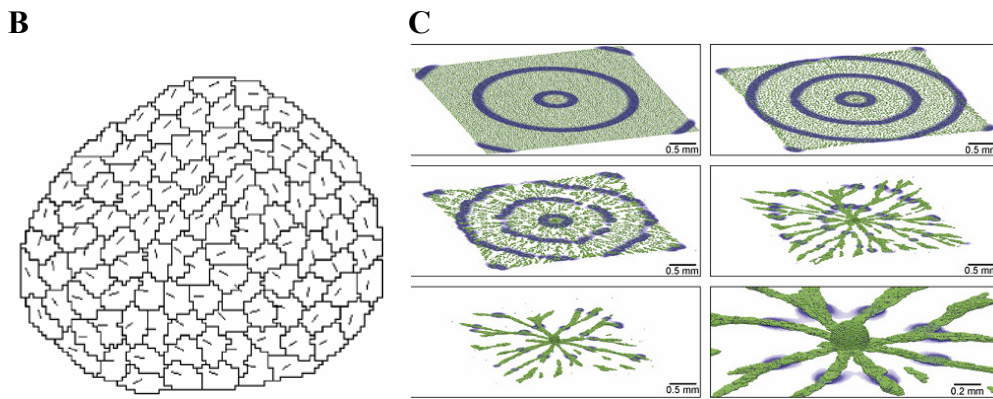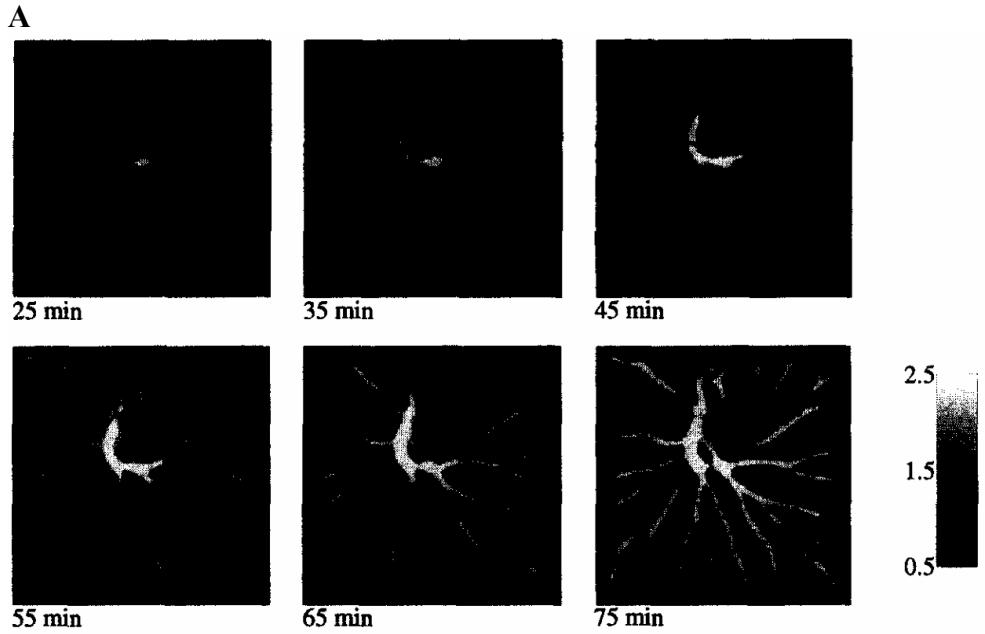
Figure 1.10- Examples of Models of *Dictyostelium* Aggregation

Several classes of models have successfully captured the qualitatively individual to group dynamics of *Dictyostelium* aggregation. (A) Aggregating cells are modeled by continuum treatment of cell density. Whiter pixels indicate greater cell density. *Image reproduced from [99] with permission.* (B) Aggregating cells are modeled by a Potts model. *Image reprinted from Fig. 2 from [100]. Copyright (1999) by the American Physical Society. Used with permission.* (C) Cells are modeled as deformable 3-D objects. *Image reproduced from [101] with permission.*

While this model captures the aggregation dynamics with more fidelity than earlier models, those models were still able to capture the most striking qualitative feature of aggregating cells: the streams. The consensus is that streams form due to an inherent streaming instability that arises due to cell-cell attraction from signal relay [103]. Although a qualitative understanding of aggregation has been provided by the previously mentioned models, models attempting to predict the transition from single cell to slug are still being researched and have had some success [102]. In addition, recent experimental work has revealed that cells within streams may have additional coupling through F-actin polymerization waves and cAMP signaling unaccounted for in models [104]. Finally, it has been shown that the signal relay release may be localized [105, 106], a fact that no model has taken into account. We hypothesize that careful selection of the metrics used to characterize the aggregation process may further the basic understanding of how a chemotactic signal couples to motion. These measurements may show that additional considerations may be required when attempting to model collective *Dictyostelium* motion.

1.5.3. Studies of Individual Behavior

To our knowledge, no experimental work has been undertaken that performs in-depth analysis of individual *Dictyostelium* motion during the transition from individual cell to collective aggregate [107]. Research continues on individual cell motion in well-defined gradients (such as those from microfluidics) [34, 108-110], and the characterization of cell sensitivity, as well as cell shape and the forces generated during motion. These studies generally present cells with a well-defined

signal that is constant in time, or no signal at all. In nature, however, the cAMP field is fluctuating in time [111], and the spatial dependence is heavily influenced by the secretion of the cells themselves. Therefore, a study of individual cell motion during aggregation would be able to address several questions: How does cell motion depend on the stability of the surrounding field? What is the effect of signal relay, and what advantages does it bring to a cell population? Other species of *Dictyostelium*, such as *Dictyostelium minutum*, thrive in nature by aggregating with no relay [112]. How do cells move inside of streams (computational models make predictions, but systematic studies have not been carried out), and does motion in streams enhance aggregation in some fashion? Another question of interest is, what is a good metric for differentiating when relay is present or not? Indeed, streams present an obvious marker in *Dictyostelium*, but other amoeboid cells may similarly enhance motion through signal relay and yet not display streams.

In Chapter 4 experimental work is presented that addresses these questions. We find that the chemotactic index (CI), a measure of direction, provides a good metric to determine the presence of signal relay. We also show that cell speed and persistence of motion are unaffected by signal relay, suggesting that cells use gradient sensing to steer their inherent ability to protrude pseudopods. Finally, we quantitatively establish that signal relay dramatically broadens the range of an aggregation signal, with the added effect of making the directional component of a signal weaker in areas that would be reached in the absence of relay.

1.6. *Cell-Surface Adhesion and Migration*

1.6.1. Cell Motion Cycle Depends on Adhesion

The collective motion of cells depends on a variety of environmental conditions. For example, if there is a large fluid flow during *Dictyostelium* aggregation, the chemical signal is not properly relayed and aggregation does not occur. Additionally, increasing the temperature initially causes cells to stop responding to cAMP signals, and then die. However, changing conditions in a controlled fashion and assessing the effects can lead to a greater understanding of the system. One such condition that can be changed is the cell-to-surface adhesion, and we explore the implications of such a change below.

The question of the effects of environmental change is salient to understanding cell behavior, particularly as it has been shown that many mechanical properties, such as topography and stiffness, can have drastic effects on cell behavior. For instance, stem cells, which can differentiate into any type of cell in the body, will differentiate in a fashion that is dependent on the substrate elasticity: they become neurons on soft substrates, arterial walls on moderately stiff substrates, and bone cells on stiff substrates [113]. As another example, neutrophils have a biphasic dependence of migration speed with substrate stiffness [114]. Adhesiveness is another parameter that can be adjusted on surfaces, and has been shown to have implications in many health-related fields, such as diagnostics (so that cells do not stick to the walls of testing devices) and implant effectiveness (cells must be able to properly adhere to implants to begin a proper healing process). In addition, adhesiveness has been shown to affect neuron outgrowth [115]. Therefore, a more general understanding of

cell-surface adhesion and the resultant behaviors can be found through a study of individual and collective amoeboid migration.

The ability of cells to move on top of a two-dimensional surface is of fundamental importance to cell migration. Previous studies have established that the characteristic cycle of amoeboid cells (such as *Dictyostelium*) moving on a surface moves the cell ~15 μm in ~1-2 min [116], and is as follows (see Figure 1.11): 1) The cell extends a pseudopod via the polymerization of actin and places this pseudopod on the substrate. 2) The pseudopod is anchored to the substrate through the formation of linkages between transmembrane adhesion receptors and the surface. 3) The cell removes adhesions from the cell rear by some mechanism, such as endocytosis of the receptors. 4) The cell contracts its actin cortex through the action of actomyosin, causing a net forward motion of the cell body (as the front is anchored to the surface but the rear is not). In this view of cell motion, it is clear that cell-substrate adhesion plays a critical role in two steps. Cell-substrate adhesions that are too strong will allow the cell to properly extend pseudopods and to anchor to the surface, but will not allow de-adhesion, causing the cell to remain firmly stuck in place. Adhesions that are too weak will not allow proper anchors to form, so that the overall contractions break anchors, causing the cell to be stalled in place, unable to generate the traction required to move. It is hypothesized that a surface adhesiveness somewhere between these two extremes allows cells to move with maximal efficiency [65, 66], a view that has been borne out through experiments on several cell types [117]. This biphasic dependence of cell speed on cell-surface adhesion is illustrated in Figure 1.12 A.
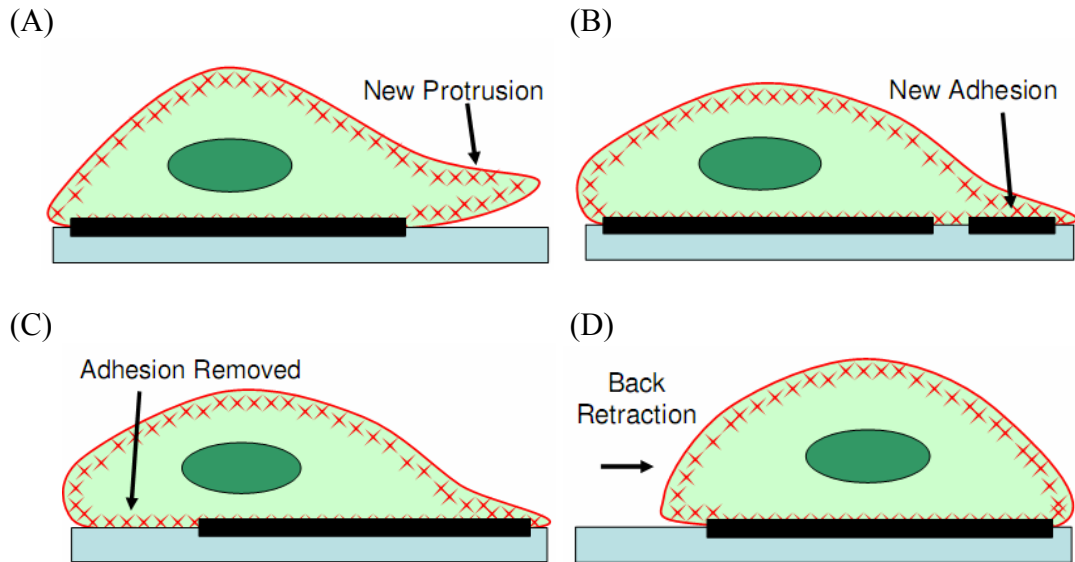
Figure 1.11 – Characteristic Motion Cycle of Amoeboid Cells
Cartoon of a cell undergoing one cycle of motion, moving to the right. The actin cortex is red, the nucleus is dark green, and the cell-substrate adhesions are black. (A) The cell pushes the front of its membrane forward using actin-based protrusion. (B) The new protrusion forms adhesions with the surface. (C) The cell de-adheres its back from the surface. (D) The cell contracts the actin cortex, moving its body forward as the back is no longer adhered.

Recent work, however, has shown that for some cells, specifically those that do not form strong cell-surface contacts and that display amoeboid motion (such as *Dictyostelium*), this hypothesis of adhesion-dependent motion may not hold true (see Figure 1.12 B). Studies have shown that dendritic cells (a type of mammalian immune cell) are able to compensate for low or high cell-surface adhesion through modulating their actin polymerization, and therefore are able to move at a constant speed [118]. Previous work indicated that *Dictyostelium* can move on surfaces of varying adhesiveness, although how exactly this feat is accomplished is not known [119]. In addition, how adhesion affects collective *Dictyostelium* motion is an open question.

1.6.2. Molecular Mechanisms of Cell-Surface Adhesion

Once again, to understand the effects of adhesion on collective motion, we must understand how the rules of individual cell behavior change due to changes in adhesion. To this end, we review cell-to-surface adhesion mechanisms and molecules. A list of adhesion molecules is given in Table 1-3.

Many migratory mammalian cells, such as fibroblasts and epithelial cells, have transmembrane adhesion receptors termed integrins, that bind to specific extracellular surfaces, such as the extracellular matrix (ECM). The bond can have adhesive strength of order 100 N/m^2 [120] and often triggers a particular response in a cell, causing it to follow a set pattern of behavior depending on the cell type and the surface that has been bound. The majority of adhesion studies focus on integrin-based adhesion and its associated molecular complexes.

In contrast, *Dictyostelium* does not use integrins to bind to surfaces [121]. The methods used by *Dictyostelium* to bind to substrates have not been entirely characterized, although some regulators of cell-surface adhesion are known. Only one adhesion receptor (sadA) has been identified. This receptor is active solely during the vegetative (non-starving) part of the life cycle [122]. Cells lacking this receptor do not bind well to plastic and have difficulty phagocytosing latex beads. The binding of *Dictyostelium* is termed 'non-specific', meaning that these cells are able to adhere to a variety of surfaces. However, there is evidence that this 'non-specific' binding is accomplished through several different receptors, as a genetic mutant was developed that retained the ability to bind to hydrophilic surfaces

38
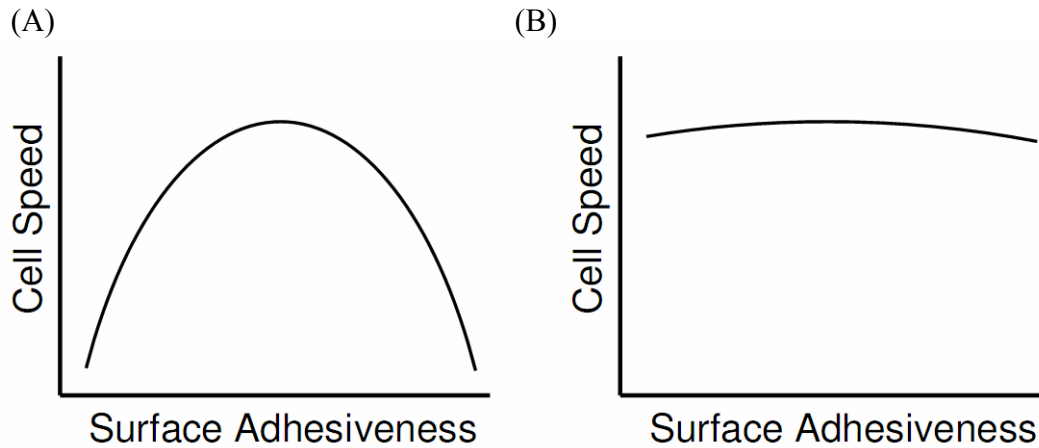
Figure 1.12 – Cell speed dependence on surface adhesiveness
(A) In the standard view, cell speed has a biphasic dependence on cell-surface adhesiveness: surfaces that are non-adhesive do not allow cells to gain the traction necessary to move, while surfaces that are too adhesive do not allow cells to remove themselves from the surface. *Adapted from [117].* (B) Recent work in amoeboid cells has shown that the view in (A) may not always hold true: for a large range of adhesiveness, cells are able to move with similar speed. For other cell types (A) may still be the correct picture.

but not hydrophobic ones [123]. These 'non-specific' receptors are able to form cell-surface adhesions with strength greater than 10 N/m^2 [124]. Even among hydrophilic surfaces, *Dictyostelium* spreads differently on surfaces with different electrostatic charge [125], with cells generally spreading more on surfaces with a greater positive charge. In addition, the mechanisms of adhesion depend on the stage of the life cycle, as was found for a secreted protein that inhibited cell-substrate adhesion in feeding cells but not starved cells [126]. Finally, sites of close cell-surface contact correlate with the location of clustered actin, leading to the idea that the cells form 'actin foci' at the receptors in order to adhere properly [127]. Still, the vast majority of surface adhesion receptors have yet to be found in *Dictyostelium*, leaving the mechanisms regulating adhesion unknown.

Table 1-3 – Known *Dictyostelium discoideum* Adhesion Molecules

Name	When Expressed
Cell-Substrate	
sadA	Vegetative (non-starving)
sibA	Entire life cycle
Cell-Cell	
Dd-CAD1	Early Starvation to Slug
gp80	Starvation to Fruiting Body (Spore/Stalk)
gp150	Late Starvation to Fruiting Body
psA	Loose Aggregate to Slug

This table is adapted from a recent review [128].

During collective motion, cells not only experience cell-surface contacts, but also cell-cell contacts. As opposed to cell-surface receptors, a variety of *Dictyostelium* cell-cell adhesion receptors have been identified and characterized [129]. Some of these adhesions are calcium-dependent, while others are not [130]. The proteins are differentially expressed through the life cycle [131] and can localize to specific parts of the cell, such as the pseudopod [132]. The regulation of these receptors is also dynamic and can be affected by the number of nearby cells, as measured by quorum-sensing factors [86]. Some receptors bind specifically to the same type of receptor on another cell, while others bind to a different type of receptor. In addition, the purpose of some of these receptors is not always obvious: in one case, the only phenotype for a mutant lacking the membrane glycoprotein csA was that it fails to properly form spores on soil, but is able to do so on glass, plastic, agar, and other common experimental surfaces [133].

1.6.3. Surface Adhesiveness and *Dictyostelium* Behavior

Previous work on the effect of cell-surface adhesion on the behavior of *Dictyostelium discoideum* focused on the phenotypes of cytoskeletal mutations on individual migration and found that certain components were important in particular circumstances. Wild-type cells proved capable of maintaining a consistent speed over a variety of surface adhesivities. Myosin-II null mutants, which have a decreased ability to generate contractile forces, move much more slowly over a very adhesive surface than on less adhesive ones [119], suggesting that wild-type cells require myosin II to generate enough force to overcome large adhesions [116] and tightly regulate their motility cycle [134, 135]. Cells in which talin, a regulator of adhesion in mammalian cells, was knocked out show decreased surface adhesion but no motility defects [136].   Cells in which several actin cross-linking proteins were knocked out have lower speeds on less adhesive surfaces but no problems on more adhesive ones [137, 138]. Other mutants have shown various phenotypes on a variety of surfaces [139, 140], but the picture of how the cells regulate their adhesion is a murky one. In addition, no studies have investigated the collective response of cells to surfaces of varying adhesivities.

Previous studies have generated models of how speed depends on cell-substrate adhesion. One essential component is how the cell-surface bonds behave under applied forces. Often the bonds are modeled as elastic springs that have some chemical off-rate. This type of model allows the bonds to transmit forces between the cell and surface, while maintaining the ability to detach if the forces get too large.

41

For instance, in one adhesion model [116], the off-rate dependence on displacement is modeled as

$$k_-(\overset{\text{v}}{x}) = k_-^0 \exp\left(\frac{k_s\Delta|\overset{\text{v}}{x} - \overset{\text{v}}{x_0}|}{k_B T}\right),\tag{1.7}$$

where $k_-(\overset{\text{v}}{x})$ is the off-rate for a cell-surface bond, k_-^0 is the off-rate without stretching, k_s is the spring constant of the bond, Δ is the characteristic potential well width keeping the bond from breaking (of order nm), k_B is Boltzmann's constant, and T is the absolute temperature. These bond dynamics inform the mechanics of the cell body itself, the modeling of which can be quite complicated (see Figure 1.13). Other models predict the biphasic dependence of speed on surface adhesiveness [141], which does not seem to hold true for *Dictyostelium*. A recent model addressing this issue suggested that the forces exerted by *Dictyostelium* cells are far in excess of what is required to pull off of the surface, and a limiting factor in motion is the disassembly time of adhesion bridges [116]. An overall model of cell adhesion and motility for *Dictyostelium* cells has not been produced.

The lack of basic answers to the question of how *Dictyostelium discoideum* collective behavior changes on surfaces of extreme adhesivities led to the work presented in Chapter 4, where individual and collective cell motion was quantified on different surfaces. Initial experiments performed with an actin-depolymerizing drug confirmed that our surfaces had very different cell-substrate adhesion properties. However, individual wild-type cells showed remarkable robustness in motility,
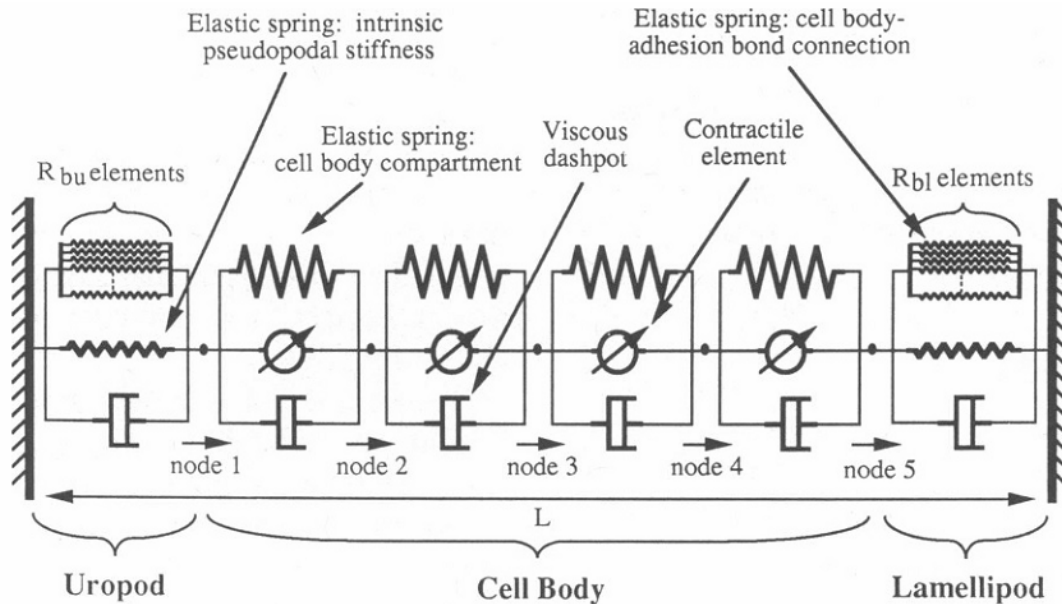
Figure 1.13 – Example Model of the Mechanics of Cell Motion and Cell-Surface Adhesion
Example model of cell body mechanics and adhesion. In this model, the cell body is treated as a one-dimensional structure composed of four compartments. The middle four compartments represent the cell body and contain a spring, dashpot, and contractile element in parallel. The lamellipod (cell front) and uropod (cell back) have springs and dashpots in parallel. In addition, the cell-surface receptor dynamics are only explicitly modeled in the lamellipod and uropod regions. This model predicts a biphasic dependence of cell speed on cell-substrate adhesiveness. *Figure reproduced from [141] with permission.*

migrating equally well on all surfaces tested. We noted that cells presented with an interface between surfaces of different adhesivity tended to migrate on the surface with less adhesivity. Finally, we allowed cells to aggregate on the surfaces and found a surprising result: although individual cells migrate equally on all surfaces, collective migration changes based on the surface adhesiveness: cells on very adhesive surfaces tend to prefer cell-cell contact over cell-surface contact. This system therefore displayed a remarkable emergent behavior that could not be inferred from investigating individual cells in isolation.

2. Bias in a Model of Eukaryotic Gradient Sensing

This chapter is adapted from a publication by Skupsky, McCann, Nossal, and Losert [73]. Section 2.3 summarizes and explains the mathematical model that is the subject of our stability analysis. This model, not part of the Dissertation research, was constructed by Ron Skupsky and others [35, 69] and will be referred to as 'our model'. It is placed here as understanding its development is critical to understanding the subsequent analyses. The research completed as part of this dissertation resumes with Section 2.4. Sections 2.4.1 – 2.4.3 are based on work presented in the dissertation of R. Skupsky [35].

2.1. *Summary*

We apply linear-stability theory and perform perturbation studies for the characterization of, and for the generation of new experimental predictions from, a model of chemotactic gradient sensing in eukaryotic cells. The model uses reaction-diffusion equations to describe 3' phosphoinositide signaling and its regulation at the plasma membrane. It demonstrates a range of possible gradient-sensing mechanisms and captures such characteristic behaviors as strong polarization in response to static gradients, adaptation to differing mean levels of stimulus, and plasticity in response to changing gradients. An analysis of the stability of polarized steady-state solutions indicates that the model is most sensitive to off-axis perturbations. This biased sensitivity is reflected in responses to localized external stimuli as well, and leads to a clear experimental prediction: a cell that is polarized in a background gradient will be

most sensitive to transient point-source stimuli lying within a range of angles that are oblique with respect to the polarization axis. Stimuli at angles below this range will elicit responses whose directions overshoot the stimulus angle, while responses to stimuli applied at larger angles will undershoot the stimulus angle. We argue that such a bias is likely to be a general feature of gradient sensing in highly motile cells, particularly if they are optimized to respond to small gradients. Finally, an angular bias in gradient sensing might lead to preferred turn angles and zigzag motions of cells moving up chemotactic gradients, as has been noted under certain experimental conditions [142].

2.2. *Introduction*

Chemotaxis, the process by which a cell moves in response to a chemical gradient, is essential for many biological functions, including the immune response of neutrophils, the growth of blood vessels, embryonic development, and the aggregation of the amoeboid cell *Dictyostelium discoideum* [143-147]. A proper response requires that the spatio-temporal information in a chemotactic stimulus be transduced into a redistribution of the cellular constituents that mediate the mechanical and morphological changes underlying cell movement [49, 56]. In highly motile cells, such gradient sensing involves adaptation to the spatial average of the experienced stimulus, highly polarized responses to small spatial gradients, and sufficient response plasticity for the cell to follow the direction of a changing gradient [148-151].

Recent experiments in both *Dictyostelium* and neutrophils have indicated that the spatial distributions of the molecules involved in signaling by 3' phosphoinositide (3'PI) lipids at the plasma membrane are correlated with both leading edge protrusion and the development of polarity in chemotaxing cells [38, 65, 152]. Similar patterns of molecular localization are seen in chemotactically stimulated cells that are round and immobile due to pharmacological poisoning of the actin cytoskeleton [50, 52], suggesting that aspects of gradient sensing can be decoupled from motility. These observations have motivated several mathematical models [70, 153-159], including a recent study in which Skupsky et al. developed a model of 3'PI-mediated gradient sensing that explicitly includes biochemical mechanisms at an intermediate level of detail [35, 69]. This model demonstrates a range of behaviors consistent with observations of characteristic gradient-sensing responses.

The complexity of chemotactic signaling poses many challenges to refined mathematical modeling. Currently, the number of testable model predictions remains small and the available experimental data are insufficient to characterize the pathway fully in any given cell type and to distinguish among possible mechanisms. Traditional experiments might measure the steady-state responses to a static gradient of chemoattractant and the response in time to uniform application of the same chemoattractant. Only recently are dynamic and more complex stimuli, such as rotating or alternating gradients, being used to probe gradient-sensing responses and their regulation [51, 52, 150, 156, 157].

Here we demonstrate the use of stability analysis and perturbation studies to identify types of dynamic stimuli to which a cell might be most responsive and that

might be best suited to probe cellular behaviors. In particular, our results indicate that a polarized cell should be most sensitive to off-axis perturbations. Such a biased sensitivity might be observed by measuring responses to localized stimuli applied on top of a background gradient, and is potentially a general feature of gradient sensing in highly motile cells.

We begin by introducing the model of eukaryotic gradient sensing by Skupsky et al. and linearizing its equations [35]. An analysis of responses to perturbations in the spatial distributions of *internal* variables about *uniform* steady-state solutions highlights different qualitative behaviors demonstrated by the model in different parameter regimes. Our results suggest that the decay rates of normal-mode perturbations about uniform solutions might be measured to characterize cellular gradient-sensing mechanisms, and we comment on the relationship of our results to those found in more general Turing-like systems. An analysis of responses to *internal* perturbations about *polarized* solutions indicates that the least stable modes are localized at an angle with respect to the polarization axis. Motivated by this result, we explore the angular dependence of the responses of the model to localized perturbations in the external stimulus. Our simulations of cellular responses to point source stimuli, applied at different angles with respect to a background linear gradient, demonstrate a maximal response to stimuli applied at an oblique angle with respect to the pre-established cellular polarization axis. We argue that such a biased sensitivity is in fact a general feature of gradient sensing in highly motile cells, and might result naturally if the cells are optimized to detect small chemotactic gradients.

Finally, we discuss how our results might relate to experimentally observed zigzag motions of immune cells moving up a chemotactic gradient [160].

2.3. _Summary of Prior Work_

2.3.1. Mathematical Model

Efficient gradient sensing depends on a complex network of regulatory interactions that couple dynamics on multiple length and time scales. In particular, the amplified response to a gradient involves localization of components to the up-gradient side of the cell, while response adaptation requires components that effectively integrate the external stimulus over the cell surface [49, 148]. In our model, because of differences in characteristic diffusion times, membrane-bound proteins (with minute-scale diffusion times) are treated as fixed, and effectively act locally, while cytosolic proteins (with sub-second-scale diffusion times) are treated as uniformly distributed, introducing a global coupling. However, lipid diffusion along the membrane (second-scale diffusion times) is explicitly calculated. The spatial patterns generated by lipids in our model thus depend on their regulated production and degradation.

The geometry of our model is a 2-D circle (Figure 2.1 A), which qualitatively captures gradient-sensing responses observed in pharmacologically immobilized _Dictyostelium_ cells. Below we briefly describe the particular components of our model and their regulation. Readers interested in a more detailed discussion are referred to [35, 69].
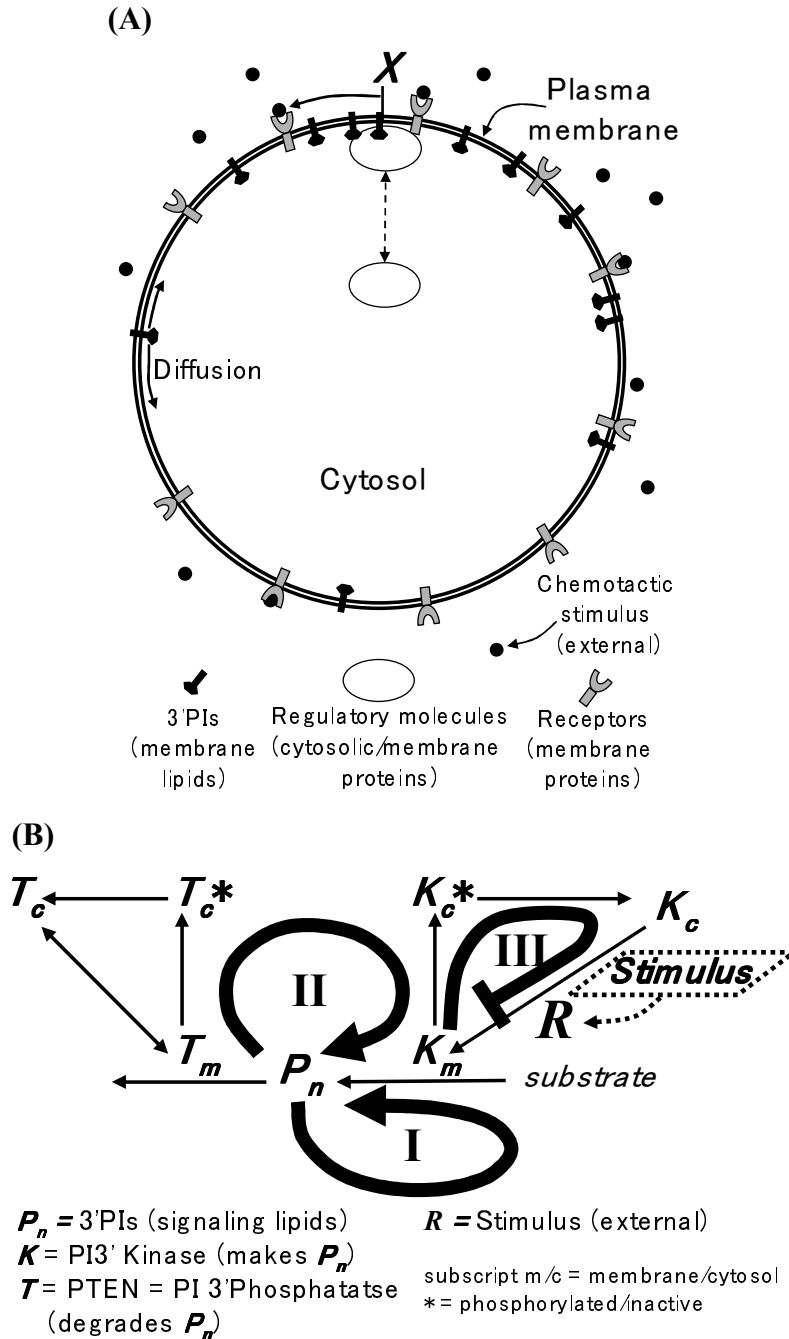
Figure 2.1 – Idealized Model of the Cell

Adapted from [69]. A) Geometry and components of the model. The cell is treated as a 2-D circle. The perimeter, marked by the normalized coordinate, *X,* represents the plasma membrane, along which 3'PI signaling lipids diffuse. Their spatial distribution is a primary output of our model. Regulatory proteins can exchange between the membrane and the cytosol, where they are considered to be uniformly distributed. A pattern of activated receptors on the cell surface, representing the outside stimulus, is taken as the input for our simulations. B) Variables and network topology. The single variable, *R,* represents the outside stimulus, which drives PI3K to the membrane. Positive feedback Loops I and II enhance generation of P_n (the 3'PI signaling lipids) through substrate delivery and enzyme regulation, respectively. Negative Feedback Loop III represents PI3K phosphorylation and removal from the membrane, leading to adaptation.

2.3.2. System Variables

The scaled variables of our model are indicated in Figure 2.1 B. They represent molecules that are thought to be important for gradient sensing and that have been visualized in live cells using fluorescent labeling techniques. Other significant regulatory molecules are implicitly included in feedback terms in our equations (see below).

The included lipids are the 3' phosphoinositides, $PI(3,4)P_2$ and $PI(3,4,5)P_3$, which are represented by the scaled model variables P_2 and P_3 (scaling factors are given at the end of this Chapter and discussed in [69]). These 3' phosphoinositides (3'PIs) are thought to act as binding sites for regulators of actin-based structures that generate force at the leading edge of chemotaxing cells [54, 65, 152, 161]. Their sum, denoted P_n, is a primary output of our model.

Proteins included in our model are 1) the enzyme that generates 3'PIs (a PI 3' kinase, abbreviated as PI3K and denoted by the scaled variable K) and 2) an enzyme that removes them (the PTEN phosphatase, denoted by the scaled variable T). In mammalian cells, phosphorylation is thought to be an important form of regulation for these enzymes [162, 163]. Thus, we will consider three pools of PI3K/PTEN. One pool, which is unphosphorylated and localized on the membrane, acts to generate/remove 3'PIs. A second unphosphorylated pool, which is cytosolic and thus assumed to be uniformly distributed in our model, can bind to the membrane. The third pool is also cytosolic and uniformly distributed, but is phosphorylated. Molecules in this pool require dephosphorylation in the cytosol to return to the membrane.

A single scaled variable, ***R***, is used to represent ligand-activated receptors and hetero-trimeric G-proteins at the cell surface, which together act to recruit PI3K from the cytosol to the membrane [54, 164, 165]. The 3'PIs, and PI3K and PTEN in different states, are the *internal* variables of our model, for which we will write dynamical equations. The distribution of ***R*** along the membrane, on the other hand, is set *externally*; it acts as the input for our simulations and is varied to represent different patterns of chemotactic stimuli.

2.3.3. Network Topology

The topological features of the regulatory network of our model (Figure 2.1 B) were inferred primarily from biochemical and microscopy data in *Dictyostelium* and/or neutrophils. Where biochemical details necessary to account for noted observations in gradient-sensing cells are unclear, mechanisms were proposed based on data for related cell types.

Loop I in Figure 2.1 B represents a positive feedback from 3'PI production to delivery of the substrate upon which PI3K acts to generate more 3'PIs. This feedback is thought to depend on the activities of small G-proteins, whose regulators bind to the membrane in a 3'PI-dependent manner [161, 166, 167]. Loop II is a proposed feedback from 3'PIs to localization of both the molecules that generate them and those that degrade them. This feedback accounts for the observation that during chemotactic response in *Dictyostelium*, PI3K translocation to the membrane parallels 3'PI accumulation, while PTEN translocation demonstrates an inverse dynamic [152,

168, 169]. PI3K recruitment to the membrane in response to *external* stimuli (**R**) drives Loops I and II, which together act to amplify cellular responses in our model.

Response adaptation is necessary for cells to sense chemotactic gradients over many orders of magnitude in the absolute concentration. The mechanisms that account for this adaptation currently are unknown, but are thought to act downstream from receptor and G-protein activation [51, 54, 150, 170]. For our model, we have proposed that in response to chemotactic stimuli, PI3K that is recruited from the cytosol to the membrane is subsequently phosphorylated such that it no longer binds to the membrane (negative feedback Loop III in Figure 2.1 B). The cytosolic pool of unphosphorylated PI3K that can be recruited to the membrane is thus depleted. This adaptation mechanism contains a global element because it involves regulation of a cytosolic variable.

2.3.4. Model Equations and Modular Interpretation

Our model consists of a set of reaction-diffusion equations describing the dynamics of its scaled model variables. Linear mass-action kinetics have generally been assumed, with more complex terms included to account for feedback regulation by molecules whose dynamics are not well characterized. Integrals in our equations arise because we have treated the cytosol as uniform, exchanging material with the entire membrane simultaneously. The spatial variable, X, is normalized to the range $[0,1]$ and is periodic (Figure 2.1 A). Here, we briefly discuss the major terms and parameters representing regulatory interaction in our model equations. A more detailed discussion, as well as derivations, can be found in [69].

In what follows, the subscripts m/c denote membrane-bound/cytosolic, and '*' indicates phosphorylated species, which are inactive. The parameters χ generally represent scaled forward rate constants, λ represent backwards rate constants, and κ provide saturation concentrations and/or concentrations at which a particular term becomes effective. The parameters ζ designate additional constitutive processes beyond the scope of our model (see also the end of this Chapter).

The following equations describe the dynamics of the lipids included in our model:

$$\frac{\partial P_3}{\partial t} = \chi_3 K_m \left(\frac{\Xi}{1 + K_m / \kappa_3} + \zeta_{3/PITP} \right) + \zeta_3 - \lambda_3 P_3 \left(T_m + \zeta_{3/T} \right) + D \frac{\partial^2 P_3}{\partial X^2}, \tag{2.1}$$

where

$$\Xi \equiv \frac{P_n}{\underbrace{P_n / \kappa_m + \int_0^1 P_n dX / \kappa_c + 1}_{Loop\ I}} + \zeta_{PITP} \tag{2.1a}$$

with

$$P_n \equiv P_3 + P_2, \tag{2.1b}$$

and

$$\frac{\partial P_2}{\partial t} = \zeta_2 + \lambda_3 \zeta_{3/T} P_3 - \lambda_2 P_2 \left(T_m + \zeta_{2/T} \right) + D \frac{\partial^2 P_2}{\partial X^2}. \tag{2.2}$$

Equation 2.1 states that P_3 is generated by the action of membrane-bound PI3K (K_m) on its substrate. The factor Ξ (defined in Eq. 2.1a and derived in [35]) represents 3'PI-mediated enhancement of substrate delivery (Loop I). In the denominators, the term K_m / κ_3 represents a Michaelis-Menten-like saturation of P_3 production at high

values of K_m, while the terms $\int_0^1 P_n dX / \kappa_c$ and P_n / κ_m represent saturation at high

values of P_n due to depletion of cytosolic and membrane-bound regulatory molecules.

Equation 2.1 also includes degradation of P_3 by PTEN on the membrane (T_m), as well

as lateral diffusion of P_3 along the membrane. Equation 2.2 describes P_2 production

from P_3 and its removal by T_m, such that P_2 dynamics generally follow P_3 with a

slight lag.

The following equations describe the dynamics of proteins on the membrane:

$$\frac{\partial K_m}{\partial t} = \lambda_K (\gamma - \frac{K_m}{1 + \underbrace{P_n / \kappa_K}_{Loop\ II}}),$$

(2.3)

where

$$\gamma \equiv (\chi_K / \lambda_K)(R + 1) K_c;$$

(2.3a)

$$\frac{\partial T_m}{\partial t} = \chi_T T_c - \lambda_T \underbrace{T_m (K_m}_{Loop\ II} + \zeta_T)$$

(2.4)

In Eq. 2.3, the rate of PI3K recruitment from the cytosol to the membrane (first term)

is proportional to the product of cytosolic PI3K (K_c) and the outside stimulus (the

factor (R+1) includes both the effect of the outside stimulus and a constitutive

activation term). This product, which we label γ (see Eq. 2.3a), defines a driving

parameter for our model (discussed further below), coupling its responses to outside

stimuli and driving its positive feedbacks (Loops I and II, see Figure 2.1 B). The rate

of K_m removal from the membrane by phosphorylation (second term) is decreased

with increasing P_n, resulting in a PI3K translocation that parallels 3'PI production

(we have postulated a regulatory molecule that binds 3'PIs, as discussed in [69]).

This feedback is represented by Loop II in Figure 2.1 B, and becomes effective when P_n is of order κ_K. The first term in Eq. 2.4 describes PTEN translocation from the cytosol to the membrane (i.e., the production of T_m from T_c). PTEN removal from the membrane is enhanced by a postulated K_m-induced phosphorylation (second term), which further enhances 3'PI production and results in a T_m dynamics inverse to that of K_m (also represented by Loop II in Figure 2.1 B and discussed further in [69]).

The following equations describe the dynamics of cytosolic proteins in our model:

$$\frac{\partial T_c}{\partial t} = \lambda_{T*} T_c * -\chi_T \int_0^1 T_c dX / A_{cell} , \tag{2.5}$$

$$\frac{\partial K_c}{\partial t} = \frac{\lambda_{K*} K_c *}{\kappa_{K*} + K_c *} - \lambda_K \int_0^1 \gamma dX / A_{cell} \tag{2.6}$$

$$\sim \left(\lambda_K / A_{cell} \right) \left(\gamma_0 - \int_0^1 \gamma dX \right), \tag{2.6a}$$

with

$$\gamma_0 \equiv \frac{A_{cell} \lambda_{K*}}{\lambda_K} , \tag{2.6b}$$

where A_{cell} is the area of our two-dimensional cell, equal to $1/4\pi$ in units where the circumference of the cell is 1. Equation 2.5 describes production of T_c from T_c* (i.e. dephosphorylation of PTEN in the cytosol, first term) and subsequent recruitment to the membrane (second term). Equation 2.6 describes production of K_c from K_c* (PI3K dephosphorylation in the cytosol, first term) and PI3K recruitment to the entire membrane (second term). In what follows, parameters are set such that the reaction

that dephosphorylates PI3K in the cytosol is saturated and the approximation in Eq. 2.6a is valid.

Our system is closed by the following two equations, which fix the total amount of PI3K and PTEN in the cell (scaled to 1).

$$1 = \boldsymbol{K}_c A_{cell} + \boldsymbol{K}_c * A_{cell} + \int_0^1 \boldsymbol{K}_m dX \qquad (2.7)$$

$$1 = \boldsymbol{T}_c A_{cell} + \boldsymbol{T}_c * A_{cell} + \int_0^1 \boldsymbol{T}_m dX \qquad (2.8)$$

Equations 2.1 – 2.5 effectively describe an amplification module in our model, coupled to outside stimuli and driven by the product, $\boldsymbol{\gamma}$ (see Eq. 2.3a). Equation 2.6 describes response adaptation and yields an equation for the dynamics of $\boldsymbol{\gamma}$ at constant $\boldsymbol{R}$ via multiplication by $(\chi_K / \lambda_K)(\boldsymbol{R}+1)$. The approximation of Eq. 2.6a thus implies that the average value of the driving parameter over the membrane ($\int_0^1 \gamma dX$) always returns to a baseline value defined by γ_0 (see Eq. 2.6b).

2.3.5. Response to Uniform Stimuli and Stationary Gradients

Characteristic responses of our model are shown in Figure 2.2. A uniform stimulus applied suddenly (Figure 2.2 A) is represented by a uniform increase in $\boldsymbol{R}$, and hence an increase in the driving parameter, $\boldsymbol{\gamma}$. The components of the amplification module respond approximately in phase: PI3K is recruited to the membrane ($\boldsymbol{K}_m$), PTEN ($\boldsymbol{T}_m$) is removed, and 3'PIs ($\boldsymbol{P}_n$) are generated. Eventually, Loop III-mediated phosphorylation of PI3K (see Figure 2.2 B and discussion below) begins to deplete the cytosolic pool of unphosphorylated PI3K ($\boldsymbol{K}_c$) that can be

recruited to the membrane, such that the driving parameter is returned to its baseline, resting, value and the response subsides (see Eq. 2.6a). If, however, the stimulus is applied in a gradient (Figure 2.2 B), the pool of cytosolic PI3K is depleted such that only the *average value* of the driving parameter returns to its resting value. In the front of the cell, however, receptor activity is elevated and the value of γ remains above baseline. The amplification module continues to be driven, generating a localized 3'PI signal. The reverse is true at the back of the cell. These model responses are in qualitative agreement with experimental observations of fluorescently labeled *Dictyostelium* cells responding to chemotactic stimuli.

2.3.6. Choice of Parameters: Representative Case

Many details of the mechanisms involved in gradient sensing remain to be elucidated and, even where molecular pathways are known, most of the relevant biochemical parameters have not been directly quantified in cellular contexts. Thus, we have set the parameters of our model empirically to reproduce observations of characteristic gradient-sensing responses such as those that were illustrated in Figure 2.2. We study in particular four sets of parameters (given at the end of the Chapter), for which our model demonstrates qualitatively different gradient behaviors (see [35] for further discussion). The results for these representative parameter sets provide an indication of the generality of our results.

(A)

(B)
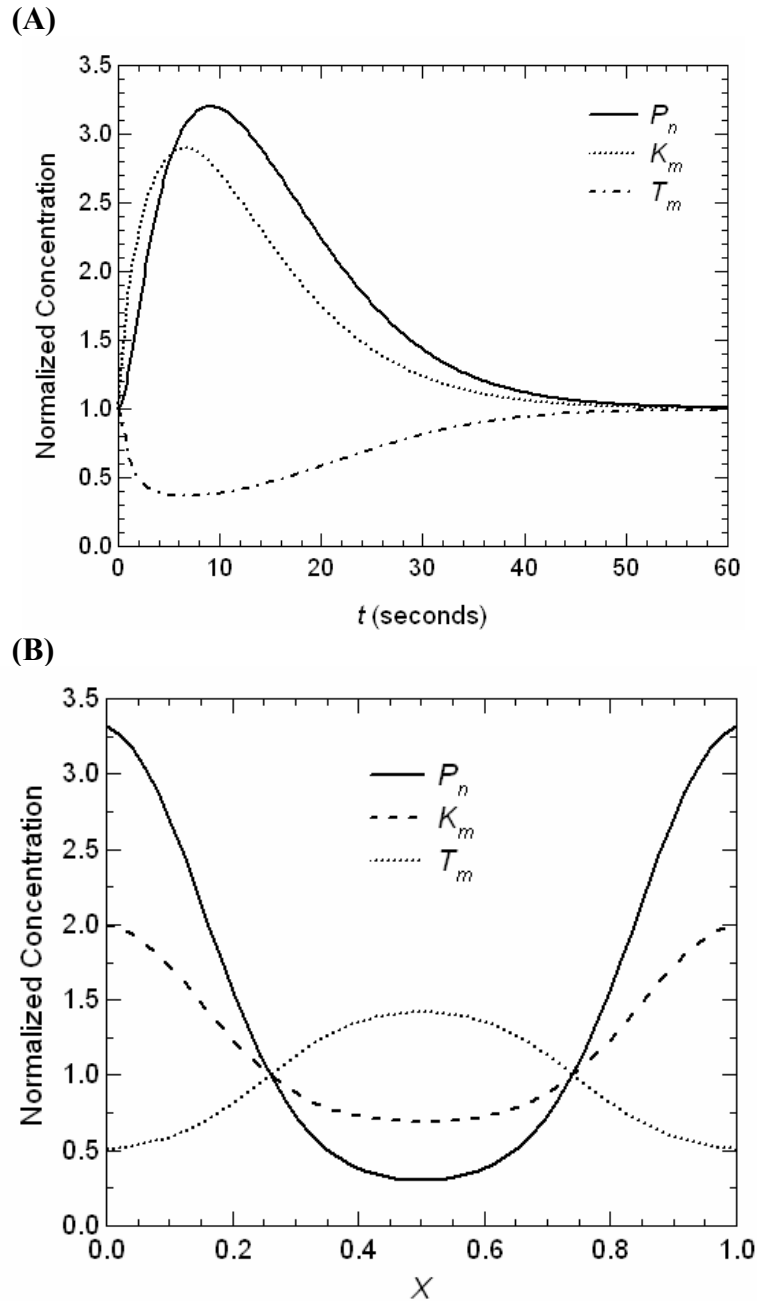
Figure 2.2 - Characteristic Gradient-Sensing Responses
A) Transient response to a uniform stimulus. At time t = 0, the external variable, R, is uniformly increased, representing a uniform step stimulus. The figure shows the transient, in-phase responses of the model variables, normalized by their values prior to the stimulus. B) Steady-state polarized response to a gradient. The steady-state profile of the model variables (again normalized by their values in the resting cell) arising in response to a small gradient in R that represents a spatially linear gradient in the outside stimulus, where the gradient lies along the X = 0/X = 1 direction (the spatial variable, X, is normalized and periodic).

58

2.4. *Stability Analysis*

We now attempt to address the following questions: How does our model respond to perturbations about its steady-state solutions? Will it relax back to the previous state or move to a new one? Will some perturbation shapes dominate responses? To what patterns of stimuli is a gradient-sensing cell likely to be most sensitive? To answer these questions, we now perform a linear-stability and perturbation analysis.

2.4.1. Linearized Equations

We begin by considering *internal* perturbations in our six model variables, whose dynamics are described by Eqs. 2.1 – 2.6. For our analysis here, we collect these variables in a vector, $\check{U}(X,t)$, which is the sum of a steady-state solution ($\check{U}_0(X)$) and a perturbation about that solution ($\delta\check{U}(X,t)$), i.e.,

$$\check{U}(X,t) = \check{U}_0(X) + \delta\check{U}(X,t). \tag{2.9}$$

Note that for cytosolic variables, which are assumed to be spatially uniform, the spatial dependence is trivial. In order to collect same-order terms in our perturbations, and in anticipation of a 'normal-mode' analysis to follow, we write our perturbations in the form

$$\delta\check{U}(X,t) = \varepsilon\check{A}_j(X)\exp(\sigma_j t) \tag{2.10}$$

where ε is small and the index, j, specifies a normal-mode solution with growth rate, σ_j, and spatially dependent amplitude, $\check{A}_j(X)$. Solutions of this form are inserted into Eqs. 2.1 – 2.6, which are expanded in orders of ε, and only lowest order terms in

ε are retained. The resulting system of linearized equations represents an eigenvalue problem, and can be written in the form

$$s_j \overset{\vee}{A}_j = \overset{\backprime}{A} \, \overset{\vee}{A}_j.$$
(2.11)

Here, $\overset{\backprime}{A}$ is a linear operator, and we must solve for the growth rates, σ_j, and the normal-mode perturbations, $\overset{\vee}{A}_j(X)$. In terms of our model variables, we find the following system of equations:

$$\sigma_j \hat{P}_{n,j} = \frac{\chi_3 K_m}{\left(1 + K_m / \kappa_3\right)} \hat{\Xi} + \chi_3 \left(\frac{\Xi}{\left(1 + K_m / \kappa_3\right)^2} + \zeta_{3/PITP} \right) \hat{K}_{m,j}$$

$$- \left(\lambda_3 P_3 + \lambda_2 P_2\right) \hat{T}_{m,j} - \lambda_3 T_m \hat{P}_{n,j} + \left(\lambda_3 T_m - \lambda_2 \left(T_m + \zeta_{2/T}\right)\right) \hat{P}_{2,j} + D \frac{\partial^2 \hat{P}_{n,j}}{\partial X^2}$$
(2.12)

where $\hat{\Xi} \equiv \dfrac{\left(1 + \int_0^1 P_n dX / \kappa_c\right) \hat{P}_{n,j} - P_n \int_0^1 \hat{P}_{n,j} dX / \kappa_c}{\left(P_n / \kappa_m + \int_0^1 P_n dX / \kappa_c + 1\right)^2}$
(2.12a)

and Ξ was defined in Eq. 2.1a;

$$\sigma_j \hat{P}_{2,j} = \lambda_3 \zeta_{3/T} \hat{P}_{n,j} - \lambda_2 P_2 \hat{T}_{m,j} - \left(\lambda_3 \zeta_{3/T} + \lambda_2 \left(T_m + \zeta_{2/T}\right)\right) \hat{P}_{2,j} + D \frac{\partial^2 \hat{P}_{2,j}}{\partial X^2};$$
(2.13)

$$\sigma_j \hat{K}_{m,j} = \lambda_K \int_0^1 \hat{\gamma} dX + \frac{\lambda_K K_m / \kappa_K}{\left(1 + P_n / \kappa_K\right)^2} \hat{P}_{n,j} - \frac{\lambda_K}{1 + P_n / \kappa_K} \hat{K}_{m,j};$$
(2.14)

$$\sigma_j \hat{T}_{m,j} = \chi_T \int_0^1 \hat{T}_c dX - \lambda_T T_m \hat{K}_{m,j} - \lambda_T \left(K_m + \zeta_T\right) \hat{T}_{m,j};$$
(15)

$$\sigma_j \hat{T}_c = -\left(\lambda_{T*} - \lambda_T \zeta_T\right) \int_0^1 \hat{T}_m dX / A_{cell} - \left(\chi_T / A_{cell} + \lambda_{T*}\right) \hat{T}_c;$$
(16)

$$\sigma_0 \hat{\gamma} \sim -\left(\chi_K / A_{cell}\right)\left(R + 1\right) \hat{\gamma}.$$
(17)

Equations 2.12 – 2.17 are the linearized counterparts of our six model equation

(Eqs. 2.1 – 2.6). Here, we have eliminated the variable P_3 in favor of P_n via Eq. 2.1b

(see Eq. 2.12), and we have written K_c in terms of the driving parameter, γ, via Eq.

2.6a (see Eq. 2.17). In the above, model variables with a '^' represent the components

of our normal-mode perturbations, while variables without a '^' represent the steady-

state profiles about which we perturb. Both can be spatially dependent; we will find

in the next subsection that the system is greatly simplified if we consider

perturbations about uniform solutions. It must be emphasized that the stability

analyses here are performed with respect to the *internal* distribution of the model

variables, and the *external* signal, represented by R, is assumed to be fixed.

2.4.2. Stability of Uniform Solutions

Studying the linearized response of our system to *internal* perturbations about

uniform steady-state solutions highlights some of qualitative gradient-sensing

possibilities demonstrated by our model. At the end of this subsection, we will

discuss how the linear stability properties of our equation set might be related to more

general models of Turing-type systems, and how they might be studied

experimentally.

Consider the case in which the unperturbed profile is a uniform steady-state

solution, for which a harmonic spatial dependence of the perturbations can be

assumed:

$$\overset{v}{\hat{A}}_j(X) = \overset{v}{\hat{a}}_j \exp\left(i2\pi j X\right).$$

(2.18)

Here, $\overset{\vee}{a}_j$ is a constant vector of perturbation components, 'i' is the imaginary unit, and the "wave number" 'j' must be an integer so that $\overset{\vee}{A}_j(0) = \overset{\vee}{A}_j(1)$. Under these conditions, Eqs. 2.12 – 2.17 become greatly simplified, such that the linear operator $\overset{\iota}{A}$ in Eq. 2.11 can now be written as a 6×6 matrix for each j, and its action on $\overset{\vee}{A}_j(X)$ in Eq. 2.11 amounts to matrix multiplication. The matrix, which we now denote as $\overset{\iota}{\mathfrak{I}}_j$, is initialized using uniform steady-state solutions to Eqs. 2.1- 2.6. Normal modes are calculated using SciPy [171], an open-source scientific toolkit for the Python programming language (www.python.org).

For each j, we expect to find 6 eigenvalues and eigenvectors, corresponding to 6 growth rates and normal modes. The mode with the largest growth rate determines the stability of our solutions, and this mode is likely to dominate responses to the most general perturbations. In what follows we only discuss this mode for each j (i.e., we do not include an extra index to enumerate the six solutions at each j), and we will refer to it as the '*least stable*' mode for that j. If the growth rate for this mode is negative, then we can conclude that the system is stable to all perturbations of that wavelength. On the other hand, if the calculated growth rate is found to be positive, then perturbations of that form will grow and the system is unstable to those perturbations.

In Figure 2.3 we plot growth rates of the least-stable normal-mode perturbations over a range of j. Results are shown for the four representative sets of model parameters (labeled as Cases 1 – 4) that were discussed above and characterized in previous work [69]. We note here several general features of our

results, as well as several features that highlight the characteristic differences among the analyzed Cases.

Amplification and adaptation become decoupled in our normal-mode analysis (as can be seen from the form of Eq. 17). In particular, the calculated least-stable modes are composed primarily of perturbations in the components of the amplification module, with $\hat{\gamma} \sim 0$ (data not shown). Further, for these least-stable normal modes, the membrane-bound components of the amplification module are always found to be approximately in phase, reinforcing each other as they do in response to external stimuli (see Figure 2.2). That is, $\hat{P}_{n,j}$, $\hat{P}_{2,j}$, and $\hat{K}_{m,j}$ all have the same sign, while $\hat{T}_{m,j}$ has the opposite sign. If any of these variables are held fixed, such that the corresponding perturbation component is set to 0, the calculated growth rates are always reduced (not shown).

We see in Figure 2.3 that σ_0 is always negative. Thus, the uniform system is always stable to uniform perturbations. More specifically, this is a requirement for the system to demonstrate a transient response followed by adaptation to all uniform stimuli (parameter values were always chosen such that this condition holds). On the other hand, $\sigma_1 > \sigma_0$ is possible because in our linearized equations integrals of perturbation components, which generally account for cytosolic depletion, vanish for $j \neq 0$. Conceptually, cytosolic depletion saturates the activity of positive feedback loops in response to uniform perturbations $(j = 0)$, while in response to non-uniform perturbations $(j \neq 0)$ this depletion is avoided by a redistribution of molecules on the membrane. Thus, we see in Figure 2.3 that $\sigma_1 > \sigma_0$ only for Cases 2 and 4. These

Cases were designed to illustrate conditions under which depletion of translocating molecules from the cytosol saturates uniform responses, but redistribution of these molecules on the membrane effectively amplifies non-uniform responses. Further, $\sigma_1 > 0$ is possible, as is demonstrated by Case 4 in Figure 2.3. This means that the uniform state is unstable to small perturbations that induce polarization (i.e., those with $j = 1$). Case 4 includes both strong, coupled, positive feedbacks and amplification of non-uniform responses by redistribution of translocating molecules; in previous work we had characterized this Case as demonstrating a finite polarization in response to infinitesimal applied gradients in the external stimulus [69]. A model in this regime might relate to the spontaneous polarization in response to uniform stimuli that is demonstrated by some motile cells (this is referred to as chemokinesis, and requires cytoskeletal dynamics for full explanation). Finally, $\sigma_i < \sigma_j$ for $i > j \geq 1$, as is demonstrated by all four Cases in Figure 2.3. These relations means that higher spatial modes, which are subject to greater dissipation from diffusion, decay more quickly. Thus, $\sigma_1 < 0$ means $\sigma_j < 0$ for all j, and we can infer from Figure 2.3 that the uniform state is stable to all perturbations for Cases 1 – 3.

We place our analysis in the more general context of pattern forming systems by noting that Case 4 demonstrates a Turing-type instability [172-174]. Indeed, gradient sensing responses in our model depend on a competition between activator molecules that drive the response at the leading edge of the cell (i.e. P_3, P_2, K_m, and T_m, which are the membrane-bound components of our model), and those whose depletion inhibits that response (i.e. K_c and T_c, as well as other cytosolic components that are implicitly included in feedback terms, see [35]). Differences among the
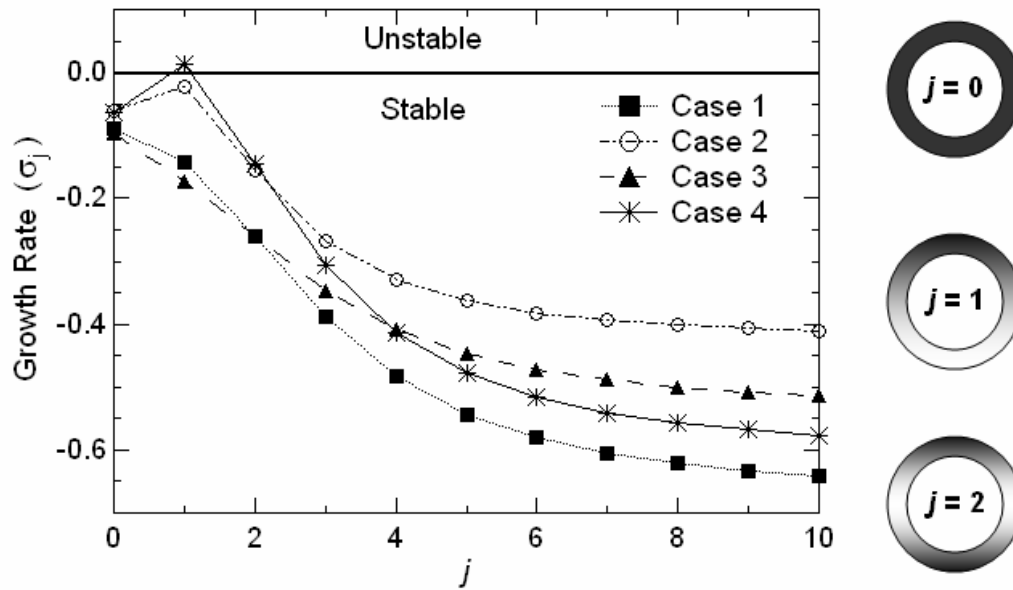
Figure 2.3 - Stability of Uniform Steady-State Solutions

Growth rates, σ_j, are plotted for least-stable perturbations with spatial wave numbers indicated by the index, j, about uniform steady-state solutions. The system is stable towards perturbations with negative growth rate, but unstable when σ_j is positive. The grey scale cartoons indicate the shape of the first few spatial modes around the membrane. The four Cases analyzed represent the qualitatively different response-amplification mechanisms that had been analyzed with the model.

diffusion coefficients of these components make instability possible. While Cases 1-3 are stable, they are nevertheless defined near bifurcations where instability begins to occur; we generally found gradient sensing to be most efficient in regions of parameter space near such bifurcations (the dependence of model response on variations of key model parameters is analyzed in [35], though stability is not directly addressed there). For combinations of parameters that do lead to instability in our model, single peaked patterns are always favored (i.e. $j = 1$, see Figure 2.3).

If finite diffusion coefficients were to be considered for cytosolic components in our model (recall that we had considered cytosolic diffusion to occur instantaneously), a Turing instability could generate multi-peaked patterns on a

length-scale determined by the decay length of the inhibitory effects of the cytosolic depletion near regions of membrane activation. However, robust multi-peaked patterns in our model also require either a decrease in the membrane lipid diffusion coefficient or consideration of a larger cell (see [175] for a discussion of Turing patterns in cellular geometries). While simpler Turing-type systems (e.g. those involving only two components) have been well characterized mathematically and find application in diverse areas of study [172, 175, 176], our model does not map directly onto these.

In real cells, the values of σ_0 and σ_1 perhaps could be directly measured in response to internal perturbations generated by experimental techniques such as photo-uncaging. Alternately, thermal fluctuations, or fluctuations due to interactions with other cellular components not included in the model, can act as internal perturbations; experimental observations of fluctuations in the concentrations of model components could thus be used to calculate perturbation decay rates. Finally, cellular responses to small perturbations in the *external* stimulus could act to generate observable perturbations in the distributions of *internal* cellular components. In what follows, we will continue to see that our model's responses to *internal* and *external* perturbations mirror one another.

2.4.3. Stability of Polarized Solutions

How does our model respond to small internal perturbations when the initial profile of signaling molecules is *polarized*, rather than uniform? To investigate this question, we initialize our model in its uniform steady state in the absence of stimuli

and then externally apply a small, static, spatially linear gradient, whose effect on receptor activity is described by:

$$\left\{ \mathbf{R} = 0, \ (t < 0); \ \mathbf{R} = S + G\left(1 + S\right)\cos\left(2\pi X\right), \ (t > 0)\right\}.$$ (2.19)

Here, S measures the average receptor activity that results from the applied stimulus and G measures the relative difference in receptor activity between the front and midline of the cell. In what follows, we consider $G = 0.05$ and $S = 2$, conditions that are sufficient to elicit a highly polarized response in our model (a range of gradients gave the same qualitative results and the steady state is independent of S). The system is evolved to steady-state via Eqs. 1-6 using FiPy, a finite volume partial differential equation solver (developed at the National Institute of Standards and Technology, Gaithersburg MD). The resulting polarized solutions then become the unperturbed profiles in Eqs. 12 – 17, which must now be solved assuming a general spatial dependence for the calculated normal-mode perturbations. The spatial variable, X, is represented by discrete values, a finite difference approximation is used to approximate diffusion terms, and quadrature is used to approximate integrals. In this way, we once again arrive at a matrix representation for our linearized system and solve it by the same methods as laid out above. Again, we focus on the features of the least-stable normal-mode perturbations.

Figure 2.4 A shows the $\mathbf{P_n}$ distribution for the two least-stable normal-mode perturbations in a representative computation. The calculated growth rates are negative, indicating that the system is stable towards all perturbations about this polarized solution. Further, the second normal-mode perturbation decays

significantly faster than the first, indicating that the least-stable mode is likely to dominate responses to general perturbations.

A profile of the model components for the least-stable mode is illustrated in more detail in Figure 2.4 B. We see here that the system is most sensitive to *internal* perturbations in which the model components again reinforce each other in approximately the same relationship that is demonstrated in response to the initially applied *external* gradient (illustrated in Figure 2.2 B), and as was found in our analysis of internal perturbations about uniform solutions (see discussion above). In addition, we note that the peaks in the perturbation profile occur at an angle of ~60 degrees to the direction of the initial applied gradient.

The above-noted features of the response to internal perturbations about polarized solutions were found for all Cases over a range of initial gradients (data not shown), suggesting that they reflect general features of gradient sensing as described by our model. In particular, the off-axis peaks in the spatial profile of the least-stable normal-mode perturbations indicate that the gradient-sensing response of a polarized cell should be most sensitive to perturbations localized at approximately 60 degrees with respect the polarization axis. Such a biased sensitivity, when coupled to cell motility, might cause a cell to turn at prescribed angles when moving up a shallow gradient, as has been observed for polymorphonuclear (PMN) leukocytes undergoing chemotaxis [142]. This bias will be discussed further below.

(A)

(B)
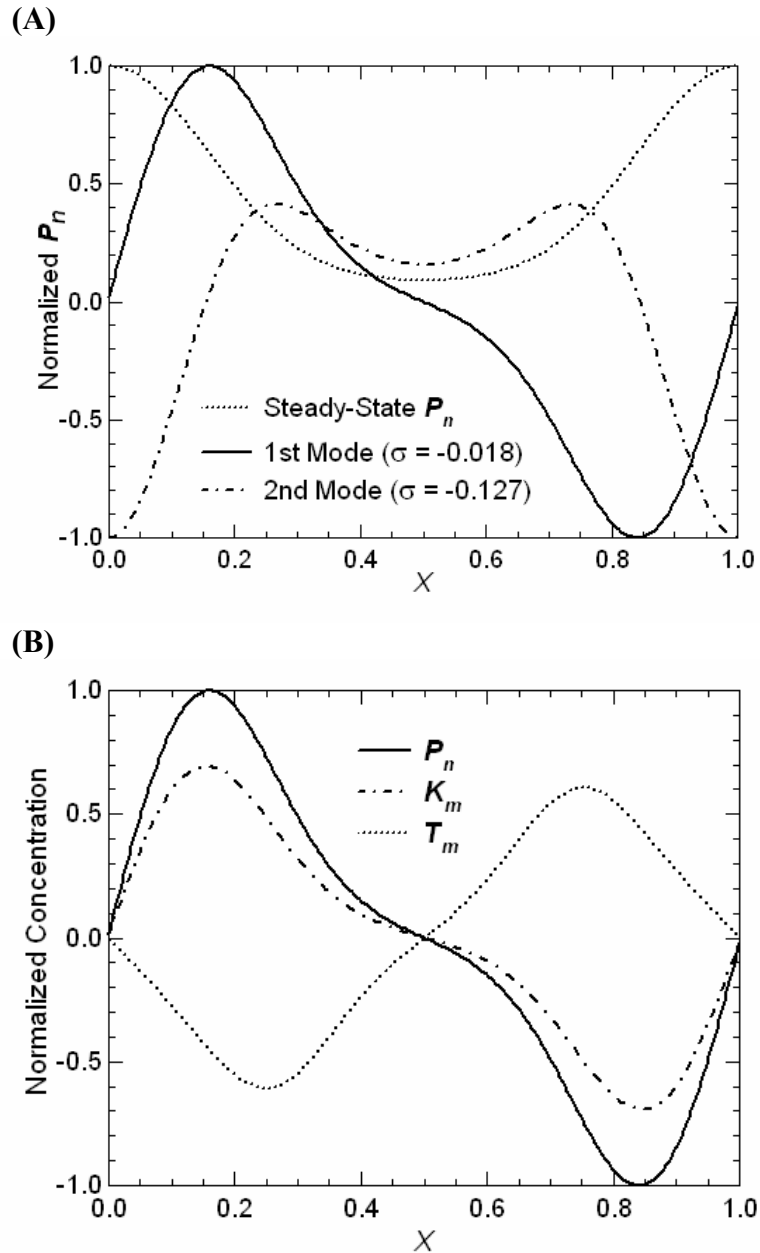
Figure 2.4 - Stability of Polarized Solutions
A) Representative P_n profiles and growth rates (σ) are indicated for the two least stable internal perturbation shapes about the polarized steady-state solution that results from application of a small background gradient in receptor activity. The least stable mode (1st mode) is peaked at approximately 60 degrees with respect to the background gradient and the peak in the steady-state profile (identical to that shown in Figure 2.2 B), indicating an enhanced sensitivity to off-axis perturbations. The 2nd mode decays much more quickly than the 1st, indicating that the least stable mode is likely to dominate responses to internal perturbations. Background (steady-state) and perturbation profiles are normalized so that their peak value is 1. B) P_n, for the least stable perturbation (1st mode), shown with the other model variables. Each variable is scaled by its value in the resting cell and then the entire mode profile is scaled so that the peak P_n value is 1. Plotted results pertain to Case 4, but qualitatively similar results were found for all four Cases, over a range of background gradients.

2.4.4.   Responses to Point Source Stimuli

How does our analysis of cellular responses to *internal* perturbations about steady-state solutions inform us about responses to *external* stimuli, which might be more easily measured experimentally? Does the enhanced sensitivity to off-axis *internal* perturbations that was demonstrated for the *linearized* behavior of our model in the previous subsection imply an enhanced sensitivity to off-axis *external* stimuli when the full *non-linear* response is considered? We might expect this to be the case because an external stimulus acts to perturb the internal variables for our model, and responses to internal perturbations mirror responses to external stimuli, as was noted in the previous two subsections.

To investigate the responsiveness of polarized cells to localized *external* perturbations, that is, to perturbations in the external stimulus, we simulate responses to a 'spike' of chemoattractant, as illustrated in Figure 2.5 A. A shallow background gradient is applied to initialize the system in a polarized steady-state solution, as above. A point-source stimulus, assumed to be a delta function in both space and time, is then released at a point outside of the cell and allowed to diffuse freely. Assuming a linear relationship between chemoattractant concentration at the cell surface and receptor activation in our model, the resulting 'perturbation' in $\boldsymbol{R}$ can be written as:

$$\Delta \boldsymbol{R} = (A/t)\exp\left(-|\vec{r} - \vec{r'}|^2 / 4Dt\right) \tag{2.20}$$

where $\vec{r}$ specifies a point on the cell surface (in 2 dimensions) and A specifies the 'strength' of the point source, released at $t = 0$, at position $\vec{r'}$ (assumed to be in the plane of the cell and measured from its center). The diffusion coefficient, D, was

70

fixed at 300 μm^2/sec, a value appropriate to a small-molecule chemoattractant such as cAMP (to which *Dictyostelium* responds). A point source stimulus of this type might approximate a bursting vesicle releasing its contents, which has been proposed as a method for cell-cell signaling in *Dictyostelium* [106].

We considered a range of A, sufficient to cause a peak increase in P_n by 1% to 150% of the background profile maximum. The position of the point source was varied from the cell surface to 15 cell lengths from its center (our model cell can be considered to have a diameter of order 8 μm), and its direction, labeled φ (see Figure 2.5 A), was varied from 0 to 180 degrees with respect to the direction of the background gradient. For each location, the full response of our model was simulated via Eqs. 2.1 – 2.6, again using FiPy, and a time-course was recorded.

In our simulations, the maximum stimulus from the 'spike' reaches the cell and is significantly dissipated within a few seconds. The cellular response is generally maximal after approximately 5 – 10 s and decays after approximately 20 -30 s until the initial steady state is reestablished. A sample profile is shown in Figure 2.5 B for the time point at which the response is maximal. The point source here is described by $|\vec{r}| = 5$ cell lengths, $\varphi = 36$ degrees, and A eliciting approximately a 25% maximal increase in P_n over the background profile. The variable representing the cellular response in the plot, ΔP_n, is the change in P_n from the background profile that is caused by adding the point source over the background gradient. In this instance, the peak in ΔP_n occurs at an angle, $\theta_{max} \sim 58°$, which is greater than the source angle, φ; i.e., the cell response overshoots the angle of the external stimulus. The complete time-course of ΔP_n at angle θ_{max}, at φ, and at two representative off-peak angles, is

71

shown in Figure 2.6 for this simulation; the magnitude of the peak response increases with increasing strength of the point source, as shown in the inset. We see that large perturbation responses are possible (a model including cytoskeletal dynamics would be necessary to identify that magnitude of perturbation that would have a significant effect on the path of a moving cell). Other qualitative features of the response, such as its shape and the position of the maximum in $\Delta \boldsymbol{P_n}$, were found to be similar over a range of point-source distances ($|\overset{v}{r'}|$) and strengths (A) for all four Cases (results not shown).

To investigate any possible angular bias in our model's responses to the above 'spike' stimuli, we systematically varied the point-source angle, φ, keeping the point-source distance and strength fixed as in Figure 2.5 B. Figure 2.7 records the magnitude and direction of the maximal response from the time-courses for each simulation as a function of the point-source angle. We see in Figure 2.7 A that all four Cases respond maximally to stimuli released at angles between approximately 40 and 80 degrees with respect to the background gradient. Figure 2.7 B indicates that when the source angle, φ, is below this range, the maximum response of the cell occurs at an angle θ that is greater than φ, i.e. the response overshoots the direction of the stimulus perturbation. On the other hand, for larger φ the angle of the maximum response is less than φ, i.e. the response now undershoots the angle of the applied stimulus. Again, the qualitative features of these results were not found to depend on the distance or strength of the point source. As shown in Figure 2.8 and

(A)

(B)
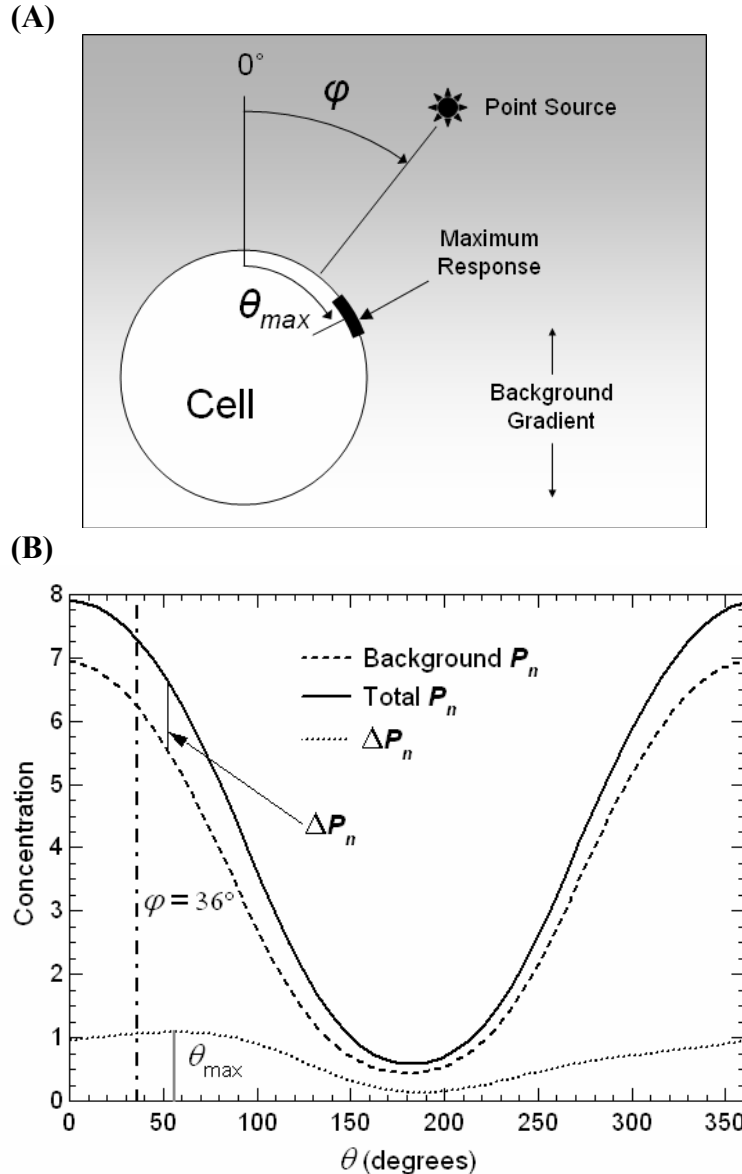
Figure 2.5 – Point Source Simulations
A) Simulation geometry. The cell is first allowed to equilibrate to a small external linear gradient, as in Figure 2.4. A point source in space and time is then released at an angle, φ, with respect to the background gradient, and the response in time is recorded. θ_{max} measures the direction of the peak response on the membrane. B) Time response. The spatial profile at the time of maximal response to a point source released at $\varphi = 36$ degrees, is plotted. ΔP_n indicates the difference between the instantaneous P_n distribution ('Total P_n') and the steady-state profile ('Background P_n'). Notice that the peak in ΔP_n, θ_{max}, is at an angle greater than 36 degrees, i.e. the response overshoots. Qualitatively similar results were found for all four Cases, over a wide range of background gradients and point source parameters (results for Case 4 are plotted).
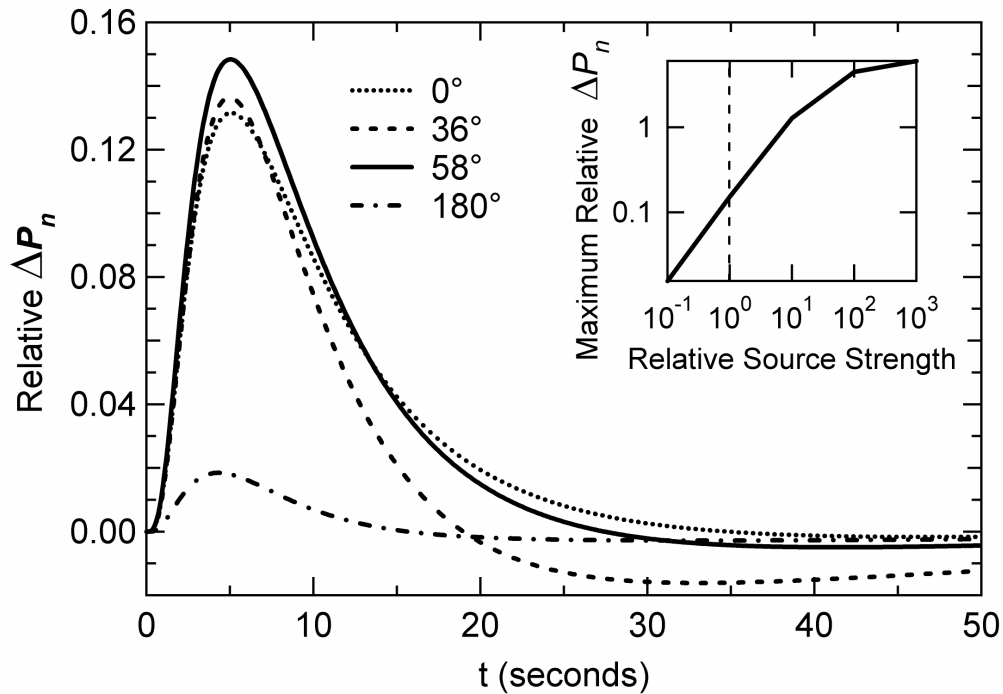
Figure 2.6 – Time Course of Point Source Response
Time progression of four membrane points for the conditions shown in Figure 2.5 B. Here, ΔP_n is normalized by the peak value of the 'Background P_n' curve in B. Inset: Logarithmic plot of maximum relative ΔP_n vs point source strength. The response levels off as the source strength increases. The dashed line indicates the strength used in all simulations. Qualitatively similar results were found for all four Cases, over a wide range of background gradients and point source parameters (results for Case 4 are plotted).

Figure 2.9, these features are accentuated when the response is integrated over time; quantifying responses in this way is likely to yield clearer results in experimental investigations of the biased-sensitivity in gradient-sensing response that we are suggesting.

The analysis here indicates that our model is most sensitive to *external* perturbations that are localized at an oblique angle, in the range typically between 40 and 80 degrees, relative to a pre-established polarization axis. The overshooting and undershooting of the response to the stimulus source angle that was observed in our

74

simulations reflects the fact that responses are most easily generated in this angular range even when the stimulus is localized outside of this range. These results are consistent with our finding in the previous subsection that the polarized state of the cell is most sensitive to *internal* perturbations that are peaked at approximately 60 degrees with respect to the polarization axis. Notably, both analyses demonstrate a similar biased sensitivity for *all* four representative Cases, suggesting that this bias should be a general feature of eukaryotic gradient sensing.

Why should a biased sensitivity be a general feature of gradient sensing in highly motile cells? For the parameters investigated in our model, the parameters that determine the baseline state in the unstimulated cell were always chosen to maximize the polarized response to a small static gradient. Thus, even a very small external gradient applied to a *resting cell* activates the positive feedback loops regulating responses at the front of the cell and suppresses them at the back. In a *polarized cell*, these feedbacks are *already* activated at the front of the cell and might be functioning near saturation, while at the back of the cell their activity is already suppressed and requires a larger stimulus for reactivation. At the sides of the cell, however, the state of the regulatory loops most resembles that in the resting, unstimulated cell, where responses are easily activated or suppressed in response to even very small perturbations. Thus, a biased sensitivity might be the result of cellular optimization for responses to shallow gradients.

(A)

(B)
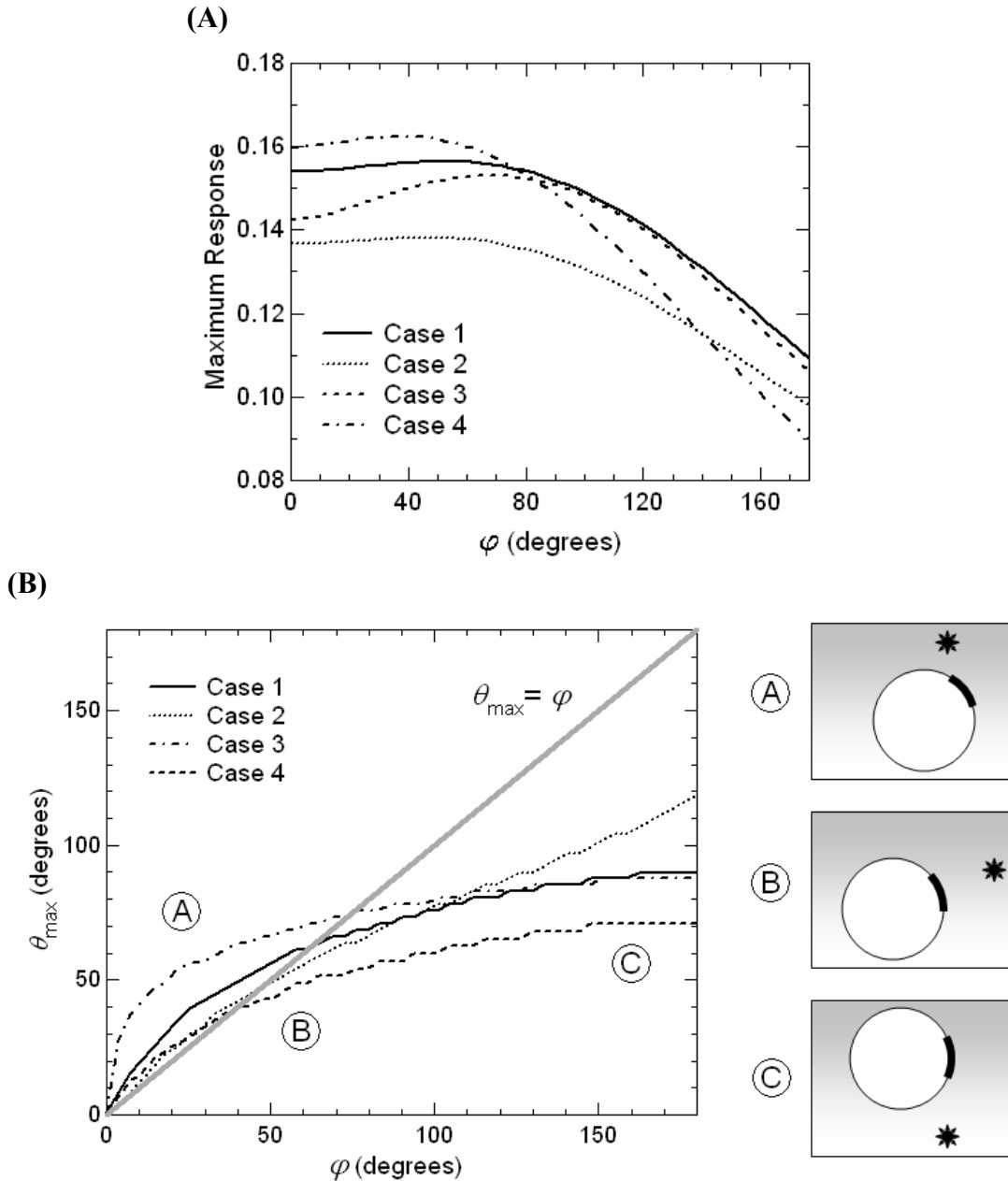
Figure 2.7 - Angular Bias in Responses to External Stimuli.

Responses of polarized cells to point sources were simulated, as in Figure 2.5, and the results plotted as a function of the source angle, φ. A) Peak value of the response ($\mathbf{\Delta P_n}$), normalized by the peak value of $\mathbf{P_n}$ in the steady-state background profile. The strongest responses occur for point sources at angles of approximately 40 – 80 degrees with respect to the background gradient. B) Direction of the maximal response, θ_{max} (see Figure 2.4). The cartoon illustrates the response overshooting that is observed for source angles less than approximately 40 degrees (A), and undershooting that is generally seen for large source angles (C). Similar results were found over a range of point-source parameters.

76

2.5. *Meandering of Chemotactic Cells*

Our analysis addresses only the gradient sensing component of chemotactic response, considering the localization of 3'PIs in response to chemotactic stimuli in a circular geometry. Moreover, it does not include coupling to cellular deformations and/or movements. Nevertheless, if a biased sensitivity is a general feature of gradient sensing in highly motile cells, this bias should affect the paths cells take when they are free to deform and move. Indeed, several key features of our results are consistent with observations of immune cells moving in responses to a chemotactic gradient.

Neutrophils and other amoeboid cells rarely move directly towards a chemotactic source. Rather, their trajectories frequently resemble biased random walks (see, e.g., [177-179]), although stochastic elements of their movement may be small compared with intrinsic, internally driven, oscillatory components of their motility [180]. This behavior was demonstrated quite dramatically, e.g., in a study of PMN leukocytes moving towards a stripe of aggregated protein (nominally γ-globulin) that acted as a source of chemotactic molecules [160]. In this instance, the trajectories of the cells appeared as essentially straight-line segments, linked by relatively abrupt changes in orientation, as illustrated in Figure 2.10 A [142, 160]. The cells seemed to zigzag as they moved up the gradient, having a tendency to overcompensate when they turned, and favoring turn angles of order 40 degrees with respect to the previous morphological polarization axis. In Figure 2.10 B we show a scatter diagram of the magnitudes of the turn angles demonstrated experimentally by the PMN cells as a function of their previous direction of movement with respect to

the gradient. We see that cells oriented at angles of less than approximately 40 degrees tend to overshoot the direction of the gradient when they turn, while those oriented at larger angles are likely to undershoot. These data are reminiscent of the angular features of the simulated 3'PI responses to point sources that were analyzed in Figure 2.7 B.

To match experiment and simulation results one needs to assume that in the experiment the morphological polarization of the cell is aligned with the direction of the internal gradients in our model variables and the external chemical signal acts as a perturbation. These assumptions are not unreasonable: morphological polarization likely feeds back on, and acts to stabilize, the distribution of signaling molecules at the front of a chemotaxing cell, possibly by affecting intracellular trafficking patterns that deliver important regulatory molecules [181-183]. Thus, if a cell is oriented at an angle with respect to the external gradient, the distribution of signaling molecules will be stabilized on that same axis. The extracellular applied gradient will then generate a perturbation in the profile of signaling molecules, whose shape will reflect the biased sensitivity that we have analyzed in our simulations. To connect bias in the sensitivity to bias in the direction of motion, we need to speculate. For example, if nucleation of new cellular protrusions depends on the change in signaling molecule concentration rather than its absolute value, then a protrusion directed with the same angular bias will be favored. Such a protrusion might then become stabilized via the suggested feedback between signaling molecule localization and cytoskeletal rearrangements. If the old cellular polarization axis eventually becomes destabilized, the new protrusion will define the polarization axis, and its direction will overshoot or

(A)
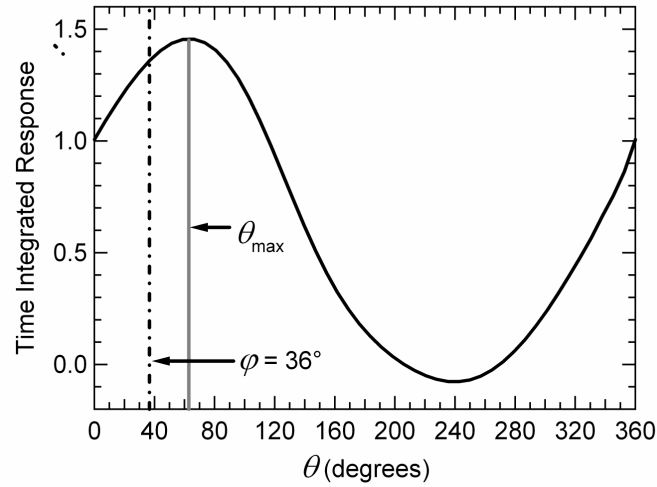
(B)
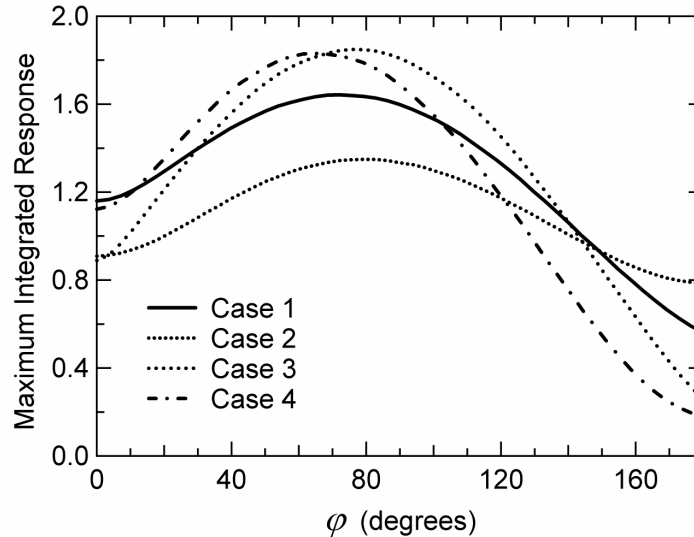
Figure 2.8 - Angular Bias in Time-Integrated Responses to External Stimuli.

Integrating the response of polarized cells to point sources over time accentuates biased sensitivity in responses. A) The profile of ΔP_n in response to a point-source stimulus released at $\varphi = 36°$, integrated over 50 seconds. θ_{max} is the direction of maximal time-integrated response in this case. B) Peak value of the time-integrated response for each point source angle, φ, analogous to Figure 2.7 A. Time integration makes the enhanced responses to off-axis stimuli most evident.
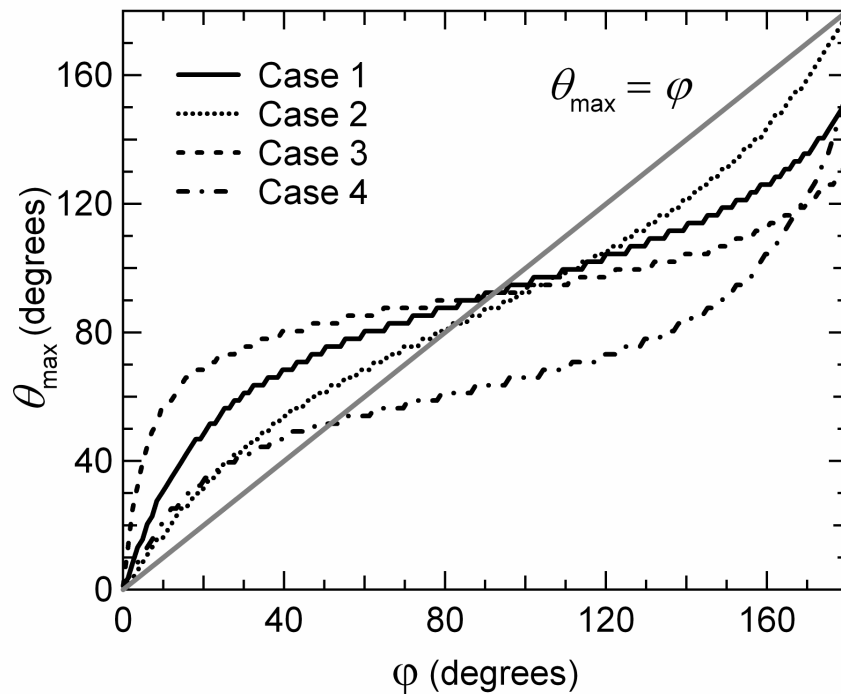
Figure 2.9 – Direction of Time-Integrated Maximal Response
Direction of the maximal response, θ_{max}. Notice that the response overshooting/undershooting sources at small/large is seen more clearly here that it was in Figure 2.7 B, where the response was not integrated. Similar results were found over a range of point-source parameters.

undershoot the direction of the gradient in the predicted manner. The cell will then continue to move along this axis until the external gradient succeeds in nucleating another new extension, whose direction again will reflect a biased sensitivity, overshooting or undershooting appropriately and repeating the process.

We should note that such zigzag motion has only been observed under specific sets of experimental conditions. The tie between our analysis and such movement is quite speculative, and other explanations are possible. For example, the geometry of the dendritic actin cytoskeleton at the leading edge of a cell [184, 185] might lead to preferred angles for the generation of a new lamellipodium. In addition, longer time-scale local inhibition of the cellular signaling apparatus might result in a

desensitization of the transduction apparatus at the leading edge of the cell after a characteristic time. Such change in sensitivity may generate a new leading edge in regions adjacent to the old one [178, 186].

2.6. _Summary and Discussion_

Eukaryotic gradient sensing is a complex cellular process. Although the general features of the signaling pathways that are involved are known and many of the relevant signaling molecules have been identified, there is still much left for discovery. Thus, a range of qualitative mechanisms that account for characteristic behaviors have been proposed. Novel approaches from multiple disciplines are needed to identify those features of gradient sensing that are general, and to design experiments that might distinguish between possible mechanisms.

Here we have analyzed a model that describes the dynamics of 3' phosphoinositide signaling in eukaryotic gradient sensing. This model is derived from proposed biochemical mechanisms and illustrates a range of possible signal amplification mechanisms. Linear-stability analysis and perturbation studies allow us to characterize responses in a very general way, and to identify patterns of stimulus to which a gradient-sensing cell is likely to be most sensitive. Studying model behaviors for several representative combinations of parameters allows us to start to investigate the generality of our results.

An analysis of the stability of uniform steady-state solutions indicates that the least stable internal perturbations are those for which the components linked to signal

A   **B**
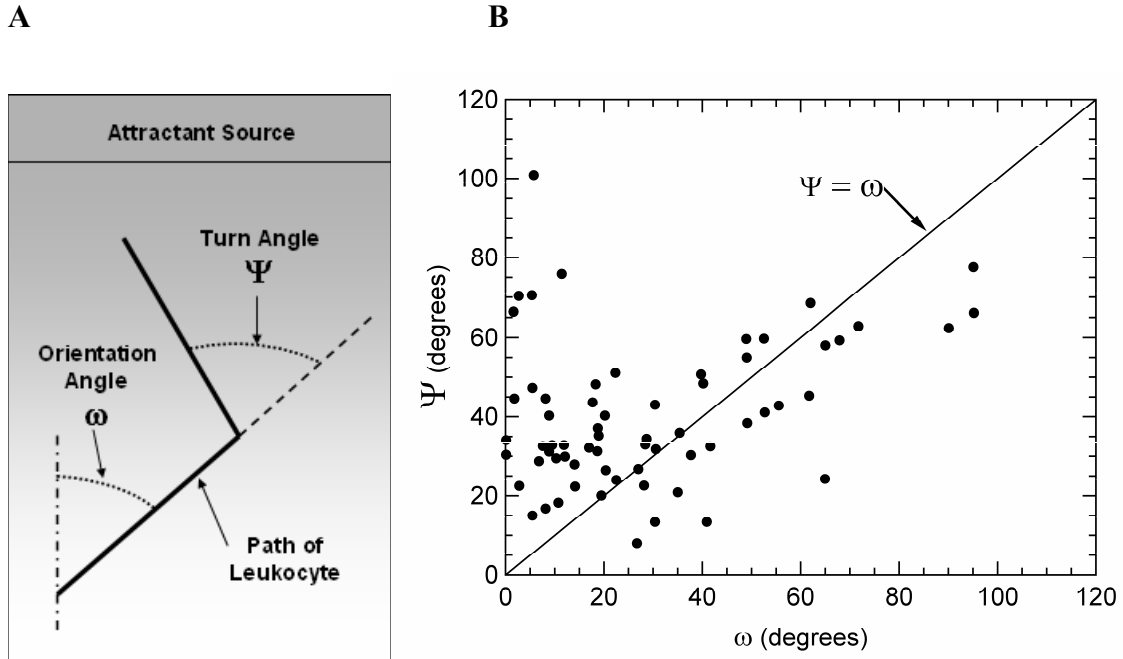
Figure 2.10 - PMN Leukocytes Moving in a Chemoattractant Gradient.

A) Idealized representation of cell tracks, showing the angle through which a cell turns after moving on a track directed at an oblique angle with respect the gradient prior to the turn. B) Absolute values of the turn angles, ψ, vs. directions of movement prior to a turn, ω (see [142]). The solid line indicates the turn angle that would have reoriented the cells exactly towards the source. Note that a curve of the average value of ψ if plotted as a function of ω, would have the qualitative features of the curves shown in Figure 2.7 B and Figure 2.8 C.

amplification reinforce each other. We found that we could characterize model

responses to such perturbations based on the signs and relative values of rate

constants for uniform and first-mode polarizing perturbations (which we labeled as j

$= 0$ and $j = 1$, respectively). We have shown qualitative possibilities that reflect

differences in the signal-amplification mechanisms that result from considering the

model in different parameter regimes, and we have discussed how the stability

properties of our model relate to more general Turing-type systems. Differences in

signal-amplification mechanisms lead to differences in responses to complex stimuli,

such as rotating gradients, and may affect patterns of cellular movement in natural settings in which stimuli vary in space and time (this topic is discussed further in our earlier work [69]). While it may be possible to characterize real cells by directly measuring growth or decay rates of internal perturbations, we have noted that it might be more productive to analyze cellular responses to external stimuli, which are more easily controlled.

Application of our stability analysis to polarized steady-state solutions indicates that these solutions are most sensitive to internal perturbations localized at an oblique angle of order 60 degrees with respect to the polarization axis. Here too the relationships among model constituents mirror those found when cells respond to external gradients. These results led us to investigate whether an angular bias exists in cellular responses to external stimuli as well. Indeed, a similar biased sensitivity was found in our simulations of polarized cell responses to 'spike' stimuli released at different angles with respect to a steady background gradient. [69]

Our analysis thus leads to the clear experimental prediction that the gradient-sensing response of a polarized cell should be most responsive to point source stimuli released at an angle of order 40 – 80 degrees with respect to a background polarizing gradient. For source angles below this range the direction of the response maximum overshoots the source angle, while for larger source angles it undershoots; in our simulations, we have found this effect to be accentuated if the response on the membrane is integrated over time. Further, we have argued that this biased sensitivity may be a general feature of gradient sensing in highly-motile cells, if developmental conditions exist that optimize their responses to small gradients.

Recently, Samadani et al. published experimental results using a configuration similar to one that might be used to investigate our model predictions, in which photo-uncaging is used to stimulate rounded *Dictyostelium* cells with localized point-source stimuli [187]. The results of this study indicate a different kind of biased sensitivity than the one that we have investigated. That is, the data suggest that rounded unstimulated cells retain an intrinsic polarization axis along which their angular response to weak stimuli is biased. The analysis suggests that this internal polarization can be included in an 'effective' stimulus that is a combination of the externally imposed chemotactic gradient and the intrinsic internally generated polarity of the cell. Because our perturbation analysis considers a steady-state polarization, without direct reference to whether that steady state is internally or externally generated, the possible presence of an internal polarization does not necessarily affect our predictions.

The analysis presented here only considered the gradient sensing component of chemotactic response under isolated conditions – it does not include any coupling to cellular deformation, cytoskeletal dynamics, and cell-cell or cell-self signaling. However, if a biased sensitivity is a general feature of the gradient-sensing apparatus, we expect it to be observable in the full chemotactic response, including motility, under more natural conditions. We have discussed how our results might account for the observed zigzag movements of immune cells moving up a chemotactic gradient, but have also noted several other factors that might account for such movements. These effects should also be observable in other cell types and under other experimental conditions. Further experiments and computational modeling will be

84

necessary to better understand how the various features of gradient sensing

mechanisms are expressed in the full chemotactic responses of motile cells.

2.7. *Appendix – Model Parameters*

Our scaled model parameters were generally set to reproduce characteristic

gradient sensing responses. Experimental observations that were considered are

discussed in [35]. Table 2-1 summarizes the meaning of each model parameter and

its value. Those parameters for which a range is indicated differ among the model

variants. Table 2-2 lists the combinations of parameters that were adjusted to define

the model variants. These combinations, together with the conditions $K_c = T_c = 0.5$ in

the unstimulated cell, are sufficient to specify the parameters in Table 2-1 in which a

range is given. Table 2-3 gives the uniform steady-state for an unstimulated cell,

which is always unique.

Table 2-1 – Model Parameters

Parameter	Equation	Interpretation	Value
χ_3	1	Rate constant for **Loop I** regulated P_3 production	120.0
κ_m		P_n which begins to saturate **Loop I** by depleting membrane molecules.	1.18 – 5.0
κ_c		P_n which begins to saturate **Loop I** by depleting cytosolic molecules.	1.25 – 6.7
ζ_{PITP}		Rate of g-P independent P_3 production/rate constant for gP dependent production.	0.025
κ_3		K_m at which PI3K binding to PITP·PI(4,5)P$_2$ becomes saturated.	0.05
$\zeta_{3/PITP}$		Rate of PITP independent P_3 production/rate constant for PITP dependent production.	0.025
ζ_3		Rate of unregulated P_3 production.	0.3
λ_3		Rate constant for P_3 removal by T_m.	15.0
$\zeta_{3/T}$		Rate of P_3 conversion to P_2/rate constant for T_m-mediated removal.	0.13
ζ_2	2	Rate of unregulated production of P_2.	0.02
λ_2		Rate constant for T_m-mediated removal of P_2.	8.0
$\zeta_{2/T}$		Rate of unregulated removal of P_2/rate constant for T_m-mediated removal.	0.05
χ_K	3	Rate constant for unregulated K_c translocation to the membrane.	0.0049 – 0.0076
R		Ligand-induced, receptor-mediated activation, which drives translocation of K_c.	external
λ_K		Rate constant for K_m phosphorylation and removal from the membrane.	0.73 – 4.2
κ_K		P_n at which 3'PI inhibition of K_m return to the cytosol (**Loop II**) becomes effective.	0.95 – 5.5
χ_T	4	Rate constant for T_c translocation to the membrane.	0.019
λ_T		Rate constant for T_m phosphorylation by K_m.	30.0
ζ_T		Rate of unregulated T_m return to cytosol/rate constant for T_m phosphorylation by K_m.	0.002
λ_{T*}	5	Rate constant for T_c* dephosphorylation in the cytosol.	0.15 – 0.21
λ_{K*}	6	Rate constant for K_c* dephosphorylation in the cytosol.	0.34 – 0.58
κ_{K*}		K_c* for which the reaction that dephosphorylates PI3K begins to saturate.	0.013

Table 2-2 – Parameters which Define the Model Variants

Parameter	Case 1	Case 2	Case 3	Case 4
κ_K	1.3	5.5	0.95	4.0
κ_c	6.7	1.38	5.0	1.25
γ_0	0.014	0.037	0.011	0.028

Table 2-3 – Steady-State, Uniform Profile for Each Variant at Zero Stimulus

Variable	Case 1	Case 2	Case 3	Case 4
P_3	0.38	1.16	0.19	0.85
P_2	0.60	2.82	0.25	1.78
P_n $(=P_3+P_2)$	0.98	4.0	0.44	2.63
K_m	0.025	0.064	0.016	0.046
T_m	0.1	0.054	0.15	0.071
$A_{cell}K_c*$	0.50	0.50	0.50	0.50
$A_{cell}T_c*$	0.50	0.50	0.50	0.50

3. Cell Speed, Persistence, and Information Transmission During Collective Migration

This chapter is adapted from McCann, Kriebel, Parent, and Losert [188].

3.1. *Summary*

Collective migration is a key feature of the social amoeba *Dictyostelium discoideum*, which uses secreted chemicals to communicate directional signals within a population. Understanding the collective dynamics of these cells requires knowledge of the rules of individual cell behavior as well as the interaction laws between cells. A key to such understanding is determining appropriate metrics with which to quantify experimentally observed behavior. In this chapter, we describe experimental work and subsequent analysis performed on two types of motile cells: one type is able to communicate via chemical signals, and the other cannot. We find that active chemical communication does not alter a cell's basic motion: cells move with the same speed and directional persistence with or without neighbor-to-neighbor communication. We find, however, that measurements of the chemotactic index (CI), a metric of directionality, indicate that population signaling directs cells to an aggregation center over large ranges independent of the original directional signal strength.

Collective motion in *Dictyostelium* results in structures called 'streams', which are head-to-tail chains of cells migrating in a common direction. To determine the motion of cells inside these dynamic structures, we experimentally label a fraction of cells with a fluorescent label and watch their motion inside and outside streams. We

find that being part of a stream does not alter the speed or persistence of a cell. These observations suggest a model of cell motion where the cell is intrinsically motile, with a predetermined speed and persistence, and outside factors guide cells but otherwise leave their basic motion unchanged. Signal relay via chemical signals therefore provides guidance cues necessary for gathering a large number of cells together.

3.2. *Introduction*

The ability of cells to migrate directionally in the presence of gradients of chemoattractants, referred to as chemotaxis, is a fundamental physiological response regulating a wide variety of biological processes [33]. In fast-moving cells such as neutrophils and *Dictyostelium discoideum*, chemotaxis is mediated by the binding of chemoattractants to specific G protein-coupled receptors (GPCRs), which transduce the chemotactic information to multiple effectors. This transduction eventually leads to the anterior enrichment of F-actin for pseudopod extension and the posterior/side accumulation of myosin II for back retraction [60, 64, 189]. Interestingly, many types of cells amplify chemotactic signals by synthesizing and secreting additional attractants upon stimulation, a process called signal relay [190, 191]. By relaying signals to neighboring cells, large numbers of cells can communicate and collectively migrate – a process that is emerging as a potentially important mode of transport in morphogenesis and cancer [15].

Dictyostelium provides an ideal model system for studying signal relay and collective cell migration [39, 191, 192]. When starved, up to 10^5 *Dictyostelium* cells migrate directionally toward one another to form tight aggregates that eventually

differentiate into a resistant structure made of a spore head atop a stalk of vacuolated cells, referred to as the fruiting body. During the aggregation process individual cells exquisitely sense and migrate toward cyclic adenosine monophosphate (cAMP; a chemoattractant). The binding of cAMP to its specific GPCR cAR1 (cAMP receptor 1) leads to the activation of a variety of intracellular signaling pathways that regulate chemotaxis, gene expression, and the synthesis and secretion of additional cAMP for signal relay [193]. Cyclic AMP emitted by individual cells drives groups of cells to self-aggregate if cells are sufficiently close to each other. Indeed, using mathematical modeling Cohen and Robertson provided evidence that there is a critical density for aggregation [194], and experimental work performed by several researchers established that a minimal cell-cell distance of 60-80 μm is required to sustain aggregation and fruiting body formation [195-197]. Interestingly, as cells sense and migrate towards cAMP signals they transition from single cell to group migration by aligning in a head-to-tail fashion to form characteristic lines of cells called 'streams' [198]. This transition from single to collective cell migration is dependent on the enzyme that generates cAMP, adenylyl cyclase A (ACA; an adenylyl cyclase expressed during aggregation), and in particular on its enrichment at the back of chemotaxing cells [105, 106]. Cells lacking ACA, or mutant cells that show a loss of ACA enrichment at their back, do not stream during chemotaxis. Kriebel et al. proposed that the cAMP signal is released from the back of cells, and as a result specifically leads cells to follow each other in a head-to-tail fashion [105]. In *Dictyostelium*, streaming therefore provides a direct measure of signal relay during chemotaxis.

Recent studies have revisited the question of how chemotactic signals are translated into migration. Steep chemotactic gradients can effectively trigger actin polymerization and dominant pseudopod formation in the direction of the chemical gradient [52, 143]. However, pseudopods also form when cells are exposed to a uniform concentration of chemoattractants during chemokinesis or under shallow chemotactic gradients [105, 199, 200]. Under these conditions, pseudopods emerge near each other in a coordinated fashion, allowing cells to maintain persistent motion in a given direction for several minutes [201-203]. Chemotactic signals of the strength used for cell-cell communication may simply override this natural ability of cells to maintain direction and generate new pseudopods, or take advantage of it and steer cells by biasing the location of naturally occurring pseudopods, as suggested by King and Insall [41].

While previous studies quantified the ability of single cells to migrate towards well-defined chemoattractant gradients [34, 149, 203], the role of signal relay on other chemotactic measurements has not been assessed. We therefore used cells lacking ACA (*aca*⁻), which are specifically defective in signal relay. We assessed their ability to migrate and compared with that of wild type (WT) cells. By tracing the motion of ensembles of thousands of *Dictyostelium* cells we were able to study how large populations of cells respond in groups during chemotaxis and to elucidate what aspects of cell migration are affected by signal relay and collective behavior. A second, equally important goal was to develop a simple metric for the assessment of the presence of signal relay that could be applied when no tell-tale signs of signal relay are present. Indeed, a variety of chemotaxing mammalian cells secrete

chemoattractants to amplify signals. While these cells may not show head-to-tail alignment, signal relay could still play a key role in the recruitment and migration of neighboring cells, and a direct measurement would help to decipher the role of signal relay in health and disease states.

3.3. _Results_

3.3.1. Short Cell-Cell Distances and Small Fluid Heights Are Necessary for Cells to Relay Signals During Chemotaxis

To provide baseline data for our studies, we first determined the cell-to-cell distance and fluid height for which _Dictyostelium_ cells relay signals and migrate collectively. For these experiments, WT cells were allowed to reach the chemotaxis-competent stage (see Appendix A.1.1), plated on glass chamber coverslips at cell-cell distances varying between 35 and 150 μm, and covered with 0.5 mm to 11 mm of buffer (corresponding to 5 to 600 μL of buffer in a square eight well plate; see Appendix A.1.4). Thousands of cells were observed by time-lapse microscopy, and their ability to collectively migrate was assessed based on visual inspection for the presence of streams one or a few cells wide (Figure 3.1 A). We found that the ability of cells to migrate spontaneously and form streams requires that cells are close to one another, up to a critical cell-cell distance of less than 100 μm (Figure 3.1 B) – as the cell plating density is lowered, the cell population transitions from forming streams to not forming streams. These findings are very similar to cell-cell distances found to be required for aggregation and fruiting body formation by other investigators [195-

197]. To determine if the absence of streams at large cell-cell distances is due to the inability of cells to sense their neighbors, or to their inability to release cAMP under diluted conditions, we used a micropipette to establish a stable chemoattractant gradient, essentially creating an artificial aggregation center to induce the release of cAMP by cells near the micropipette and trigger signal relay. The cell density was varied and the capacity of cells to stream was determined at a constant fluid height. As depicted in Figure 3.1 C, even when migrating toward an external point source of cAMP, cells stopped forming visible streams at the same cell-cell distance as observed during self-aggregation (the fluid height highlighted by the box in Figure 3.1 B is comparable to the fluid height used in Figure 3.1 C). This finding establishes that the inability of cells to stream is not due to a failure to initiate the production and emission of cAMP. Rather, as previously described by others [195-197], increasing the distance between cells hinders their capability to sense one another and thereby relay signals.

Figure 3.1 B shows that the ability of cells to stream also depends on the quantity of fluid present. We observed that as the amount of fluid is increased without changing the cell-cell distance, the cells lose their ability to stream. Remarkably, the addition of media isolated from high-density WT cells or cells lacking Conditioned Media Factor (CMF) [204] (instead of buffer) recovered streaming (data not shown), suggesting that a secreted factor other than CMF maybe involved. We envision that the dependence of streaming ability on fluid height, where the extra fluid is present several mm away from the cells, is not due to dilution of the cAMP signals

(A)

700 cells/mm² = 40 μm between cells

225 cells/mm² = 70 μm between cells

(B) **(C)**
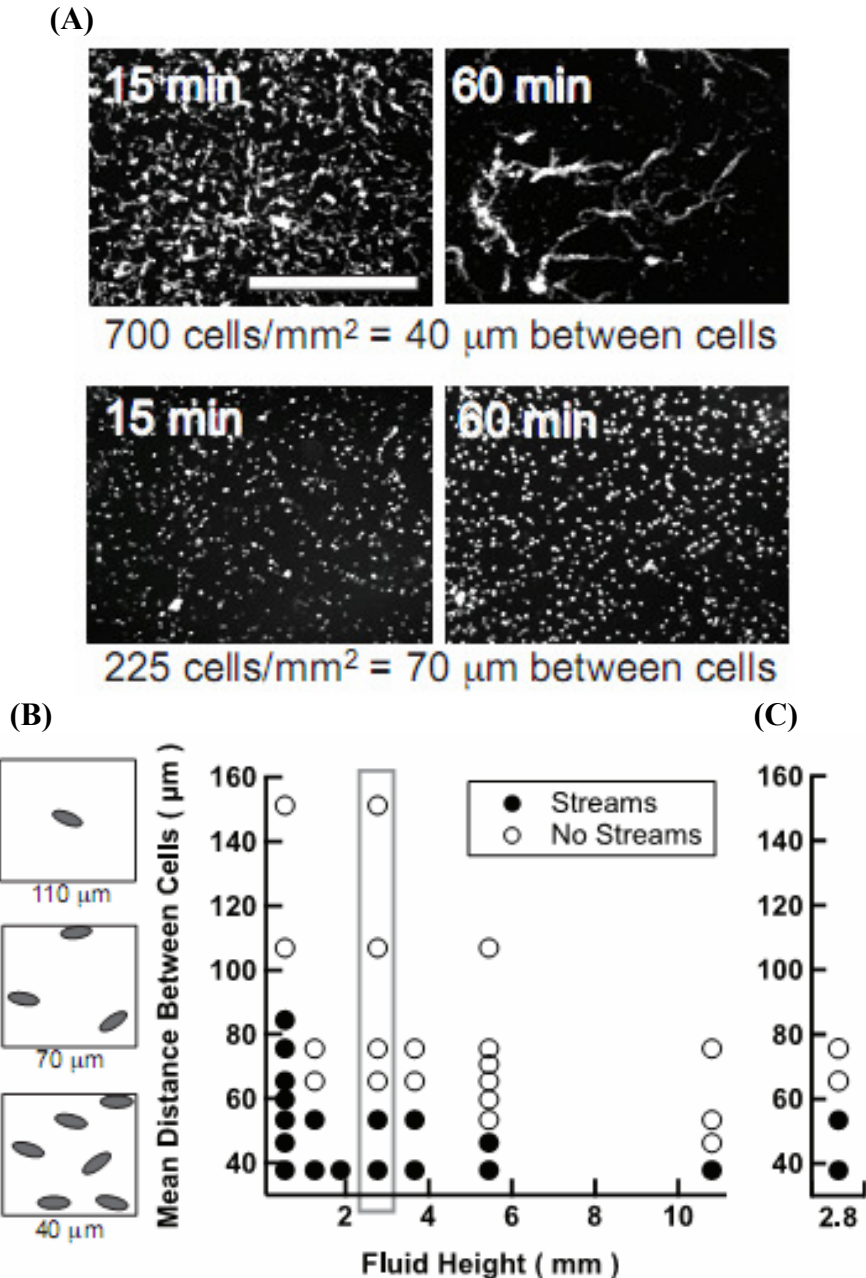
Figure 3.1 - Short Cell-Cell Distances and Small Fluid Heights are Necessary for Cells to Relay Signals During Chemotaxis
(A) Developed WT *Dictyostelium* cells plated on chambered glass slides at a mean center-to-center distance of ~40 μm (700 cells/mm²; top images) or a mean distance of ~70 μm between cell centers (225 cells/mm²; bottom images) under 3.9 mm of buffer. Images were taken with a 5x objective using phase-contrast microscopy 15 and 60 min after plating. Scale bar = 500 μm.
(B) Graph depicting the ability of cells to stream as a function of cell plating densities and fluid heights. The cartoons on left illustrate increasing distance between cells in the vertical direction. Each data point displays the majority result of at least 3 independent experiments. The grey box indicates region investigated in panel C below.
(C) Identical experiment as in B, but with the addition of a micropipette containing 10 μM cAMP.

for the following reasons: (1) cAMP diffuses too slowly (D_{cAMP} = 400 μm^2/sec [205]) to distribute over mm distances into the additional fluid volume on our experimental timescales. This consideration holds true for other signaling molecules larger than cAMP, such as Counting Factor (CF) [206]. (2) cAMP is not only emitted by cells, but is also degraded via a secreted phosphodiesterase [207], which decreases the distance over which cAMP molecules can travel. We conclude that particles smaller than cAMP, such as ions, are more likely the source of the fluid volume dependence, since ions diffuse an order of magnitude faster than cAMP [208]. The above argument assumes diffusive transport of cAMP, yet, strong enough fluid flows could cause dilution of signaling molecules of any size over mm distances on the experimental timescales. Thus, fluid flow was minimized during the experiments by imaging samples only at the start and end of each experiment (as flows can be triggered by heat and movements involved in imaging multiple wells). Furthermore, results were obtained similar findings when cells were plated on agar of varying thickness, in which the dense agar gel effectively prevents convective flows (Figure 3.2). However, cAMP dynamics are complex, so we cannot exclude the possibility that cAMP plays a role in regulating the dependence of streaming on fluid height. A cell-cell distance of ~40 μm was therefore used for all further experiments, as this cell-cell distance allowed signal relay and stream formation under all fluid heights tested.
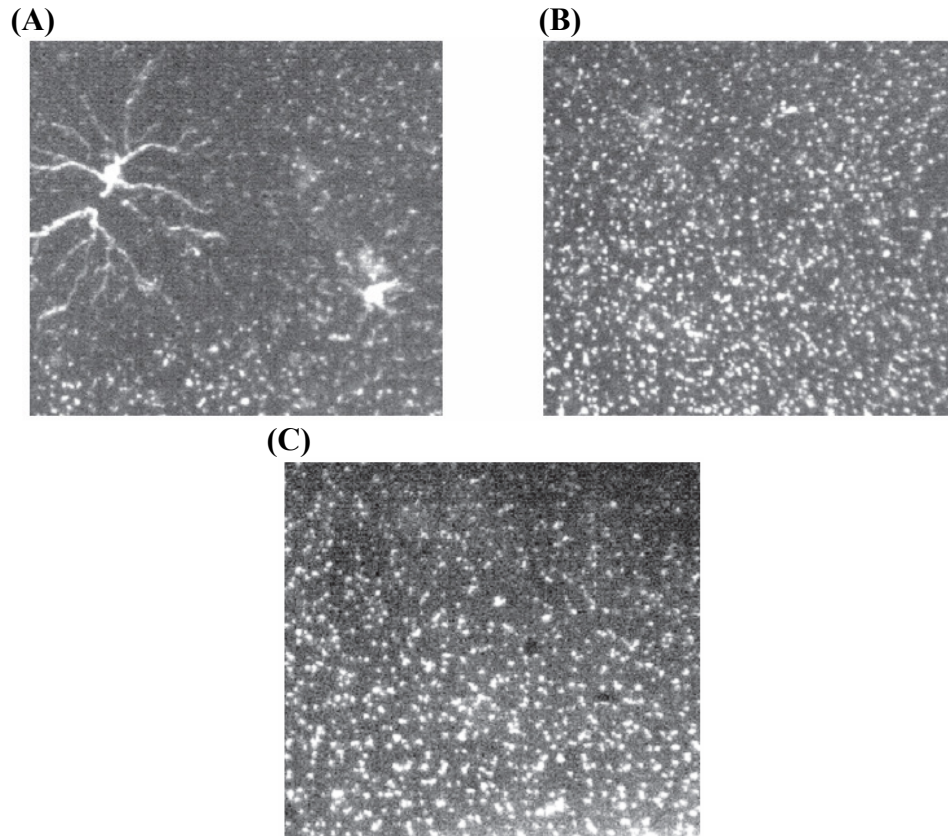
Figure 3.2 - Streaming Dependence on Fluid Height Not Due to Convective Flows.
(A) WT cells developed for 5 hrs were plated on a thin layer of agar (1 mm thick),
covered with either a thin (2 mm height) (A) or a thick (8 mm height) layer of buffer
(B), and assessed for stream formation after 2 hrs.
(C) WT cells developed for 5 hrs were plated on a thick layer of agar (8 mm), covered
with a thin layer of buffer (2 mm), and assessed for stream formation after 2 hrs.

3.3.2.   Signal Relay Does Not Regulate Individual Cell Speed and Short Time

Persistence

To determine if the presence of signal relay affects the ability of cells to migrate

individually (outside streams), we used *aca⁻* cells, which retain the ability to

chemotax but do not produce cAMP upon chemoattractant stimulation, and therefore

lack the ability to relay signals [105, 209]. Both WT and *aca⁻* cells were allowed to

96

reach the chemotaxis-competent stage and exposed to a micropipette filled with cAMP as a constant exogenous point source of chemoattractant for chemotaxis measurements. In addition, the behavior of both cells types was studied in the absence of exogenous point sources: *aca⁻* cells were exposed to a uniform increase of chemoattractant for chemokinesis measurements and WT cells were observed as they spontaneously migrate and aggregate. Indeed, chemokinesis is a key feature of chemotactic migration and is readily observed in *aca⁻* cells. WT cells, because of their endogenous ACA activity, do not require further chemoattractant stimulation and spontaneously exhibit random migration [105]. We experimentally acquired several time-lapse movies for each condition and automatically extracted the position and motion of all single cells, i.e. before they merged into streams, using custom image processing routines (see Appendix A.2.2). In order to reduce noise and eliminate the contribution of stationary cells, cell speeds were only included from cells that showed a net displacement of at least 20 μm over a 5 min time interval. Surprisingly, we found that the speeds of individual cells were comparable for *aca⁻* and WT cells ($p > 0.05$) under either chemokinesis, chemotaxis, or self-aggregation conditions (Figure 3.3 A depicts average data of hundreds of cells from one representative movie for each condition; Table 3-1 shows average speeds of thousands of cells from at least three independent movies once the speed plateau had been reached; see below). We also found that for cells chemotaxing to a point source of chemoattractant, the speed of moving cells does not depend on the cAMP concentration or gradient, as cell speed does not change as a function of the distance from the micropipette tip (Figure 3.3 B). Remarkably however, we observed for both WT and *aca⁻* cells in all conditions tested

that cell speeds almost double during the first 60 min of migration (Figure 3.3 A). It is

important to note that this gradual speedup is distinct from the routinely observed

rapid speedup measured just after cells are plated. To determine if the slow increase

in cell speed with time is due to development, we starved *aca⁻* cells for 5 and 6.5 hrs,

exposed them to a micropipette, and measured their velocity as a function of time

thereafter. We found that neither the absolute speed nor the speedup depend on these

developmental times, as all conditions displayed similar speeds and behavior (Figure

3.4). Similarly, cells plated in media isolated from starving cells showed the same

speedup (data not shown), suggesting that the lack of a secreted factor is not

responsible for the speed up. Together, these findings establish that signal relay does

not regulate individual cell speed during chemotaxis or chemokinesis and that the

speed of cells doubles during the first 1 hr of migration.

We next measured metrics that indicate how persistently a cell maintains its

motion in a given direction. This measure can be readily determined using mean

squared displacement (MSD) measurements, which indicate the total displacement

over which a cell migrates during a given time interval (see Appendix A.2.3). We

choose the MSD as it is a commonly-used measure of particle motion, and

importantly, its slope on a log-log plot provides intuitive information about track

persistence (see below). How fast the MSD increases with time can be seen from the

slope of the MSD in the double logarithmic plot of Figure 3.5 A. A slope of 2

indicates ballistic (straight-line) motion, whereas a slope of 1 indicates purely

diffusive motion [210]. We note, however, that the slope of the line is not constant

(A)

(B)
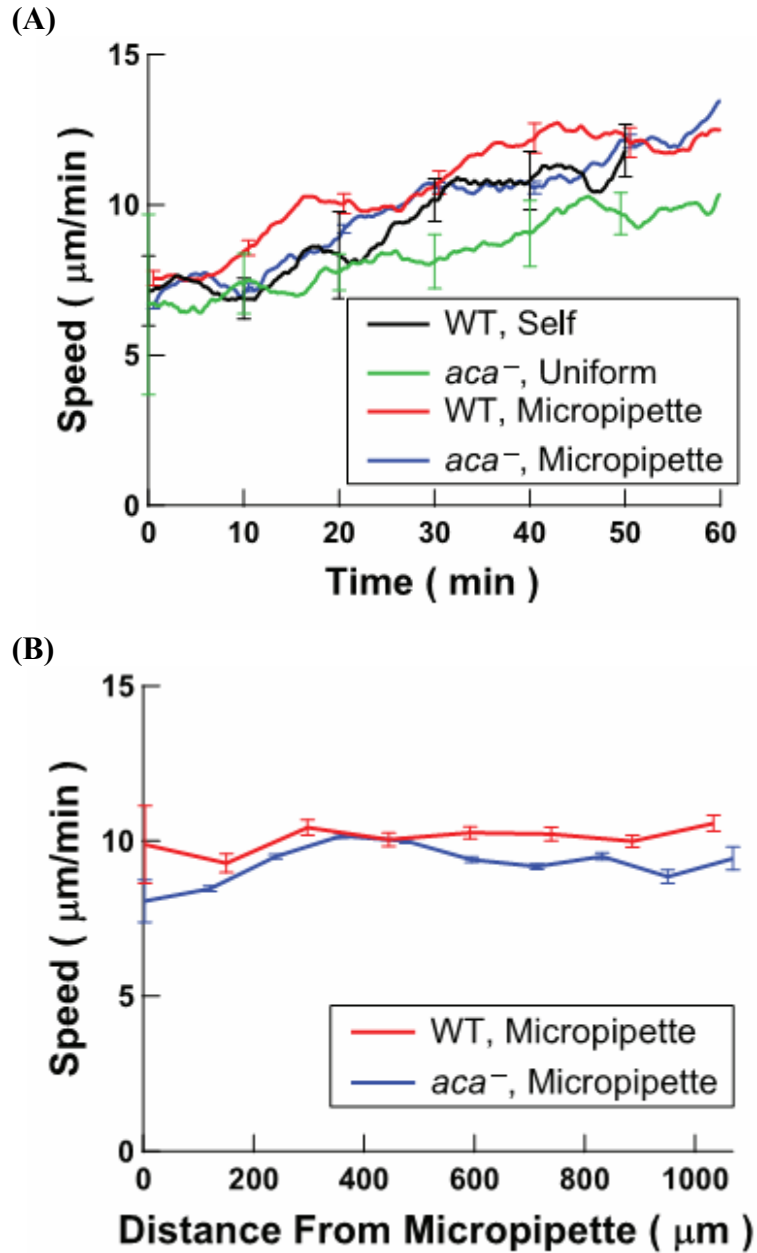
Figure 3.3 - Signal Relay Does Not Regulate Cell Speed
(A) Graph depicting average cell speed versus time for WT and *aca*⁻ cells. Cells were either subjected to a chemoattractant gradient provided by a 10 μM cAMP-containing micropipette (Micropipette) (WT and *aca*⁻), to a uniform 50 nM cAMP stimulus (Uniform) (*aca*⁻ cells only), or to endogenous stimulus (Self) (WT cells only). These data are representative of at least 3 experiments. Error bars indicate standard error of the mean. Table 3-1 shows average data from 3 experiments.
(B) Graph indicating average speed as a function of distance from a 10-μM cAMP-containing micropipette. These data are representative of at least 3 experiments. Error bars indicate standard error of the mean.
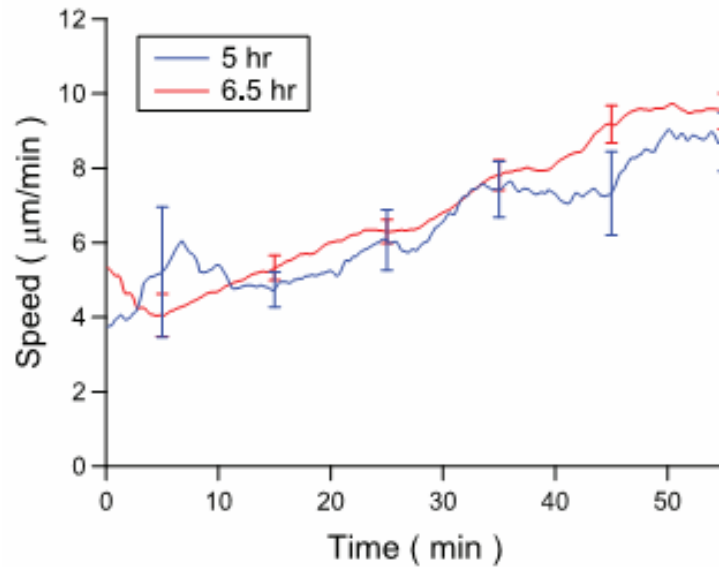
Figure 3.4 - Cells Speedup Independently of Development Time.
Graph depicting average cell speed versus time for *aca*⁻ cells developed for either 5
or 6.5 hrs. Cells were subjected to a chemoattractant gradient provided by a 10 μM
cAMP-containing micropipette. Graph is an average of three independent
experiments. Error bars indicate standard error.

for all time intervals; it can change as a function of time interval. For example, the

slope of *aca*⁻ motion is higher around ΔT =1 than at ΔT=10, indicating that over short

time intervals motion is more persistent than over longer time intervals. This measure

has been used by several research groups as a tool in differentiating among different

types of cell motion in *Dictyostelium* cells [210, 211]. Other measures of motion,

such as direction auto-correlation or turning rate, can be used as measures of

persistent motion [212], although these measures do not account for the net

displacement of a cell.

To find the persistence as a function of time interval, we calculate the local

slope, α, from Figure 3.5 A, and graphed it as a function of time interval, as

previously described [210, 213] (Figure 3.5 B). Since α is a derivative, it has higher

uncertainty than the MSD (hence the jagged lines vs Figure 3.5 A). Nevertheless α

provides more intuitive insight than the MSD: cells that move ballistically (straight)

have a slope α of 2 and cover twice the distance when given twice the time, while

randomly migrating cells have a slope of 1 and need four times longer (on average) to

cover twice the distance. We found that on timescales up to 3 min timescales ("Short"

on Figure 3.5 B), chemotaxing WT and *aca*⁻ cells have a similar α. This observation

is consistent with the similar slope of Figure 3.5 A, which highlights short times. The

slope of ~1.5 indicates that the overall direction of motion is persistent but that the

cell tracks are not completely straight (Figure 3.5 B). During chemokinesis of *aca*⁻

cells, the slope α decreases after 3 min, leveling off at α~1 at time intervals above 10

min ("Long" on Figure 3.5 B). This difference in α indicates that cells without a

directional signal maintain a preferred direction over several min, but over longer

times change direction randomly. In contrast, cells that migrate toward an aggregation

center – during spontaneous aggregation or migration to a micropipette – maintain a

slope of $\alpha \sim 1.6$ for all timescales, indicating persistence in their direction of motion.

Note that persistence data for WT cells have more variation than the data for *aca*⁻

cells (see Table 3-1). This variation is due to the fact that many WT cells quickly join

streams, and thus fewer cells can be tracked for the long time intervals needed for

MSD measurements.

Together, our findings establish that signal relay does not significantly regulate

individual cell speed during chemotaxis and chemokinesis. We also show that while

the presence of signal relay or exogenous directional cues does not impact the

(A)

(B)
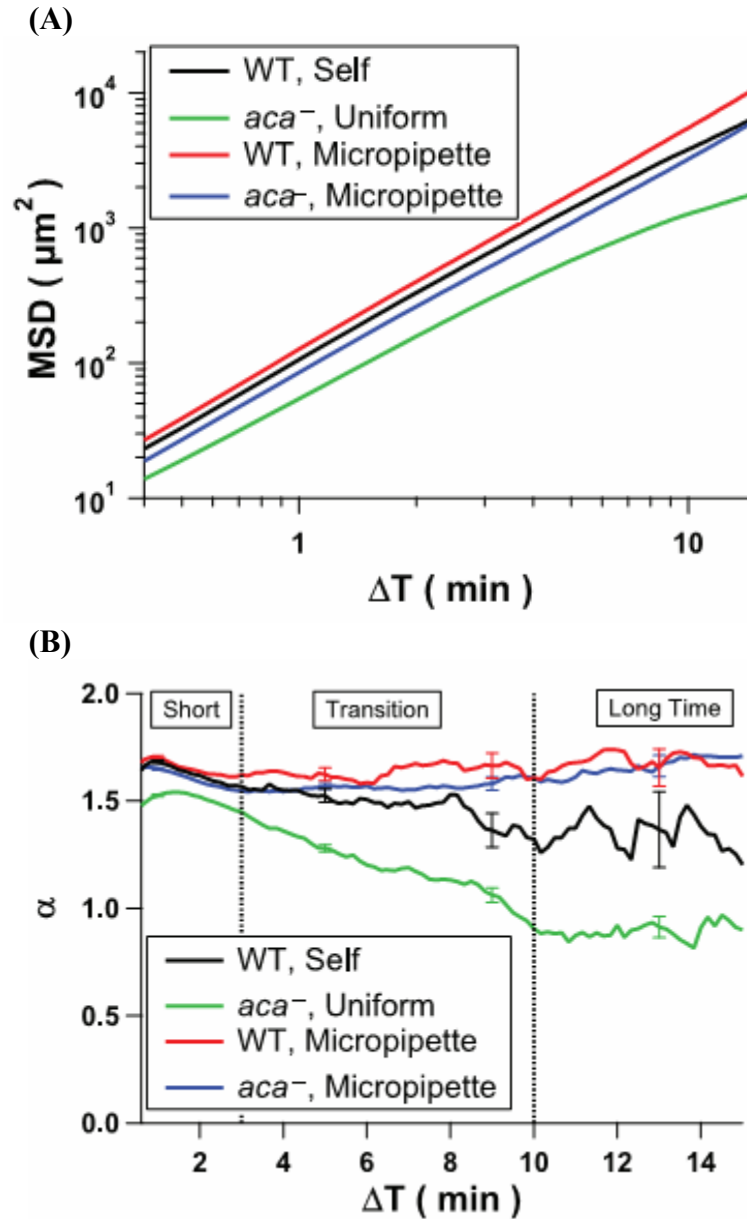
Figure 3.5 – Signal Relay Does Not Regulate Directional Persistence

(A) Graph depicting mean squared displacement (MSD) measurements as a function of time interval for the experiments presented in panel A. Error bars indicating standard error are smaller than the traces and are thus not shown.
(B) Graph depicting the slope α of the MSD graph in panel B as a function of time interval for the experiments presented in panel A. See text for details. Table 3-1 shows average data from 3 experiments. Error bars indicate standard error of the mean in the average α for every cell. "Short", "Transition", and "Long" designate the ΔT values where similar, changing, and different behaviors are observed between the different experimental conditions (see text).

persistence of individual cells on short timescales, directional cues, regardless of their nature, allow cells to maintain their preferred direction over long times.

3.3.3. Cell Speeds and Directional Persistence Are Similar Inside and Outside Streams

We next compared the migration behavior of individual cells (outside streams), to the migration ability of cells that are inside streams. Phase contrast images do not provide clear boundaries between cells in a stream, and thus did not allow us to elucidate the migration of cells within streams. To identify individual cells within a stream, we therefore analyzed WT cell populations in which 10% of the cells were treated with Celltracker, a cytosolic-staining dye. We captured both fluorescent images (to track the position and motion of the fluorescently labeled cells) and phase contrast images (to track the location and motion of all cells that are not part of a stream, and to elucidate the location of the streams) (Figure 3.6 A). Cell speeds were monitored for cells inside and outside streams in the presence or absence of a micropipette containing 10 μM cAMP, as described above. Figure 3.6 B and Table 3-1 show that the speed of cells as a function of time was comparable for all cell populations and under all conditions tested (Figure 3.6 B depicts average data of hundreds of cells from one representative movie; Table 3-1 shows average speeds of thousands of cells from at least three independent movies once the speed plateau had been reached). The data are here again dominated by a significant increase in cell speed over the first hr of migration. Furthermore, the local slope of the MSD (Figure 3.7) shows the same degree of directional persistence both inside and outside streams,

and this directional persistence is maintained both in spontaneous aggregation and directed migration of WT cells as noted above. We conclude that directional persistence and cell velocity are not altered when cells transition from single to group migration, even though cell-cell adhesions are present.

3.3.4. Signal Relay Increases Recruitment Range and Dramatically Affects Chemotactic Index

In our quest to determine the role of signal relay during chemotaxis, we next assessed the recruitment range of WT or *aca*⁻ cells to a point source of chemoattractant. We reasoned that the propagation of chemotactic signals from cell to cell would greatly extend the distance over which a chemotactic signal can travel. We also sought to determine to what degree signal relay between cells can transmit the original information, i.e. whether cells that directly sense an exogenous signal move toward it better than do cells 1 mm away that receive a signal that has been relayed by other cells. To address these questions, chemotactic-competent WT or *aca*⁻ cells were exposed to a micropipette containing various concentrations of cAMP, and their response range (in μm) from the tip of the micropipette was measured (see Appendix A.2.3). Figure 3.8 A shows representative images of WT and *aca*⁻ cells 60 min after the activation of the micropipette containing 100 nM or 10 μM cAMP and Figure 3.8 B shows the quantification of the response range to various cAMP concentrations. As expected, *aca*⁻ cells showed a clear dependence of response range on the strength of the cAMP source. With every ten-fold increase in cAMP concentration, we measured a ~200 μm (~10 cell length) increase in the response range. On the other hand, the

response range of WT cells involved the entire visible cell population up to a distance of 1500 μm from the micropipette tip, independent of the cAMP concentration in the micropipette.

The chemotaxis index (CI) of cells provides an instantaneous measure of how well cell motion is directed toward an exogenous source, and is thus a measure of how well the cells sense the "information" provided by the micropipette. The CI is defined as $\mathrm{CI}(t,i) = [\vec{u}_i(t) \circ \hat{r}_i(t)]/|\vec{u}_i(t)| = \cos[\theta_i(t)]$, where $\hat{r}_i(t)$ is the unit direction vector from cell i to the pipette at time t and $\theta_i(t)$ is the angle between cell i's motion vector at time t and the vector pointing to the pipette (see Appendix A.2.3). Therefore, a CI of 1 indicates that a cell is moving directly toward the source and thus fully responds to the information, whereas a CI of 0 indicates motion perpendicular to the direction of the source and thus a lack of information about the micropipette position. This analysis was performed on populations of WT or aca^- cells responding to a micropipette containing 0.1, 1, or 10 μM cAMP. As depicted in Figure 3.9 A, cells lacking ACA show a high CI close to the source followed by a decrease in CI with increasing distance from the micropipette, indicating that sensing of the information provided by the micropipette decreases with distance from the source. Similarly, we find that the CI decreases with decreasing exogenous signal strength for these signal relay-deficient cells. Conversely, as indicated in Figure 3.9 B, WT cells display a constant low CI that is independent of the distance to the micropipette or the amount of chemoattractant signal emitted from the micropipette.

Table 3-1 – Quantitative Migration Data of WT and *aca⁻* Cells

Cell Type	n^a	Speed $(\mu m/min)^b$	α^c
WT, self-streaming	30±14	10.8±2.2	1.3±0.5
WT, micropipette[d]	78±87	11.7±1.4	1.5±0.1
aca⁻, chemokinesis[e]	50±23	10.7±1.0	1.1±0.2
aca⁻, micropipette[d]	42±44	9.4±0.8	1.5±0.1
Fluorescent WT, self-streaming, outside streams	8±3	11.1±2.9	1.5±0.1
Fluorescent WT, self-streaming, inside streams	31±1	8.9±1.8	1.6±0.1
Fluorescent WT, micropipette, outside streams[d]	13±6	10.0±2.5	1.4±0.1
Fluorescent WT, micropipette, inside streams[d]	22±19	9.6±1.1	1.5±0.1

[a]Average number ± s.d. of individual cells tracked at each time point for each experiment. Taken from at least three independent experiments.
[b]Speeds (mean ± s.d.) are not statistically different for all conditions tested ($P>0.05$).
[c]Note that all α (mean ± s.d.) are ~1.6 on short (< 1 minute) time intervals.
[d]The micropipette contained 10 μM cAMP.
[e]ith the addition of a uniform concentration 50 nM cAMP.

To verify that the CI provides a reliable metric of signal relay rather than just emphasizing the difference between WT and *aca⁻* cells, we went back to our initial results showing that a minimum cell-cell distance is required for cells to relay signals effectively during migration. In Figure 3.1 B we showed that increasing the cell-cell distance to 70 μm prevents streaming even in the presence of an exogenous point source of cAMP from a micropipette. We now measured the CI for WT cells plated at two cell-cell distances, 40 μm and 70 μm, and subjected to a micropipette containing 10 μM cAMP (Figure 3.10). We find that in the presence of streaming (40 μm cell-cell plating distance) the CI is independent of the distance to the micropipette. In contrast, in the absence of streaming (70 μm cell-cell distance) the CI declines with increasing distance from the micropipette tip. Furthermore, we also observe that non-

streaming cells show a higher CI near the micropipette, much like we measured for

aca⁻ cells. Together, our findings show that the CI provides meaningful insight into

signal relay. In our system, signal relay preserves the information on the location of

the micropipette even at distances where none of the exogenous signal is left, and

signals are solely relayed from cell to cell along tens of cells.

3.4. *Discussion*

The ability of cells to propagate chemotactic signals is essential in a wide

variety of biological processes and is often associated with the transition from single

to collective cell migration. Our study provides novel insight into the behavior of

cells exposed to secreted signals during chemotaxis and collective cell migration. We

first confirmed that short cell-cell distances are necessary for cells to aggregate and

showed that a maximum cell-cell distance of 50-100 μm is necessary for cells to form

streams. We reason that for such close neighbors, the specific location on a cell from

which the chemotactic signal is emitted during signal relay should matter. Indeed, in

Dictyostelium the cellular distribution of signal relay components is spatially

restricted: ACA is enriched at the back of chemotaxing cells, presumably giving rise

to localized cAMP secretion and head-to-tail cell alignment [105]. Our current

findings that signal relay occurs over very short distances indicate that such local

secretion could impact signal relay. For 20 μm long polarized cells at center-to-

center distances of 100 μm, if signal relay were *not* from tail to head, an emitted

signal would need to cover a 25% longer distance and take roughly 50% longer

(A)

(B)
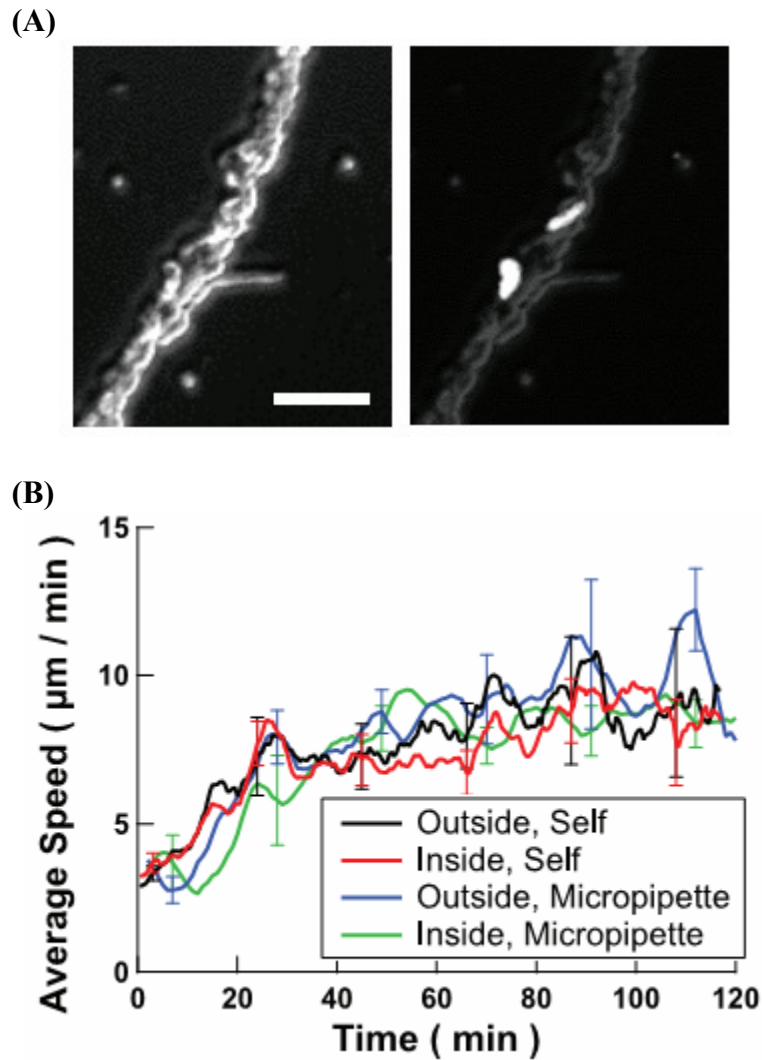
Figure 3.6 - Cell Speeds Are Similar Inside and Outside Streams
(A) (Left) Phase-contrast image of a stream that is several cells wide. (Right) Fluorescent image of the same field overlaid on a darkened phase contrast image. Two fluorescently-dyed cells can be distinguished, and their behavior can be analyzed. Scale bar = 40 μm.
(B) Graph depicting average cell speed versus time for WT cells inside or outside streams. Cells were either subjected to a chemoattractant gradient provided by a 10 μM cAMP-containing micropipette or to an endogenous chemoattractant stimulus. These data are representative of at least 3 experiments. Error bars indicate standard error of the mean. Table 3-1 shows average data from 3 experiments.

to cover that distance. Furthermore, additional factors are required to generate directional information via signal relay - if all cells continuously emit cAMP, even a localized release would not generate population wide directional information in groups of randomly oriented cells. Indeed, in-depth studies of self-aggregation have shown that waves of cAMP are crucial and require three factors: the release of cAMP in bursts, the degradation of cAMP by external phosphodiesterases, and the brief adaptation of the signal transduction cascade following cAMP sensing and relay [214, 215]. Although no clear cAMP waves are visible during chemotaxis to a micropipette, the similarity in migration metrics between self-aggregation and chemotaxis to a micropipette suggests that these factors also contribute to the relay of information to an exogenous signal.

We measured the effect of signal relay on a variety of cell migration parameters and found that the speeds of individual moving cells as well as their directional persistence are not affected by signal relay. We also discovered that individual cell speed, in all conditions tested, significantly increased during the first hour after the start of migration, leveling out in the second hour to about twice its initial value. This finding is consistent with other qualitative observations [216] as well as with quantitative analyses of cell speeds during self-aggregation [217]. We found that the gradual increase in speed was not due to continued development during the two-hour long experiments and appeared to be unrelated to better coordination of where pseudopods form, as directional persistence did not change significantly with

(A)

(B)
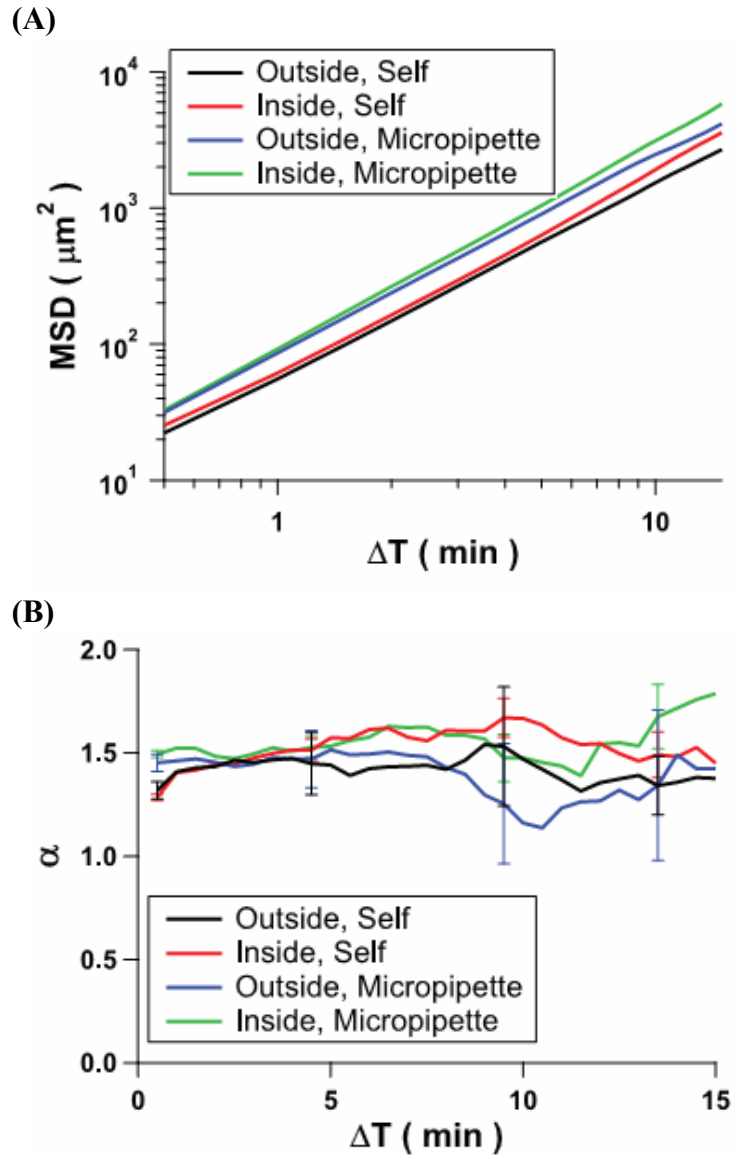
Figure 3.7 – Directional Persistence is Similar Inside and Outside Streams
(A) Graph depicting MSD measurements as a function of time interval for the experiments presented in Figure 3.6. The standard error is smaller than the traces, and thus error bars are not shown.
(B) Graph depicting the slope α of the MSD graph in panel C as a function of time interval for the experiments presented in panel B. See text for details. Table 3-1 shows average data from 3 experiments. Error bars indicate standard error of the mean in the average α for every cell.

time. Speedup also appeared unrelated to more effective sensing, as the CI did not change with time. Although the mechanism underlying the speedup of cells with time remains to be determined, it likely involves an increase in the size or growth rate of pseudopods.

Interestingly, under our experimental conditions, cell speed did not depend on the distance from the micropipette. Studies using microfluidic devices have shown that *Dictyostelium* sharply transitions from a low basal speed in weak gradients to a higher speed in strong gradients [34]. This apparent discrepancy can be explained by the fact that the microfluidic and micropipette devices generate different cAMP concentration gradients. Indeed, based on experiments in which the micropipette was filled with rhodamine (a fluorescent dye; data not shown), we determined that the cAMP concentration gradients used in our studies were in the high range of cAMP gradients used by Song and colleagues [34], in whose studies the cells moved at constant maximum speed. Our observation that the CI is constant for WT cells indicates that signal relay dominates over the exogenous signal from the micropipette, suggesting that our exogenous gradients are comparable to the concentration gradients generated by cells at the cell-cell distances needed for signal relay and spontaneous aggregation.

We determined how well a cell maintains its direction of migration from how fast the mean squared displacement (MSD) changes as a function of a time interval ΔT. The slope of this graph, α, provides important insights, since it highlights the dominant motility behavior on different timescales. We found that both individual

(A)

(B)
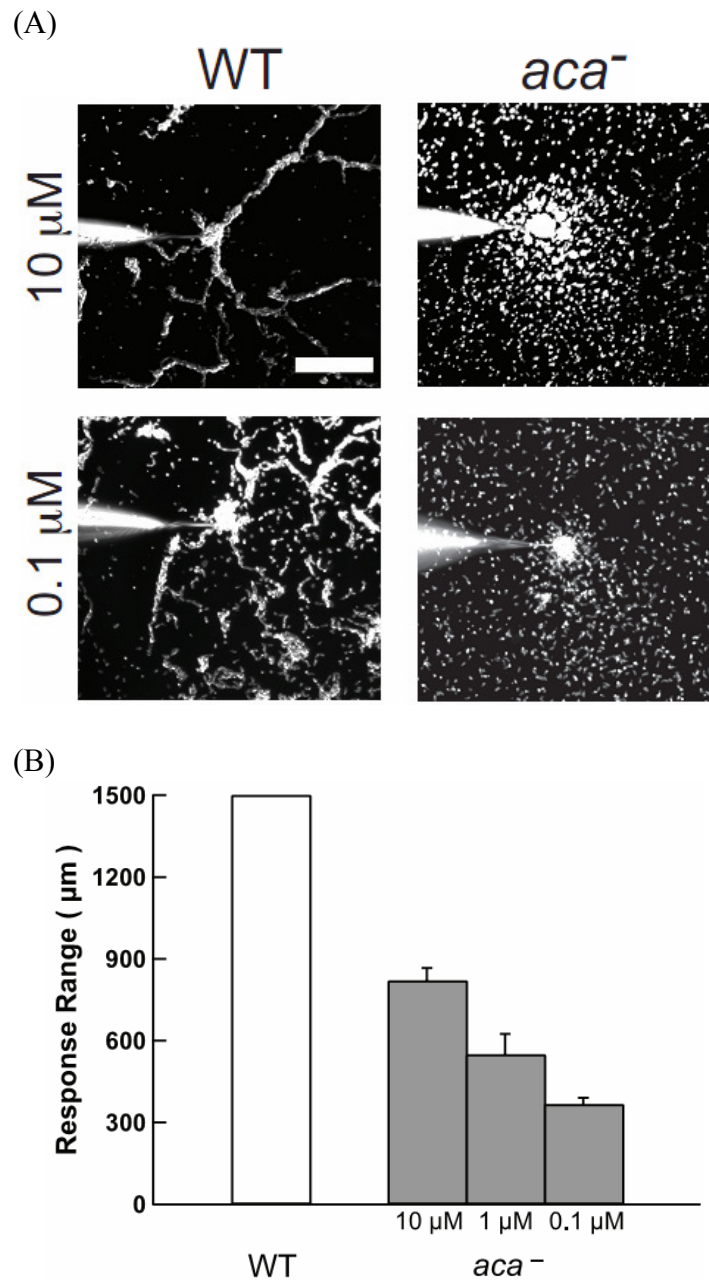
Figure 3.8 - Signal relay Increases Recruitment Range
(A) Phase-contrast images of WT or *aca⁻* cells 60 min after the cells started to migrate to a micropipette containing 10 μM (top) or 0.1 μM (bottom) cAMP. Scale bar = 200 μm.
(B) Quantification of the response range of WT and *aca⁻* cells over 90 min. The numbers on the x-axis represent the concentration of cAMP in the micropipette. The method used for determining the response range is presented in Figure 3.9. WT cells responded equally to all concentrations tested. Error bars indicate standard error of the mean and were derived from 3 independent experiments.

WT and *aca*⁻ cells maintain a preferred direction of motion over ~3 min intervals under both chemokinetic and chemotactic conditions, consistent with other reports on individual cell migration [149, 178, 201, 210, 218-220]. This result indicates that the tendency of pseudopods to develop close to one another, as suggested by Bosgraaf and van Haastert [203], may dominate the dynamics on short times even during chemotaxis and signal relay. The timescale over which α decreases during chemokinesis (between 3-10 min in Figure 3.5 B) can be interpreted as the time over which the preferred location of pseudopods changes and cells turn. When directional chemotactic cues are present, either from exogenous sources or due to signal relay, cells maintain a preferred direction over long times, and the slope α thus remains near 1.6. This result indicates that chemotactic signals bias the location of naturally occurring pseudopods, as suggested by King and Insall, thus allowing cells to maintain a preferred direction over long times [41].

Remarkably, we found that both cell speed and persistence in the direction of motion are identical in individual cells and in cells inside streams that are one or a few cells wide. This finding was surprising - we expected cells moving in groups to have distinct behaviors, as observed in simulations that explore the role of cell adhesions during early and late stages of morphogenesis [96, 101]. Indeed, cell-cell adhesion sites may induce both biochemical and mechanical perturbations [191, 221]. Our findings therefore establish that the intrinsic motility machinery, as well as the ability to migrate directionally, are innate properties of single cells that are remarkably maintained regardless of additional external signals or cell-cell interactions.
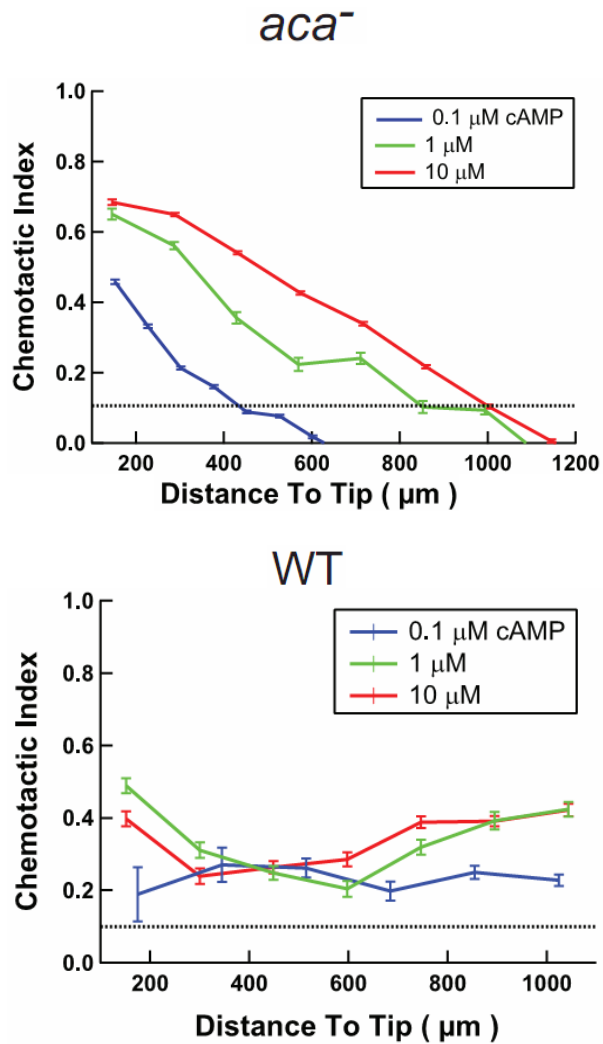
Figure 3.9 – Signal Relay Regulates the Chemotactic Index
(A) Graph depicting the time-averaged CI as a function of the distance from the tip of
the micropipette for *aca⁻* cells migrating to a micropipette containing various
concentrations of cAMP. Error bars indicate standard error of the mean.
(B) Graph depicting the time-averaged CI as a function of the distance from the tip of
the micropipette for WT cells migrating to a micropipette containing various
concentrations of cAMP. Error bars indicate standard error of the mean. Each line
indicates a single representative experiment of at least 3 experiments. The dotted line
indicates the threshold CI (0.1) used to assess response range in Figure 3.8

        In [74] work is presented that suggests migrating *Dictyostelium* cells move

themselves via formation and propagation of 'curvature waves' (see Figure 3.11).

These curvature waves are small (~3 μm) membrane bumps that originate near the

114
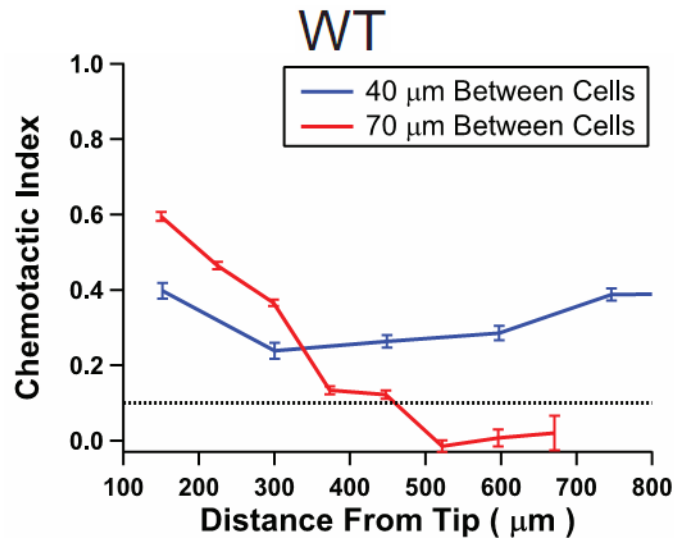
Figure 3.10 – Chemotactic Index as a Metric for Assessing Signal Relay
Graph depicting the time-averaged CI as a function of the distance from the tip of the micropipette for WT cells plated at various densities and migrating to a micropipette containing 10 μM cAMP. The dotted line indicates the threshold CI (0.1) used to assess response range in Figure 3.8. Error bars indicate standard error of the mean. Each line indicates a single representative experiment of at least 3 experiments.

leading edge of the cell and translocate along one side or the other. When these waves come into contact with the surface, they still translocate with respect to the cell, but they no longer move with respect to the surface. The authors postulate that these waves couple to the surface and are part of the protrusion machinery that drives the cells forward. Furthermore, the generation of these waves often follows a left-right pattern, leading to zig-zag motion of the cell. Although the components of these waves are unknown, one candidate is actin, which has been shown to organize into separate filamentous and non-filamentous pools inside the cell. Supporting this idea, studies of cell spreading on a surface have shown that some membrane protrusion is due to waves of polymerized actin reaching and then extending the cell membrane [76].

115
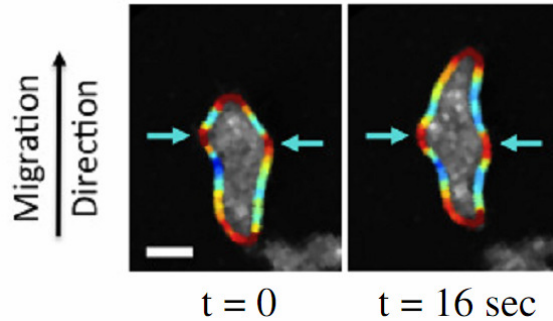
Figure 3.11 – Boundary Curvature of a Migrating *Dictyostelium* Cell
Image adapted from [74]. The calculated cell boundary (in color) is overlaid on the original fluorescence images (in gray). Curvature is designated by color; high positive curvature (outward bumps) is shown in red, flat curvature is green, and high negative curvature (inward bumps) are in blue. (Left) Two curvature peaks, indicated by teal arrows, propagate down the sides of the cell (right) but remain at the same substrate location. (Scale bar, 5 μm).

We found that on short time scales (< 3 min) cells moved essentially persistently in a given direction, but an overall directional cue was required to maintain persistence for longer time scales. This type of persistence is compatible with the 'zig-zag' protrusive activity shown in [74]. Successive protrusions of randomly migrating cells are correlated in space, leading to persistent motion on timescales on the order of a few protrusions (~30 seconds/protrusion). However, over longer times, protrusions are no longer correlated in random migration, leading to a drop in directional persistence. In addition, we found that the speed of cells did not depend on the strength of the external gradient, which is again compatible with the constant protrusive activity demonstrated in [74]. Our findings are therefore suggestive of a model of chemotaxis in which the chemical signal biases the direction of motion but does not drive motion; in other words, the chemical signal steers but does not propel.

These data provide suggestions for improving upon existing models of

Dictyostelium motion. Models in which the gradient-sensing ability feeds directly

into pseudopod polymerization are clearly incorrect, as cell speed is independent of

chemical gradient. Instead, models featuring an intrinsic motile activity that is biased

by a chemical gradient match well with our data, such as that found by Driscoll et al.

[74] or proposed by Insall's 'pseudopod-centric' view of migration [77].

Our findings show that signal relay dramatically affects the recruitment range of

cells to an exogenous source of chemoattractant. In the absence of signal relay, the

range over which cells migrate to the chemotactic source exhibits a strong

dependence on the strength of the chemotactic signal. In contrast, in the presence of

signal relay, the response range is independent of the cAMP signal strength. CI

measurements as a function of distance from the chemoattractant source provide

interesting insight into this phenomenon. As expected, when signal relay is absent (in

aca⁻ cells or in diluted WT cells), we find that the CI decreases with distance from an

exogenous source, and increases with increasing source strength. When signal relay is

present, the CI becomes independent of both the distance from the exogenous source

and of the source strength. However, under these conditions, the CI is significantly

smaller than without signal relay close to the chemotactic source. Thus our findings

show that signal relay can transmit directional information over long distances

without significant information loss. Interestingly, van Haastert and Postma recently

reported that WT cells show a decrease in CI with increasing distance from the

chemotactic source or with decreasing source strength [110]. Based on our extensive

analyses, we envision that their experiments were likely performed under dilute conditions in which the chemotactic signal is not relayed.

Taken together, our data shows that signal relay enhances recruitment range without affecting cell speed or directionality. While streaming represents a clear indicator of signal relay in *Dictyostelium*, signal relay does not necessarily give rise to streams. We propose that the independence of the CI on the distance from an exogenous chemoattractant source represents a robust metric for determining whether signal relay takes place in various chemotactic systems. Signal relay during chemotaxis needs to encode directional information, which is achieved through restricted cellular distribution, signal degradation, and refractory periods. We propose that some, if not all, of these features are needed to generate an effective relay of information between neighboring cells. We conclude that a combination of speed, persistence, and CI measurements represents a powerful way to dissect signal relay in motile cells.

4. Cell-Surface Adhesion: Effects on Individual and Collective Motion

This chapter is adapted from McCann, Rericha, Losert, and Parent [222]. The F-actin-staining data presented Section 4.3.5 and Figure 4.10 were taken by E. Rericha. These data are included to highlight that cells adapt to cell-surface adhesion by regulating F-actin polymerization.

4.1. *Summary*

Understanding the dynamics of cell motility requires knowledge of how cells attach to a surface, generate protrusive forces at their front, and contract their body at the back. In this process, the amount of cell-surface adhesion is critical, as cells need sufficient traction in order to move forward, yet they also require adhesion to be low enough to allow de-adhesion and retraction of their backs [223, 224]. In this chapter we experimentally investigate how motility depends on cell-surface adhesion. We produce four different surfaces that are commonly used in the biology literature and measure the cell-surface adhesion energy of *Dictyostelium* cells on each. Next, we acquire time-lapse images of cells moving on each surface and find that motion is quantitatively the same on all surfaces despite the different surface properties. Finally, we probe the mechanical regulation of adhesion by placing cells lacking a key contractile protein on each surface, and we find that protrusion is required to compensate for small cell-surface adhesiveness, and contractility is required to compensate for large cell-surface adhesiveness. In individual cells, therefore, we find

that the mechanisms of motility are robust for cells moving on surfaces where the cell-surface adhesion energy varies by as much as nine orders of magnitude. This finding reinforces the conclusion of Chapter 3, in which cells have intrinsic motility that operates largely unaffected by environmental conditions.

The rules governing individual motility are therefore largely robust to the cell environment; however, we experimentally investigate whether the interaction laws of collective dynamics of cell populations are surface-adhesion dependent. We place populations of thousands of cells upon each of the four surfaces and find that there is a striking difference between the dynamic patterns of aggregations: cells tend to form more spatially extended streams on less adhesive surfaces. To understand this phenomenon, we allow individual cells to migrate on a surface containing an interface between surfaces of two different adhesivities. When cells encounter an interface, they tend to move toward the less adhesive surface. This 'preference' explains the collective dynamics of cells: less adhesive surfaces lead to more surface contact than neighbor contact, and hence larger streams, while more adhesive surfaces lead to more neighbor contact than surface contact, leading to smaller structures. Thus, the interaction rules of collectively migrating cells are affected by surface adhesion, even though individual motility is not.

4.2. *Introduction*

The ability of cells to migrate across surfaces of differing composition is crucial in many biological systems. During the immune response or cancer metastasis, cells must travel through a variety of tissues en route to their destination

[225-227]. Similarly, to survive in the wild, the social amoeba *Dictyostelium discoideum* must be able to traverse a variety of surfaces, presumably with vastly different properties, using a variety of mechanisms [84, 228]. It is thought that cell-surface adhesion strength is an important determinant of how cells move on a specific surface. If a surface is too adherent, cells are able to adhere to but not de-adhere from the surface, fixing them in place. Conversely, a surface with insufficient adhesion does not permit a cell to gain sufficient traction, leading again to no overall motion. Surfaces with adhesivities between these two extremes allow cells to properly move in a directed manner [117, 229].

The survival of *Dictyostelium* cells requires that individual and collective migration be robust on many different surfaces. Few cell-cell adhesion receptors have been identified in this organism [128], and only one cell-surface receptor has been found [122]. However, other regulators (but not receptors) of cell-surface adhesion have been discovered [123], strongly suggesting that other unknown receptors exist. Adhesion receptors must be properly regulated, through control of their number on the surface (via transport to and from the membrane) and their binding properties, in order to allow proper adhesion to a surface.

Previous studies have investigated the migration of individual *Dictyostelium* cells to surfaces of varying adhesiveness, such as glass (adhesive), mica (non-adhesive), and lysine chains (adhesive) [119, 136, 137]. These studies focused on the difference between wild-type cells and various mutants in an attempt to discover the function of particular proteins in individual cell motion. For instance, cells lacking talin, an important membrane-cytoskeleton cross-linker, show decreased adhesion to

less adhesive surfaces but are still able to migrate effectively [136]. Cells lacking the motor protein myosin II have difficulty moving on very adhesive surfaces [119]. The majority of research in this area has not attempted to quantify the strength of cell-surface adhesion; the only study to do so investigated the cell-surface adhesion strength on glass for three mutants [230]. Crucially, no studies have looked at how surface adhesivity ties in to collective cell motion. Therefore, there are still several basic unanswered questions about the role of cell-surface adhesion strength in migration.

In this chapter, we answer several questions about the role of surface adhesiveness in individual and collective *Dictyostelium* motion. To provide a baseline of surface adhesiveness, we quantify the adhesion energy between cells and four different surfaces. Next we address the role of protrusion in adhesion and show that actin polymerization leads to increased adhesion on less adherent surfaces. Through time-lapse imaging of wild-type cell motion, we find that actomyosin-based protrusion and retraction lead to motion that is largely independent of surface adhesiveness, for adhesivities varying over several orders of magnitude. Finally, we investigate collective cell motion and discover that the dynamics of collective motion depend on surface adhesiveness.

4.3. *Results*

4.3.1. Experimental Surfaces

In order to study the effects of cell-surface adhesion, we used four surfaces with differing properties, the characteristics of which are shown in Table 4-1. The

122

four surfaces were chosen for their previously noted adhesion properties (see below) as well as the commonality of their use in biology laboratories. We also note that we chose the acid-wash and coating steps to match methods commonly used in adhesion and migration studies (see below). In all cases, acid-washed glass coverslips were coated with the functionalization of interest. We note that our contact angle measurements for glass, in particular (45°; see Section A.1.3) is higher than expected (about 15°; e.g. from plasma cleaning [231]); however, our treatment is consistent with what is used in cell migration studies [119, 232, 233]. We also note that water contact angle is a macroscopic measurement of a surface, and we cannot rule out inhomogeneities on a microscopic scale. Our migration and adhesion assays, therefore, use a large number of cells (at least 100) to average out any microscale differences that may occur.

The first surface chosen is **Bovine Serum Albumin (BSA; B in figures)**. This is a globular protein of 66 kDa commonly used in cell migration and adhesion studies to inhibit cell-surface adhesion [137]. BSA is a protein containing domains of various charges, and it has a negatively charged surface. As both BSA and glass have net negative surface charge, the adsorption of BSA to glass is thought to occur through BSA diffusing near the glass-liquid interface and changing conformation to display positive charges. This effect leads to BSA electrostatic adsorption to the surface, and the protein continues to change conformation until it reaches an equilibrium state [234]. This layer is thought to then weakly bind non-specifically to cell surfaces, preventing adhesion receptor access to strong binding sites [235].

Acid-washed glass (glass; G in figures) is the next surface. Glass has a negative charge and is known to allow cell-surface adhesion, though many mammalian cell types have difficulty migrating on it [236]. *Dictyostelium* cells are able to migrate effectively on glass, making it a commonly used surface for *Dictyostelium* studies [188, 220, 237].

Poly-L-Lysine (PLL; P in figures) is the third surface used. This is a polymer of L-lysine, a positively charged amino acid thought to bind electrostatically to glass. It is commonly used in laboratories as a surface that is highly adherent to cells. It is thought that the positively charged lysine molecules adhere to the cell surface electrostatically, as cell membranes are negatively charged [238].

The last surface used was a **perfluorinated carbon chain (FCC; F in figures)** chemically bonded to glass. This surface coating is neutrally charged and strongly hydrophobic, and it is similar to Teflon$^{\text{TM}}$ [239] brand coatings. While not commonly used in laboratory cell adhesion studies, it provided a contrast to the negative and positively charged surfaces of glass and PLL.

In addition, coverslips coated with poly(ethylene glycol) (PEG) were tested, which is thought to inhibit cell-surface adhesion through preventing protein absorption by steric repulsion [115, 240]. We found that cells were not able to adhere or migrate on this surface, in agreement with other researchers' findings [78]. Therefore, no PEG data are included in this study.

Table 4-1 – Surface Properties

Surface	Acid-Washed Glass (glass; G)	Bovine Serum Albumin (BSA; B)	Poly-L-Lysine (PLL; P)	Fluorinated Carbon Chain (FCC; F)
Weight	-	66 kDa (607 amino acids)	30-70 kDa (144-335 amino acids)	441 Da
Charge	Negative (Si-O⁻ exposed)	Outside is negative (but domains have different charges)	Positive	Non-polar
Hydro (philic/ phobic)	Hydrophilic	Hydrophilic	Hydrophilic	Hydrophobic
How adsorbs	-	Electrostatic. Can unfold when attached to glass	Electrostatic	Covalent Si-O-Si bond
Structure	SiO_2	Folded amino acid polymer	Polymer of Lys	$C_{10}H_{10}ClF_{13}Si$ [Tridecafluoro-1,1,2,2-tetra hydrooctyl dimethyl chlorosilane]

4.3.2. Measurements of Cell-Surface Adhesion

As the mechanisms of cell-surface adhesion in *Dictyostelium* are not well-known, we sought to measure the ability of cells to adhere to the prepared surfaces. To that end, the cells were treated with Latrunculin A, a drug that is able to enter cells and bind to monomeric G-actin, preventing its polymerization. The net result of thistreatment is that cells cannot form actin-based protrusions and their cortex is disrupted (as turnover rates for F-actin are in general less than one minute [241, 242]), causing them to remain in a spherical shape. They also cannot generate

actomyosin-based forces to push or pull against surfaces. These cells, therefore, should settle passively on each of the surfaces and form contacts based solely on a balance of adhesion forces with membrane resistance to flattening and stretching, similar to vesicles settling on a surface [243].

We measured the ability of *Dictyostelium* to adhere to surfaces using two methods. The first method, a shaking assay (commonly used as a gross estimate of cell-surface adhesion [244-246]), consists of placing populations of cells into an orbital shaker, shaking for 15 minutes, and counting the number of adhered cells (see Appendix A.1.4). We found that the cells adhered to PLL and FCC, less to glass, and not at all to BSA (see Figure 4.1 A). We take this result as a rough estimate of relative cell-surface adhesion ability.

A second method of measuring cell-surface adhesion is placing the cells on a surface and viewing them with simultaneous bright-field and interference reflection microscopy (IRM) using an inverted confocal microscope. IRM allows visualization of areas of close cell-surface contact, which appear dark in an otherwise bright image (see Figure 4.1 B; more details of IRM are described in Appendix A.1.2). Although this method does not measuring adhesion *per se*, the amount of area that a cell has in contact with a surface is likely to be related to the cell-surface adhesion, with more contact area corresponding to greater adhesion. Using this method we are able to measure the bright-field projected area of cells and the area of close cell-surface contact simultaneously. As can be seen in Figure 4.1 C, cells on BSA have little to no close contact area, cells on glass have somewhat more contact area, and cells on PLL

126
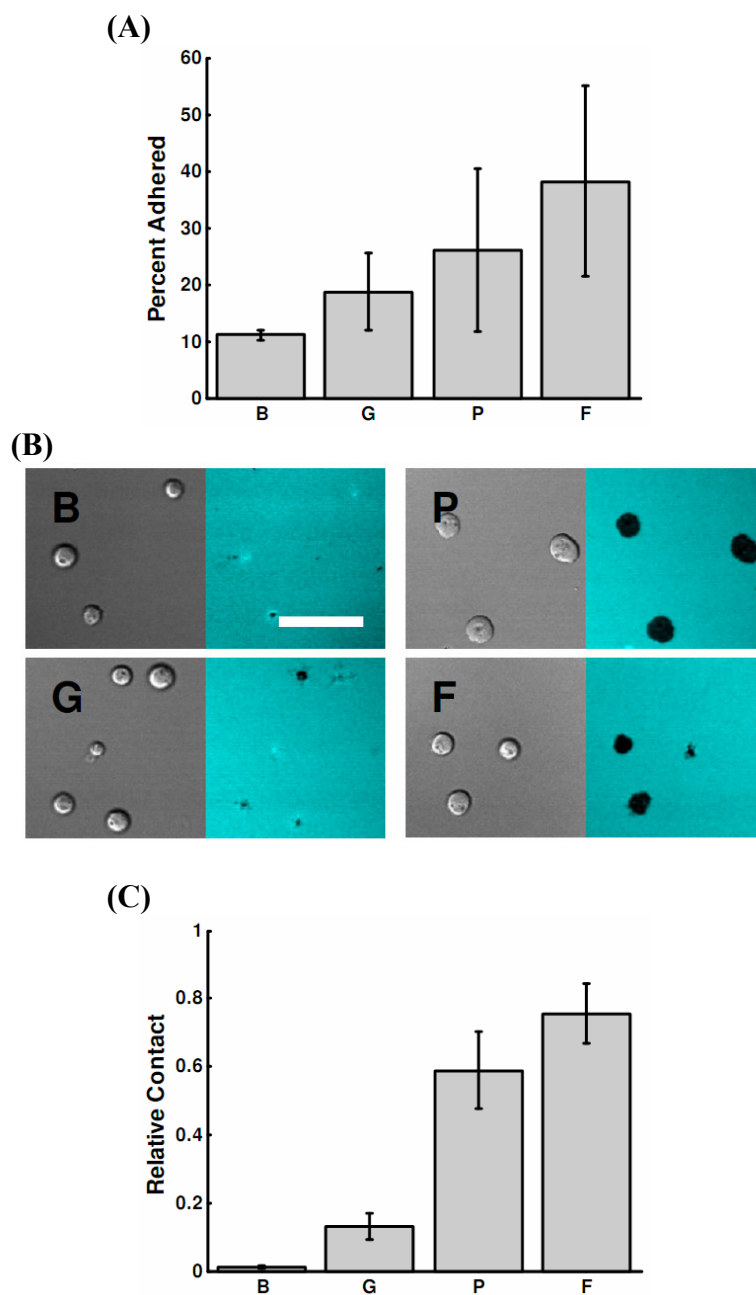
Figure 4.1 – Adhesion and Contact Area of Latrunculin A-treated Cells
Cells treated with Latrunculin A cannot polymerize actin, and as a result, can only settle passively and adhere to surfaces. (A) Shaking assay results indicate that cells are most adherent to FCC, then PLL, then glass, and barely to BSA (N=3). (B) Representative bright-field (left half of image) and IRM images (right half) of cells on different surfaces. Scale bar = 35 μm. (C) Quantification of relative contact: the bright-field area of the cell divided by the IRM area. Cells on BSA have little area in contact with the surface. Cells on glass have more area in contact, while cells on PLL and FCC have more than half their area in contact with the surface (N=3). Error bars indicate standard deviations.

or FCC have more than half their bright-field area in close contact with the surface. This trend is qualitatively similar to that found in the shaking assay.

4.3.3. Calculation of Cell-Surface Adhesion Energy

For better estimate of cell-surface adhesion, we now calculate the cell-surface adhesion energy using the bright-field and IRM images. Recent work by Murrell et al. derived analytical expressions for the adhesion energy of vesicles in contact with a surface as a function of their contact angle [247], and we follow their derivations below. Cells treated with Latrunculin should be able to be approximated as vesicles, as actin polymerization cannot occur, and the cells settle passively onto the surface, spreading until membrane tension forces balance spreading forces (similar to a liquid drop model). We note that the surface tension in this case is due to a cell membrane, which can be quite heterogeneous and contain membrane-stiffening and other membrane-affecting compounds [248] or have distinct domains of different composition [249]. However, some of these contributions should be able to be incorporated into model parameters, and so this model (explained below) should provide a rough estimate of the cell-surface adhesion energy.

For the model of [247] to be valid for our data, we must make the following assumptions:

- **The shape of the adhered cell is a truncated sphere.** Settled vesicles were shown to be this shape using confocal 3-D microscopy [230]. Similarly, Latrunculin A-treated cells in solution assume a spherical shape, as they cannot polymerize actin and therefore cannot easily deform their membrane.

128

On a surface, cells on glass and BSA roughly appear by eye to be truncated

spheres. On PLL and FCC, however, cells appear more extended due to

adhesion, and so may be flatter than truncated spheres. The 3-D shape of the

cells cannot be reconstructed from our data, so we cannot verify the cell

shape; however, this assumption should allow us to get an order-of-magnitude

estimate even if the shape is not strictly a truncated sphere.

- **The cell maintains the same volume before and after settling and does not change the amount of membrane on its surface.** The equilibrium shape is generally reached within one minute of settling (see Figure 4.2), which is short enough that significant volume change or membrane trafficking should not occur, especially as there is some interplay between the actin cytoskeleton (absent here) and membrane regulation [250].

Figure 4.3 shows a diagram of the relevant measures of a spread cell at

equilibrium. The contact angle is given by

$$\theta_c = \sin^{-1} \sqrt{A_{IRM} / A_{BF}} \, , \qquad\qquad (4.1)$$

where A_{IRM} is the dark region under the cell found through IRM, and A_{BF} is the area

of the cell in bright-field microscopy. This calculation assumes that the areas are

circular, as they would be for a truncated sphere.

Figure 4.4 shows a distribution of contact angles for cells on different surfaces.

The surface area of a truncated sphere is larger than that of a sphere of equal

volume. Therefore, the surface area of the cell must increase after settling. The

(A)
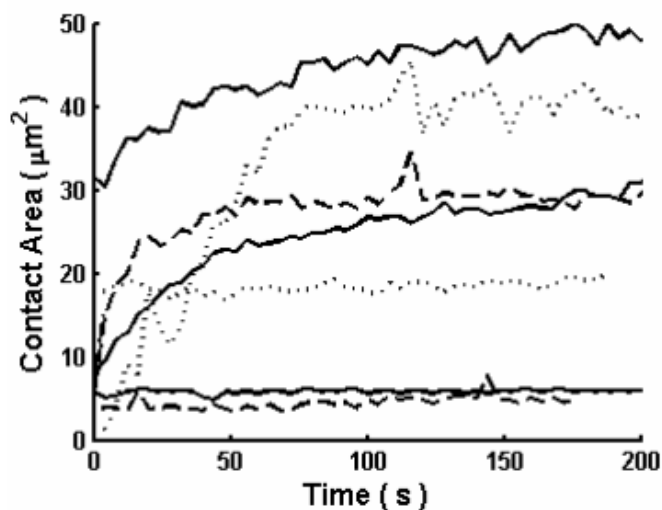
(B)
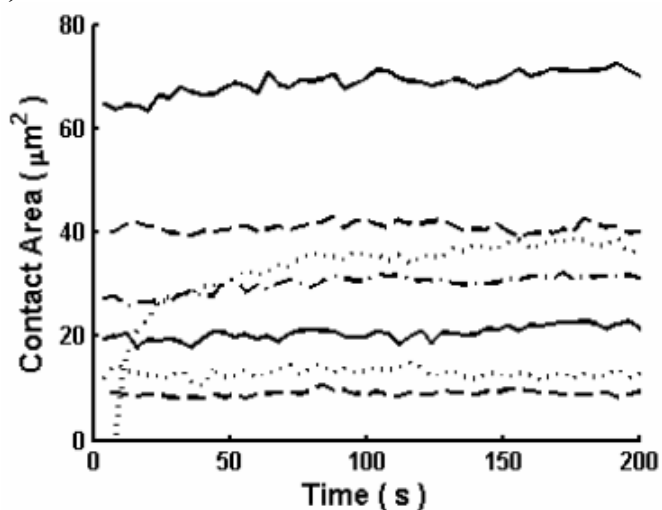
Figure 4.2 – Representative Contact Area Versus Time for Settling Latrunculin-Treated Cells
Time traces for seven representative cells for each surface, treated with Latrunculin
A. (A) Cells settling on glass. By ~60 seconds, most cells have reached their
equilibrium contact area. (B) Cells settling on PLL. Most cells reach their
equilibrium contact between frames, with a frame rate of 4 seconds.
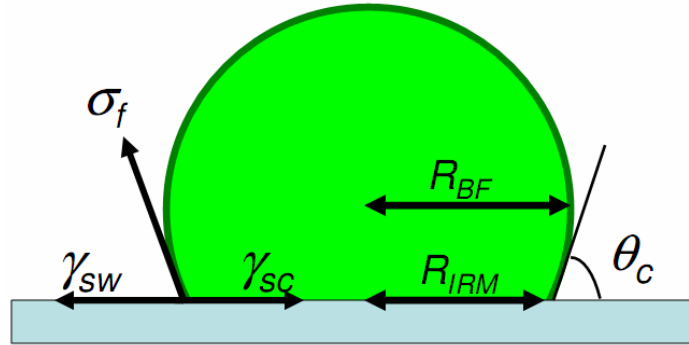
Figure 4.3 – Schematic of a Settled Cell
Cartoon of a cell settled on a surface in the shape of a truncated sphere. On the left are surface tensions, and on the right are the contact angle and the radii calculated from the bright-field and IRM areas. Adapted from [247].

increase is given by

$$\frac{\Delta S}{S_0} = \frac{2(1+\cos\theta_c)+\sin^2\theta_c}{4^{1/3}(2+3\cos\theta_c-\cos^3\theta_c)^{2/3}}-1,$$

(4.2)

where S_0 is the initial surface area and ΔS is the change in surface area. Increasing the surface area of the cell means that the membrane must be stretched, and doing so takes energy. A calculation from Murrell et al. [247] gives the change in surface area as a function of surface tension change, bending rigidity, and temperature:

$$\frac{\Delta S}{S_0} = \frac{k_B T}{8\pi\kappa}\ln\left(\frac{\sigma_f}{\sigma_0}\right) + \frac{\sigma_f - \sigma_0}{K_a},$$

(4.3)

where κ is the bending rigidity, K_a is the area expansion modulus, σ_f is the surface tension after adhesion, σ_0 is the surface tension before adhesion, k_B is Boltzmann's

(A)

(B)

(D)

(C)
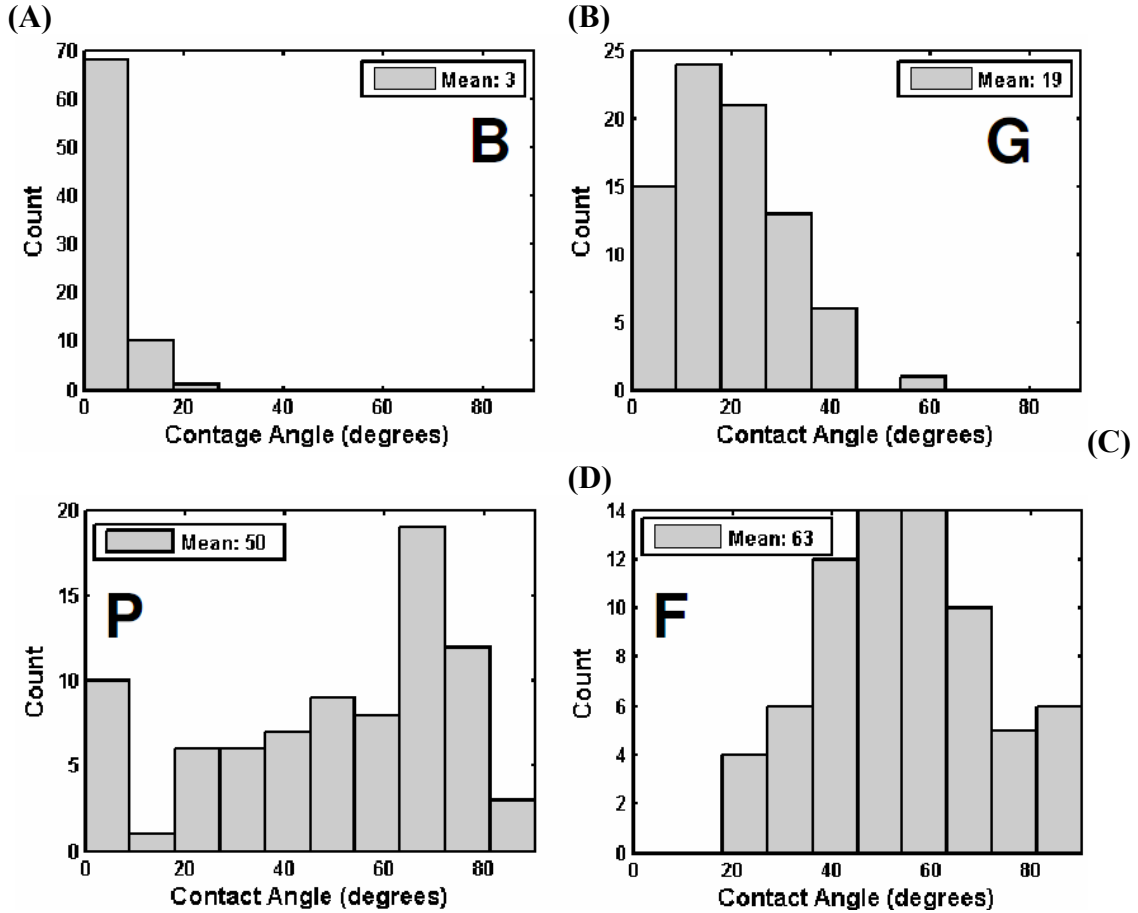
Figure 4.4 – Distribution of Contact Angles for Latrunculin-Treated Cells
Cells treated with Latrunculin A were allowed to settle on each surface, and the bright-field and IRM areas of each cell were recorded. The contact angle of each cell was calculated, assuming that the cells were truncated spheres. The mean contact angle is also shown. (A) BSA (B) Glass (C) PLL (D) FCC.

constant, and T is the absolute temperature. The first term on the right hand side is the contribution of membrane flattening, and the second term is the contribution from membrane stretching. Strictly speaking, the membrane does not physically stretch, but rather small entropically-preferred ruffles are smoothed out [243]. Here we take values from [230] calculated for *Dictyostelium* on glass under shear flow, specifically, $\kappa = 100\,k_B\,T$ and $\sigma_0 = 3*10^{-6}$ N/m. These values are for cortexillin-null

Dictyostelium mutants, which lack some F-actin crosslinkers and therefore should have a weaker cortex than wild-type cells [230]. These cells should be more similar to our Latrunculin-treated cells than wild-type cells would be; however, these values may be an overestimate, as cortexillin-null cells can still have actin-dependent stiffness. As a lower bound, floppy vesicles have σ_0 of order 10^{-6} N/m and κ of order $10\,k_B T$ [247, 249], so our estimates for each of these parameters should be at most an order of magnitude overestimation of the actual values. We let $K_a = 0.5$ N/m, which is mid-range for cells and bilayer vesicles [251], as the value specific to *Dictyostelium* is unknown. These three parameters can vary depending on membrane composition (e.g. cholesterol or protein concentration). Equating the two equations for $\dfrac{\Delta S}{S_0}$ therefore gives a relation between σ_f and θ_c.

Finally, the value of the adhesion energy density J can be found from σ_f as (from [247])

$$J = \sigma_f + \gamma_{SW} - \gamma_{SC},$$

(4.4)

where γ_{SW} is the surface tension at the surface-buffer interface and γ_{SC} is the surface tension at the surface-cell interface. Using Young's law of balance of surface tensions at the three-interface point (see Figure 4.3), we can also get

$$\sigma_f \cos\theta_c = \gamma_{SC} - \gamma_{SW},$$

(4.5)

and combining these last two equations gives

$$J = \sigma_f (1 - \cos\theta_c).$$

(4.6)

With our experimental contact angles we can therefore find J for each surface and thereby the total adhesion energy, given by $J*A_{IRM}$. Figure 4.5 shows the adhesion energy density and adhesion energy for each surface. A calculation of the adhesion energy using the floppy vesicle values as a lower bound ($\kappa = 10\,k_B\,T$ and $\sigma_0 = 1*10^{-6}$ N/m) gives energy values about one order of magnitude lower for each data point but keeps the graph otherwise unchanged.

We note the large spread in contact angles (and hence adhesion energies), which could be due either to inhomogeneities of the surfaces or differences between individual cells. The fabrication methods presented here, while in line with commonly used methods, cannot distinguish between these two possibilities. A surface fabrication method that can create homogeneous surfaces (as well as a method to verify surface homogeneity) will be required to elucidate the cause of the contact angle spread in the current experiments.

There is a significant spread in both contact angles (Figure 4.4) and adhesion energies (Figure 4.5). We note that the vesicles of Murrell et al. also showed significant contact angle spread (mean was ~50° with a standard deviation of ~15°), leading to energies spanning several orders of magnitude [247]. This spread could be due to inhomogeneities in their surface, the amount of binding receptors on the membrane, the amount of polymerized actin inside, or some other effect due to vesicle size or composition. The fact that this relatively simple system showed a large spread in values, as did our work, points to the inherent difficulty in measuring adhesion energy in this manner, and it emphasizes that the values obtained are estimates. Other methods, such as radial shear flow assays [252] or direct pulling

(A)

(B)
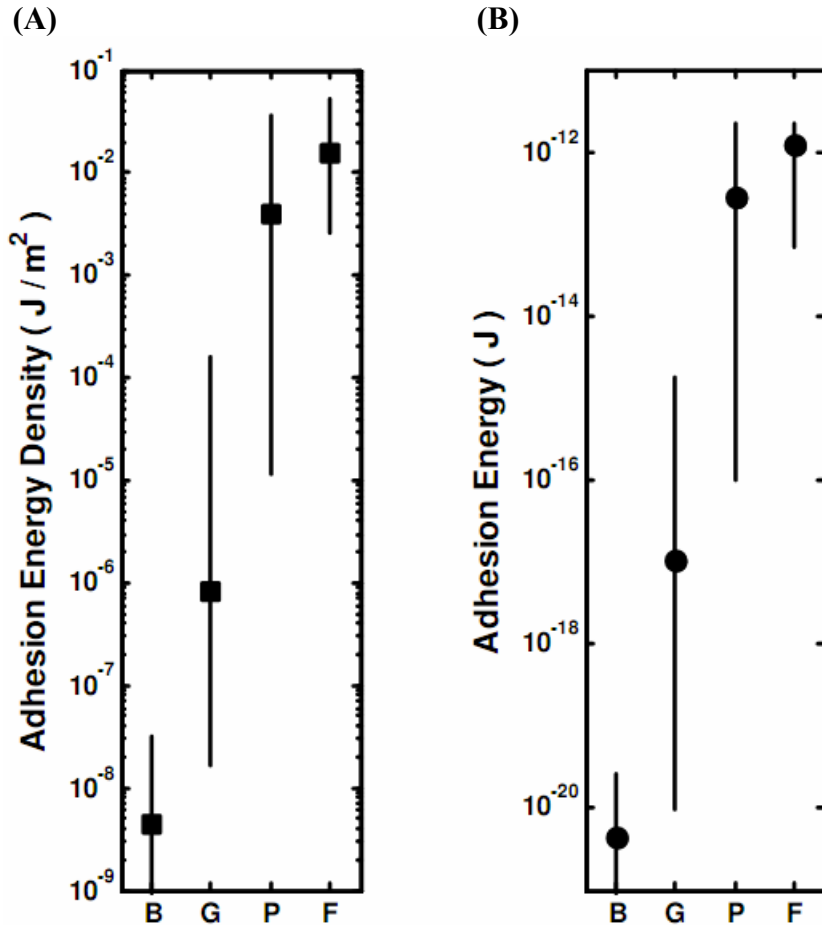
Figure 4.5 – Adhesion Energy Density and Adhesion Energy for Latrunculin Treated Cells
For each of these graphs, the marker value is the value corresponding to the mean contact angle, and the bars reach up and down one standard deviation in the contact angle. (A) Adhesion energy density for each surface. The values span seven orders of magnitude. (B) Adhesion energy on each surface. The values span nine orders of magnitude.

with AFM [253], may provide truly quantitative measurements of cell-surface adhesion.

Ideally, we would like to relate the total cell-surface adhesion energy on each surface to the results of shaking assay; i.e. we would like to find what adhesion energy the shaking assay is probing. One way of relating these two assays is to state that the shaking assay leaves cells with adhesion energies greater than a certain value. We plot this measure in Figure 4.6. This gives an estimate of about $10^{-16} - 10^{-14}$ J for
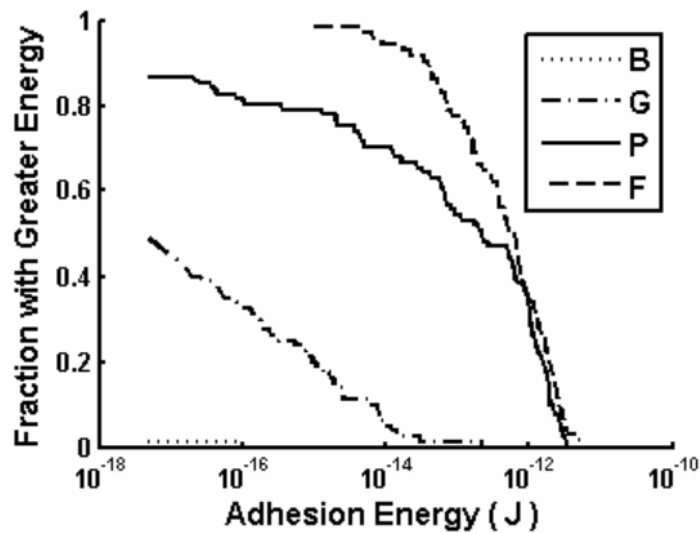
Figure 4.6 – Fraction of Cells with Greater Adhesion Energy
The adhesion energies were calculated for all the contact angles in Figure 4.4, and a cumulative distribution was obtained for the number of cells with a given contact energy. Assuming that the shaking adhesion assay pulls off cells below a given adhesion energy, this Figure, combined with Figure 4.1 A, suggests that the shaking assay pulls off cells with adhesion energies smaller than $10^{-16} – 10^{-14}$ J.

the adhesion energy cutoff in the shaking assay, although this is a rough estimate at best (see Discussion).

4.3.4. Actin-Based Protrusion Changes Adhesion Properties

Cell motion depends on the proper time regulation of localized force generation within a cell, which is heavily mediated through actin dynamics [226, 254]. To understand the role that protrusion and contraction each play in relation to cell-surface adhesion, we take the experimental step of adding the ability to polymerize actin to the cells. For these experiments we use myosin II knockout (*myoII⁻*) cells. These cells do not have myosin II and therefore are lacking a key motor protein in the generation of contractile forces (there are other myosins that can

136

still generate lesser contractile forces, however [255]). They remain fully capable of forming actin-based protrusions as well as an actin cortex, giving them the ability to spread on a surface, maintain a stable morphology, and move to a limited extent [119].

We hypothesize that these cells will be able to regulate their contact area and adhesion to some degree, with the ability to compensate for low cell-surface adhesion (through protrusion), though with less ability to compensate for high cell-surface adhesion (as they cannot create large contractile forces). Similar to the Latrunculin-treated cells, we subject these cells to a shaking assay as well as bright-field microscopy/IRM to measure their cell-surface adhesion and contact area. Unlike the Latrunculin-treated cells, we can make no assumptions about their shape and therefore cannot form an expression for their adhesion energy from IRM images; however, we can get qualitative information from the IRM contact area. Figure 4.7 shows the results of the shaking adhesion assay and contact area imaging. In the shaking assay, the *myoII⁻* cells showed less adhesion difference between surfaces, and almost half of the cells remained adhered. In looking at the IRM contact area measurements, however, there is a more significant difference between the contact areas on the surfaces. Notably, the cells are in contact most with the PLL surface, and less with glass and FCC, and then less with BSA. The results of these two assays therefore seem to be at odds (for the FCC results in particular), and we will address this issue in the Discussion.

(A)

(B)

(C)
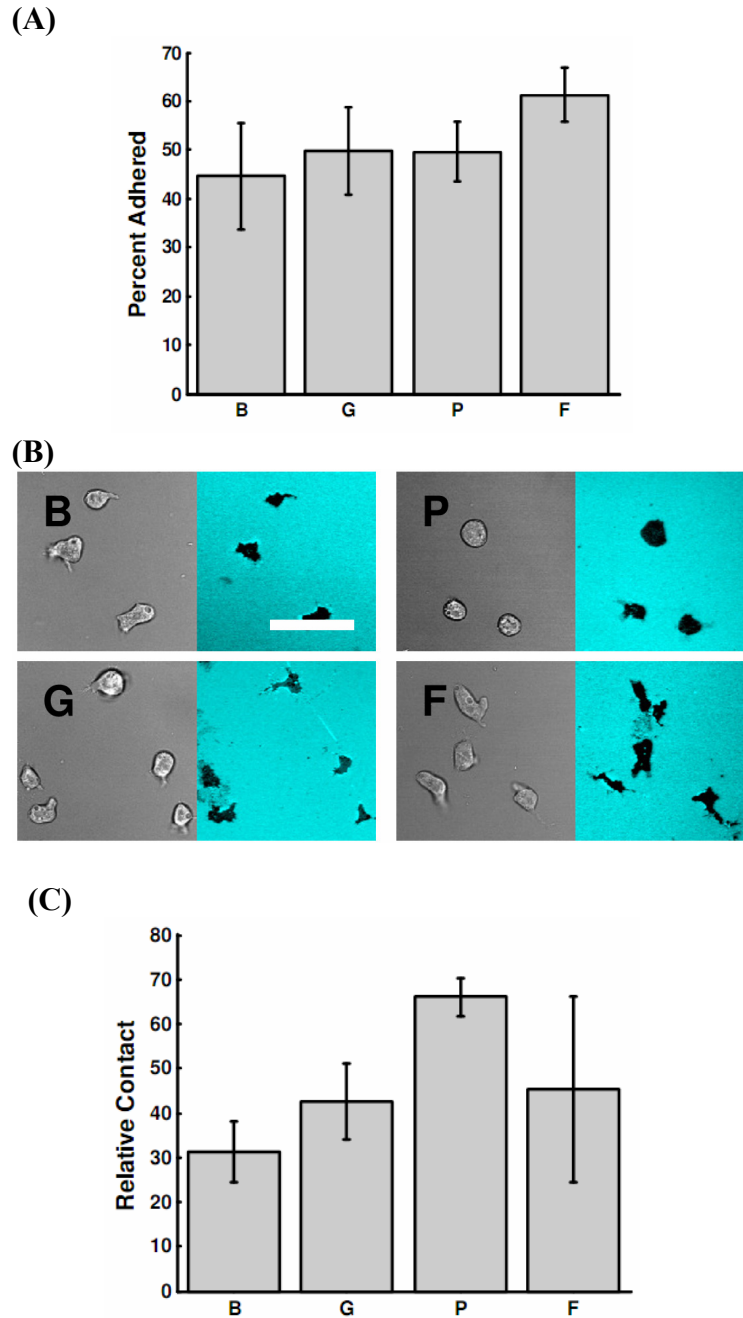
Figure 4.7 – Shaking Assay and Relative Contact Area for *myoII⁻* Cells
MyoII⁻ cells cannot generate large amounts of contractile force, although they can polymerize actin to form protrusions and an actin cortex. (A) In a shaking adhesion assay, *myoII⁻* cells adhere similarly to all surfaces (N=3). (B) Representative bright-field images of *myoII⁻* cells. Scale bar = 35 μm. (C) *MyoII⁻* cells have less contact with BSA than glass and FCC, and PLL has the most contact area. (N=3). Error bars indicate standard deviation.

138

4.3.5. Wild-Type Cells Actively Regulate Adhesion and Motion

Collectively migrating wild-type cells are able both to polymerize actin and generate contractile forces through the action of myosin II motor proteins. Therefore, we next allowed wild-type cells to migrate on each of the four surfaces. In this case the cells were fully motile and signaling to one another, and we took time-lapse bright-field and IRM images to measure various metrics of motion. The metrics that we measured were instantaneous speed, polarization (a measure of elongation), IRM contact area, and percentage of bright-field area that shows IRM contact ("relative contact area") (these definitions are detailed in Appendix A.2.3). Representative bright-field and IRM images are shown in Figure 4.8 A. Representative speed and relative contact area are shown as a function of time for two cells in Figure 4.8 B. Note the large fluctuations in both speed and relative contact area as a function of time. It is possible that surfaces of different adhesivities could show identical averages in the metrics but show different fluctuations, and therefore for each metric an average of the metric and an average of the metric fluctuations were calculated.

Remarkably, among the different surfaces no metric shows any significant difference; speed, relative contact area, IRM contact area, and polarization all are similar (see Figure 4.9). The fluctuation of speed of cells on FCC is the only measure that shows an increase. The similarity of all metrics suggests that wild-type cells have robust regulatory mechanisms in place that allow them to move effectively on all surfaces.

We then performed the shaking adhesion assay on wild-type cells, as shown in Figure 4.10. A large number of wild-type cells came off of the surfaces, and

139

investigation showed that the cells had begun the aggregation process previous to shaking. Cells in streams or aggregates will less surface adhesion per cell than individual cells, and in addition, they have a profile extending higher in the z-direction, which has stronger flows and therefore more force dislodging the cells. Therefore, we performed the same shaking assay with *aca*⁻ cells, which are not able to aggregate and remain as single cells. These cells have identical characteristics to wild-type cells except for their inability to aggregate (see Chapter 3 for a more thorough characterization). In the shaking assay, *aca*⁻ cells adhered equally to all four surfaces, as did WT cells (see Figure 4.10).

4.3.6. Mechanisms of Adhesion

The shaking adhesion assay and IRM contact angle measurements, two different measurements of cell-surface adhesion ability, reveal that wild-type cells maintain consistent shape and adhesion to the surface over a wide range of surface adhesivities. Previous work with traction-force microscopy on gel surfaces demonstrated that the forces generated by wild-type cells during migration are much higher than is required to overcome adhesion [135]. A recent mathematical model addressing the role of adhesion suggests that such large forces are a possible mechanism allowing cell speed to be largely independent of adhesive strength [116]. Regardless, this remarkable ability of cells to control their adhesion is actomyosin dependent, and we investigated this dependence through shaking adhesion assays and contact-angle measurements on three cell types: Latrunculin A- treated (no actin

140

(A)

(B)
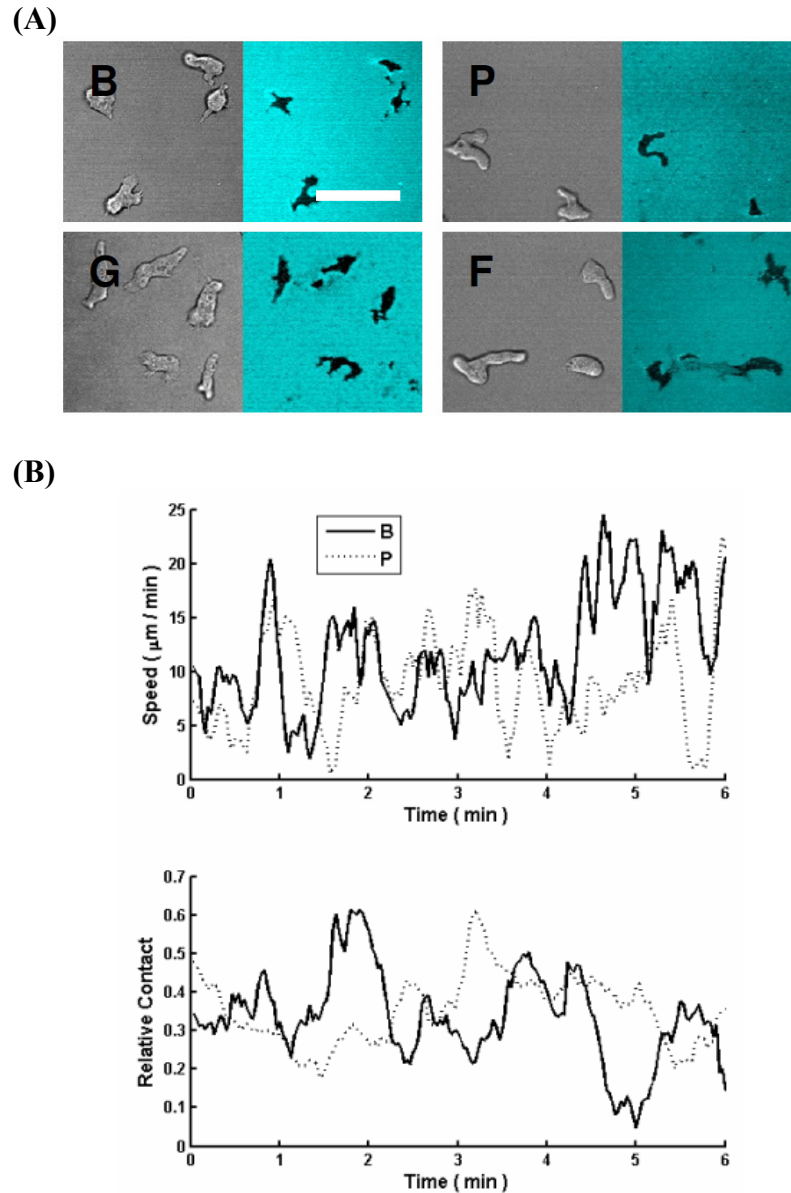
Figure 4.8 – Representative Data from Wild-Type Cells
Wild-type cells were imaged in bright-field and using IRM, and speed, polarization, contact area, and relative contact area were measured. (A) Representative images of wild-type cells on each of the surfaces. (B) Representative time traces of speed and relative contact for cells on two different surfaces. Each quantity shows large fluctuations about the mean, and they do not appear to be significantly different.

polymerization), *myoII⁻* cells (can polymerize actin but only have weak contraction ability), and wild-type cells (can polymerize actin and contract). To assist in this

141

comparison, Figure 4.11 overlays the previously-shown shaking adhesion assay and contact area measurements.

The shaking assay subjects cells to shear flows for 15 minutes. Presumably, wild-type cells and *myoII⁻* are moving on the surface during this time period. During the motion cycle, the contact area (and presumably adhesion) fluctuates, so this assay measures whether or not the minimum adhesion strength of the cell is sufficient to keep it on the surface. It is plausible that *myoII⁻* cells, with weakened contraction, will not be able to contract their body as much as wild-type cells during the motion cycle, causing a larger minimum contact area. Indeed, *myoII⁻* cells are known to have reduced speed on more adherent surfaces [119]. This view is consistent with the results of the shaking assay, in which *myoII⁻* cells were more adherent than wild-type cells on all surfaces. Time-lapse imaging of *myoII⁻* cells would reveal if these cells have a larger minimum contact area.

In contrast, the shaking assay shows that Latrunculin-treated cells have weakened adhesion on BSA, glass, and PLL in comparison to wild-type cells. This weakened adhesion is likely due to three main factors. First, the adhesion ability of Latrunculin-treated cells is less than that of wild-type cells (as suggested for glass and BSA contact-area measurements). Second, Latrunculin-treated cells do not spread out as much on the surface leading to increased cell height and therefore more force felt from fluid flows. Third, cells generally are able to respond to forces, so wild-type and *myoII⁻* cells can potentially resist pulling forces by increasing contact area through protrusions or other active strengthening of adhesion, whereas Latrunculin-treated cells cannot. These three factors could explain the apparent discrepancy

(A)

Average Speed
Speed Fluctuation

Speed (μm / min)

18
16
14
12
10
8
6
4
2
0

B   G   P   F

(B)

Average Polarization
Polarization Fluctuation

Polarization

2
1.5
1
0.5
0

B   G   P   F

(C)

Average Contact Area
Contact Area Fluctuation

Contact Area (μm^2)

40
35
30
25
20
15
10
5
0

B   G   P   F

(D)

Average Relative Contact
Relative Contact Fluctuation

Relative Contact

0.40
0.35
0.30
0.25
0.20
0.15
0.10
0.05
0

B   G   P   F
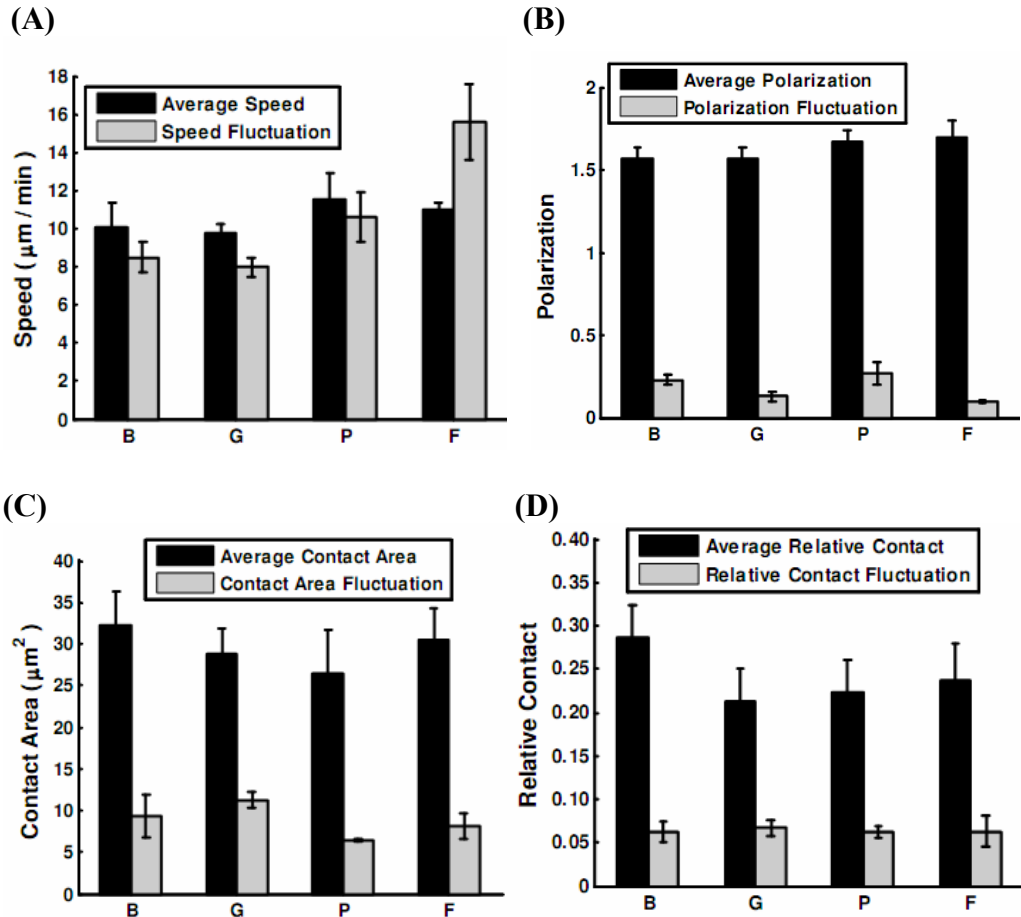
Figure 4.9 - Metrics of Motion for Wild-Type Cells
Time-lapse images of wild-type cells were taken and speed, contact area, relative contact area, and polarization were measured. The mean of each quantity was calculated, as was the average of the fluctuation of the metric. (A) Instantaneous speed (B) Polarization (a measure of elongation) (C) IRM contact area (D) Relative contact (IRM contact area divided by bright-field contact area). (N=3) The error bars indicate standard error of the mean.

between IRM contact angle measurements and shaking assay results. However, it should be noted that the forces felt by cells in the shaking assay are not homogeneous on the surface and potentially oscillate as a function of time. Therefore, to understand adhesion energy and truly quantitatively relate an adhesion assay to contact area requires another adhesion assay, potentially one that allows simultaneous well-
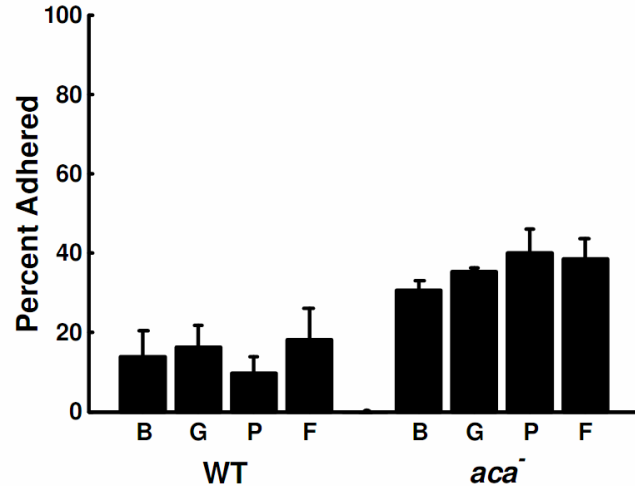
Figure 4.10 – Shaking Adhesion Assay for Wild-Type Cells
The shaking adhesion assay was performed on wild-type cells (left). A large majority of cells de-adhered, potentially due to cells being collectively migrating (see text). Therefore, we used *aca⁻* cells, which do not collectively migrate, to measure the adhesion ability of individual cells. There is little difference between the percentage adhered for each surface (N=3). The error bars indicate standard error of the mean.

characterized adhesion measurements and contact area measurements. One such

potential setup, coupling microfluidics to IRM microscopy, is shown in [230].

Measurements of contact area through IRM also revealed differences among

Latrunculin-treated, *myoII⁻*, and wild-type cells. While we did not measure the speed

of *myoII⁻* cells, the larger contact area on PLL agrees with their decreased inability to

pull off of this adhesive surface. On the other surfaces, *myoII⁻* cells have similar

contact areas (suggesting that the bond with FCC is not as strong as that with PLL),

as well as similar contact areas to wild-type cells. For Latrunculin-treated cells, the

contact area for BSA and glass is smaller by a significant amount than for wild-type

cells. This result shows that protrusion is required to adhere on these surfaces. In

contrast, Latrunculin-treated cells spread much more on PLL and FCC than do wild-

(A)

(B)
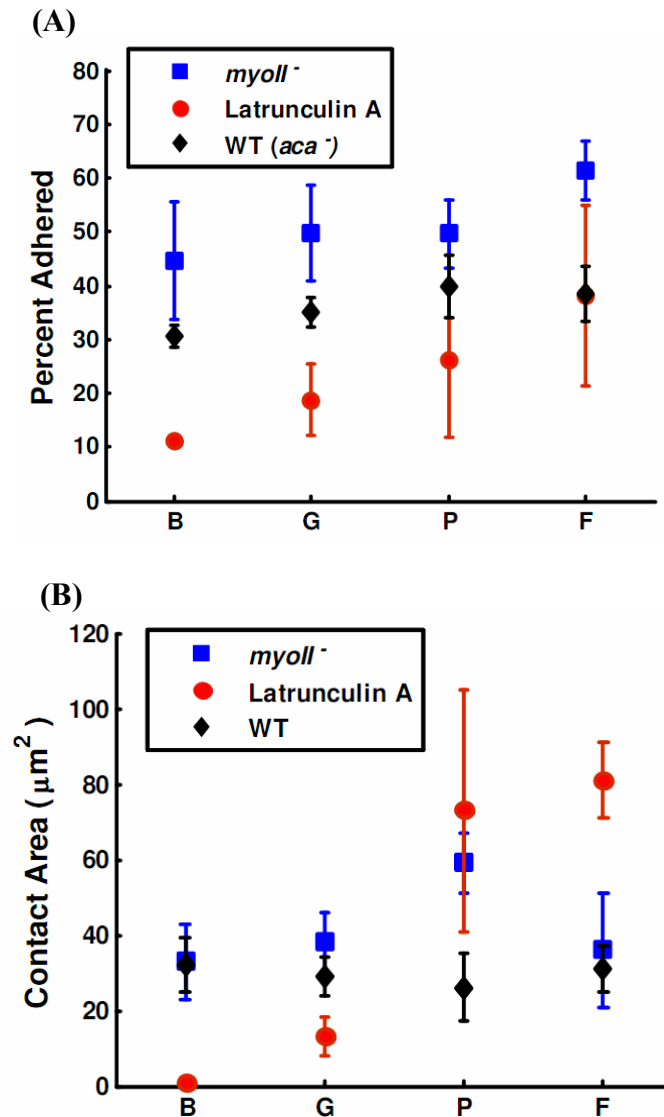
Figure 4.11 – Comparison of Shaking Assay and Contact Area Measurements
Graphs depicting overlays of the previously shown data for (A) Shaking adhesion assay and (B) IRM contact area.

type cells (and than do *myoII⁻* on FCC), suggesting that for these strongly-adherent

surfaces cell contractility and mechanical stability are important.

4.3.7. Cells Are Able to Adapt to and Distinguish Among Different Surfaces

To probe the mechanics of how cells are able to move equally on all surfaces, the cells were chemically fixed (immobilized) (see Appendix A.1.2). Fluorescently-dyed phalloidin, which binds to F-actin, was added, and the cells were imaged (see Figure 4.12). Although the metrics of motion are essentially the same on all surfaces, the F-actin distribution varies dramatically. On BSA, the F-actin network is diffuse. In contrast, even when the excitation power was decreased by almost 50%, the F-actin network showed up more brightly on glass. Decreasing the excitation power again by over 50% still produced strong fluorescence in cells on PLL. Therefore, the qualitative level of F-actin in cells increases with increasing surface adhesion. This finding suggests that cells are able to actively compensate for surface adhesiveness by strengthening their actin cortex, providing mechanical stability and also allowing for the generation of more contractile forces.

Cells show the ability to modify their actin levels based on surface adhesiveness. A method of probing the regulatory mechanisms of adaptation is to present a cell with an interface between two surfaces, and find out if a cell will cross surfaces; and if so, how fast a cell can adapt to a new surface.

We created surfaces containing a glass-PLL interface (see Appendix A.1.3) and acquired time-lapse images of cells migrating (see Figure 4.13 A). We then measured the metrics of the previous section for cells on either side of the interface, as well as for cells that made the transition from one surface to another. Cells that never crossed an interface showed dynamics identical to the previous section, i.e. no significant difference (data not shown). Cells that crossed the interface also showed
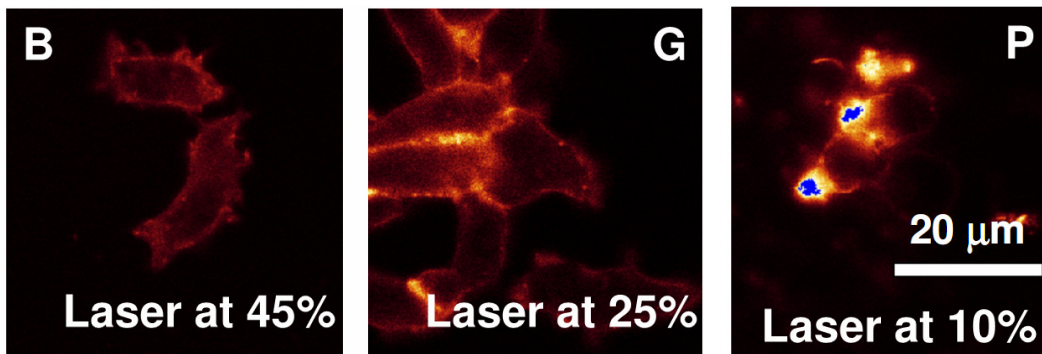
Figure 4.12 – Representative Images of Phalloidin-Stained Cells
Images acquired by E. Rericha. Cells on three of the surfaces (BSA, Glass, PLL) were fixed and stained with fluorescently-labeled phalloidin, which binds to F-actin. Note that the apparent brightness (a qualitative measure of amount of actin) increases from BSA to glass, as well as from glass to PLL. In addition, the laser power (which excites the fluorescent dye) was lowered from BSA to glass to PLL, showing that the increase is significantly more than is apparent from these images. Blue indicates saturated pixels.

no change in the metrics. In addition, cells did not show a significant 'lag time' to adapt to the new surfaces; they moved as if the interface was not even there (see Figure 4.13 B). This result shows that cells have the ability to adapt to new surfaces on times of order one minute. Figure 4.14 shows average measures for each surface for cells that crossed the interface, and there are no statistically significant differences.

Curiously, cell behavior suggests a propensity to 'prefer' one surface over the other, though cells ably cross from glass to PLL and PLL to glass. When cells on PLL contacted a PLL-glass interface, 7 of 9 cells crossed over to glass, while 2 turned back. Conversely, of 5 cells approaching the interface from glass, only one crossed to the PLL surface. In light of motion metrics being unchanged on the surfaces, this is suggestive of an interesting finding: cells are able to quickly adapt to new surfaces, but they also can show a preference, in this case for the less-adhesive surface.

(A)

(B)
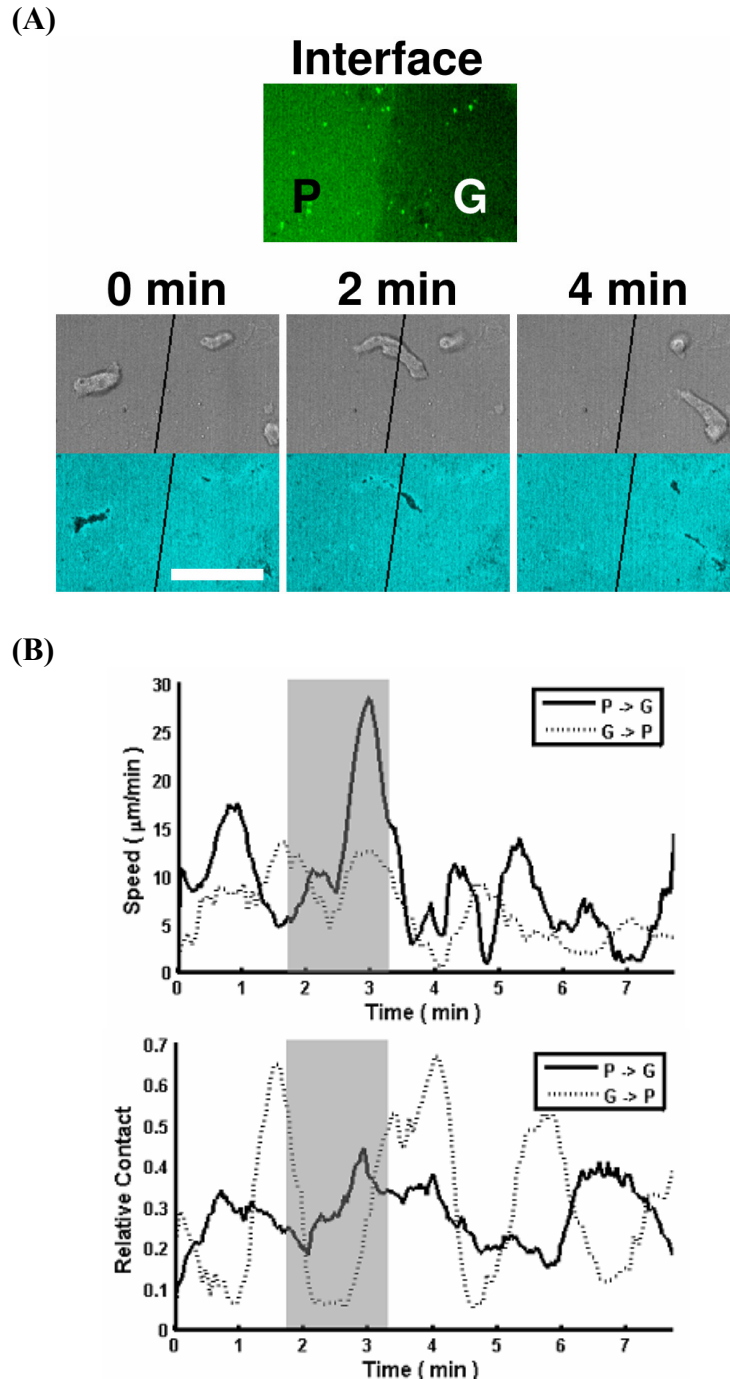
Figure 4.13 - Representative Cells at an Interface
Interfaces between PLL and glass were created to see how cells adapted to new surfaces. (A) (Top) Fluorescence image of PLL (fluorescently labeled) and glass showing an interface. (Bottom) Three bright-field and IRM images of a representative cell crossing from PLL to glass over a four minute period. (B) Speed and relative contact for representative cells crossing from PLL to glass or glass to PLL. The gray bar denotes period in contact with the interface. Note that the metrics are similar before and after touching the interface, indicating that cells adapt to the new surfaces in around a minute.
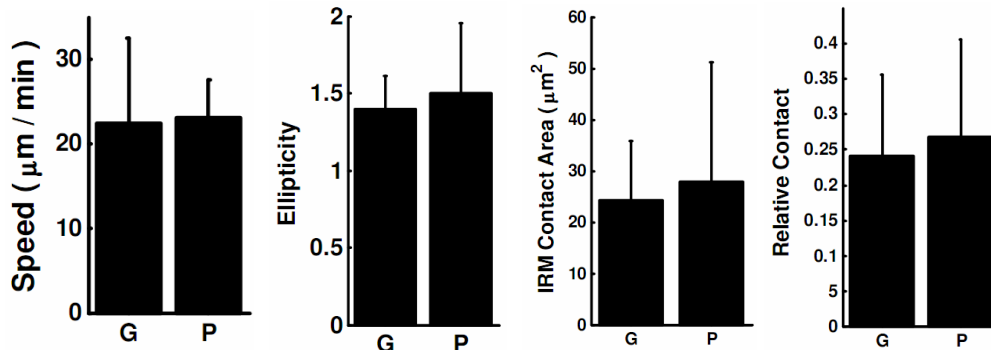
Figure 4.14 – Average Metrics for Cells Crossing an Interface
The same metrics as Figure 4.9 show no statistically significant change for cells crossing a glass-PLL interface (N=12 cells).

4.3.8. Surface Properties Alter Collective Cell Migration

Although WT cells maintain robust motion on a variety of surfaces, their ability to 'distinguish' among different surfaces leads to an interesting question: when cells start to encounter other cells (and therefore form contacts with cells as well as with the surface), will the cells behave differently on different surfaces? During aggregation, cell-to-cell cAMP signaling results in cells forming head-to-tail chains termed 'streams' that move to the aggregation center [98, 105]. Each cell in a stream is simultaneously in contact with other cells in the stream as well as with the surface, and therefore altering the relative strengths of cell-cell and cell-surface adhesion may affect collective motion.

We imaged initially uniform densities of cells aggregating on the four surfaces for several hours, until stable aggregation centers were formed (see Figure 4.15). The cells displayed surface-dependent aggregation: on BSA, stable aggregation centers form quickly, and spatially extended streams of cells move towards those aggregation

centers. On glass, there are initially more aggregation centers, some of which

coalesce into others, and the streams are not as spatially extended and often break up

and reform. On PLL and FCC, almost no streams are observed. Instead, cells form

small clumps with their immediate neighbors, and these clumps coalesce together into

larger clumps, eventually forming aggregation centers. At the end of the

experiments, all surfaces have similar number of aggregation centers. Therefore, the

aggregation dynamics change based on the surface adhesiveness, although the end

result is the same.

In order to quantify this aggregation difference, we used the following metric.

At each time point, the images were binarized, with cells, streams, and aggregation

centers as the foreground. Next the morphological 'skeleton' operation was applied,

which pared down objects into a pixel-wide backbone that keeps the same essential

shape as the object (see Figure 4.16). For instance, large circles will become single

pixels (which have the same essential round shape), but spatially extended branching

objects will become single-pixel wide spatially extended branching objects. After

this operation, the total number of pixels in each object is counted. This procedure

allows for quantification of the spatial extent of objects that would otherwise have the

same number of pixels. A representative set of skeleton sizes versus time is shown in

Figure 4.17 A, and the average peak skeleton size of three aggregation data sets is

shown in Figure 4.17 B. This metric points out the difference between the data sets:

the skeletons, and hence spatial extent, of groups of cells on BSA is larger than on

glass, which in turn is larger than on PLL or FCC.
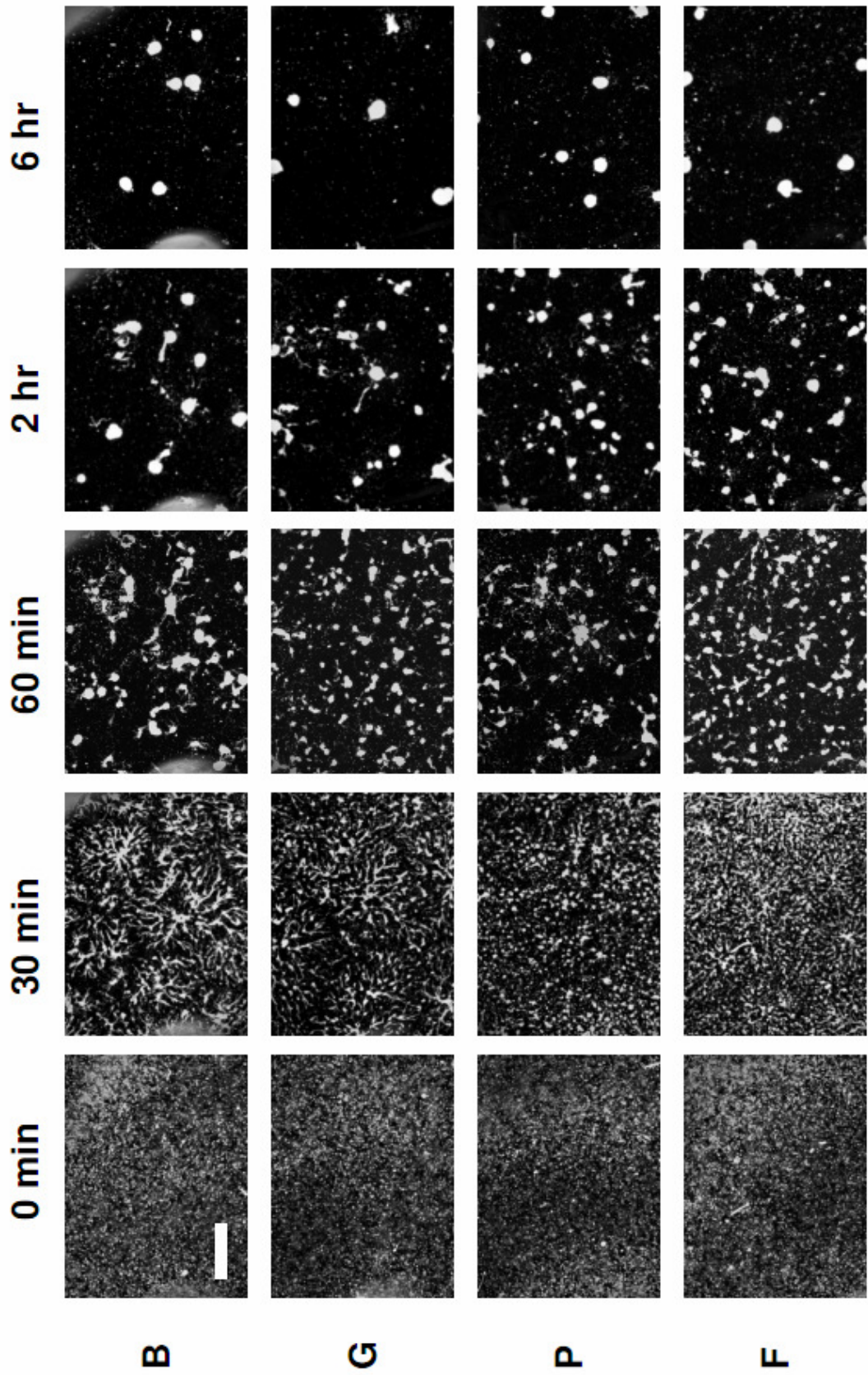
Figure 4.15 – Montage of Aggregating Cells on Each Surface
(From previous page) Low-magnification dark-field images of cells aggregating on BSA, glass, PLL, and FCC. The initial conditions (0 min) and final conditions (6 hr) are similar in all images; however, the intervening dynamics are different. Cells on BSA show large streams (visible at 30 min), and cells on glass show slightly smaller ones (30 min). Cells on PLL and FCC at 30 min show few streams at all. At 60 min and 2 hr, cells on BSA have noticeably fewer aggregation centers than cells on glass, which in turn has far fewer aggregation centers than cells on PLL or FCC. Scale bar = 400 μm.

4.4. *Discussion*

In this Chapter, we investigated how individual and collective migration of cells depends on surface adhesiveness. Using cells in which actin polymerization is inhibited, we established the adhesion energy density and adhesion energy of the cell-surface bond on each surface. To our knowledge, the adhesion energies of *Dictyostelium* cells on substrates of varying adhesivities have not been measured previously. The only previous measurement was on glass for wild-type cells and mutants lacking cortexillins and talin [230]. Our adhesion energy for glass ($\sim 10^{-6}$ J/m^2, Figure 4.5 A) is similar to that measured on glass for cells lacking talin ($6*10^{-6}$ J/m^2) [230], an important protein that links the actin cortex to the membrane. Therefore, our measurements of cell-surface adhesion energies agree with other results to within an order of magnitude.

Our results indicate that the adhesion energies of PLL and FCC are orders of magnitude higher than glass, while BSA-covered glass has adhesion energies orders of magnitude lower than glass. BSA, used as a non-specific block of adhesion in

(A)
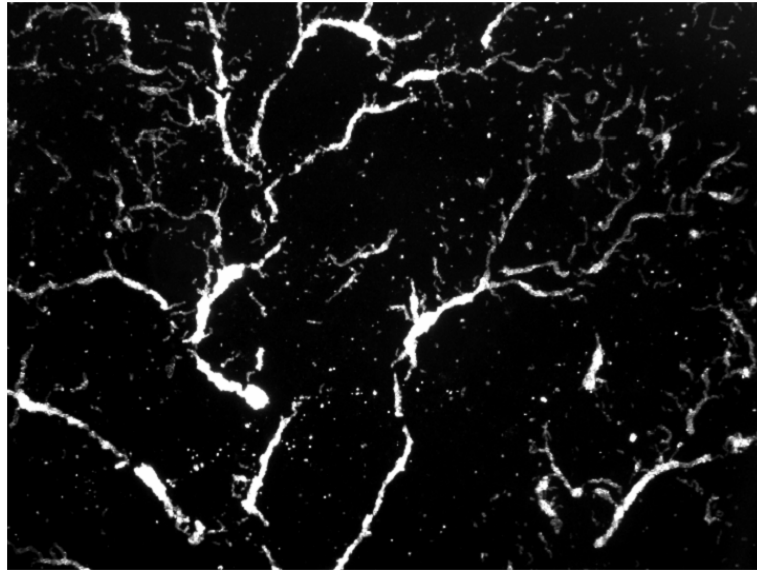
(B)
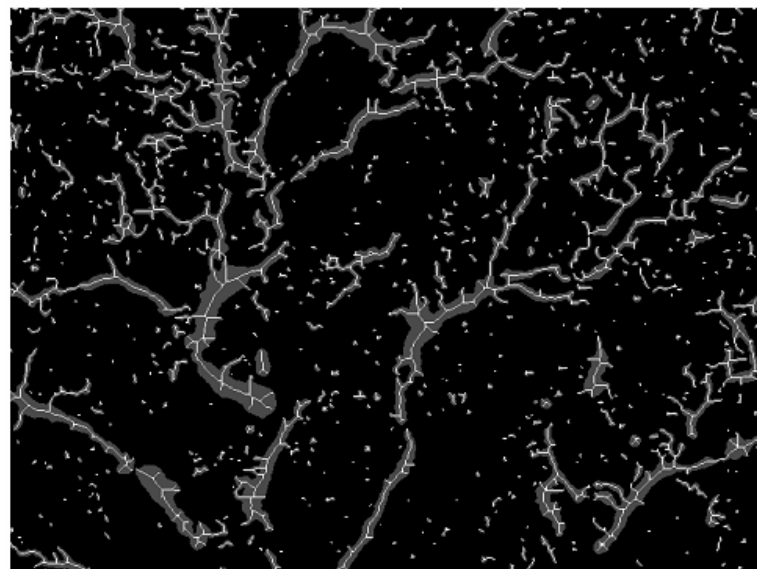
Figure 4.16 – Illustration of Skeletonization
To establish a metric highlighting the different aggregation dynamics on each surface, we chose the morphological skeletonization operation (see main text). (A) Dark-field image of a field of aggregating cells. (B) Skeletonization (white) is shown on a binarized image in which all cells are gray and background is black.

laboratory contexts, does cause the cells to adhere weakly to the surface as expected.

Cells are able to bind to glass, but glass is negatively charged, as is the cell membrane

[125]. This electrostatic repulsion will only be felt at close range, as it is screened for

distances greater than the Debye length, which is given by [256]:

$$\lambda_D = \frac{0.304 \text{ nm}}{\sqrt{c_0 \left(\dfrac{L}{mol} \right)}} \cdot \tag{4.7}$$

In our buffer (10 mM phosphate buffer, see Appendix A.1.1) the Debye length is ~3

nm. In fact, other studies show that for larger Debye lengths ($c_0 = 0.17$ mM, $\lambda_D \sim 25$

nm), *Dictyostelium* cells simply hover above a glass surface due to electrostatic

repulsion [125]. While the close-range repulsion in our buffer may hinder spreading

on glass, the fact that cells can closely contact glass indicate that they have adhesion

receptors that are able to bind to negatively-charged surfaces. PLL, a positively-

charged chain, is strongly adhesive to cells, likely due to its positive charge

electrostatically attracting the cell membrane at close range, in addition to the

possible action of adhesion receptors. FCC is strongly adherent to cells as well,

which is likely due to cell surface adhesion receptors able to bind strongly to

hydrophobic surfaces. There also is no electrostatic repulsion or attraction between

the surface and the cell membrane.

Further investigations showed that wild-type cells display a remarkable ability

to adapt to new surfaces quickly, as they are able to cross interfaces with no change in

speed or contact area. The ability to adapt to new surfaces quickly has been shown in

another amoeboid cell type [118], which increases its actin treadmilling rate to

compensate for reduced traction on less adhesive surfaces, even in different parts of

the same cell straddling an interface. Our data do not discount actin treadmilling as

(A)

(B)
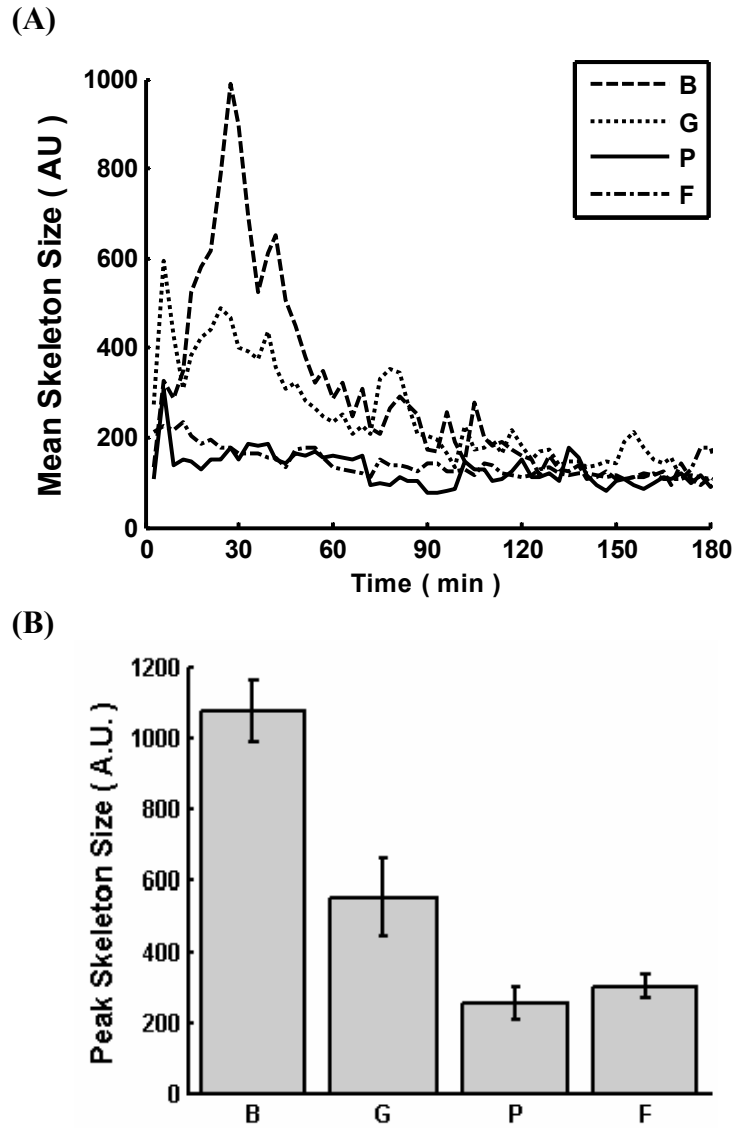
Figure 4.17 – Metric of Aggregation Dynamics
(A) Representative time trace of mean skeleton size (see Figure 4.16) for the top 1% of objects in an image as a function of time. Note the large peak in BSA, the smaller peak in glass, and small to no peaks in PLL and FCC. (B) Average peak skeleton size for 3 experiments. The error bars indicate the standard error of the mean.

one method of adapting to a new surface, but we find that *Dictyostelium* cells increase

the amount of actin in the cortex on more adhesive surfaces. This observation

suggests that strengthening the cortex can occur on timescales of tens of seconds,

though further experiments could quantitatively verify this possibility. In addition,

cells display a seeming 'preference' for glass surfaces over PLL surfaces when presented with a choice, showing that cells can 'differentiate' among surfaces of varying adhesivities while maintaining the ability to move on either. Intuitively one would expect cells to 'prefer' the more adhesive surface, as contractile forces applied over the cell body would pull the cell off of the less adherent surface first.

We conjecture that a possible mechanism explaining our unintuitive results is that contacting a more adhesive surface may cause a local increase in cortex tension due to greater spreading and the cell increasing its resistance to spreading. Work by Fischer et al recently showed that endothelial cells show increased protrusion rates in cell locations lacking myosin II [257], suggesting that decreased local cortical tension may promote local protrusion. If a cell experienced local tension differences due to surface adhesion, this effect could lead to protrusion in the direction of the less adhesive surface and hence drive a 'preference' for moving toward the less adhesive surface. Further experiments would have to be performed to evaluate if this conjectured mechanism is possible in *Dictyostelium*. Other work shows that *Dictyostelium* cells showed 'preference' when presented with changes in surface roughness [258] (though the mechanism is unknown), but to our knowledge such work has never been performed for surface adhesiveness.

The dynamics of aggregation change based on cell-surface adhesion, with cells on more adhesive surfaces aggregating through a process of clumping, as opposed to the streaming normally seen. We speculate that this process could be due to the 'preference' found in the interface experiment: when faced with an adhesive and a non-adhesive surface, cells tend to move on the less adhesive surface. In

collective migration, the strongly adhesive surfaces of PLL or FCC cause the cells to move on top of their neighbors instead of the surface, forming clumps that are attracted to other clumps through cAMP signaling. In contrast, on BSA cells prefer to move on the surface instead of one another, forming long streams that have large amounts of cell-surface contact. Cells moving on glass fall in between these two extremes. The endpoint of aggregation, however, is governed by quorum-sensing factors [87], and therefore whatever collective motion the cells undergo must have the same endpoint. Therefore, our findings highlight that the behavior resulting from the interaction of thousands of individual cells can change based on alterations in local rules (in our case, altering the relative strengths of cell-cell and cell-surface adhesion) due to environmental factors.

In summary, *Dictyostelium discoideum* cells are able to regulate their cell-surface adhesion so as to robustly migrate across various surfaces with the same speed, shape, and contact area, and this regulation is actomyosin-dependent. However, the dynamics of collective cell motion depend dramatically on cell-surface adhesion. The fact that this interplay exists suggests that surfaces may have roles in regulating population behavior that are not readily apparent, and that understanding and predicting collective cell motion is not as simple as observing the motion of cells acting as individuals.

5. Discussion

5.1. *Summary*

Understanding the rules that govern collective cell behavior is a task involving multiple size scales: sub-cellular biochemistry and signaling pathways; cell-scale protrusions, adhesion, and retraction; and multicellular aggregation patterns caused by cells releasing a chemotactic signal. At the scale of sub-cellular biochemistry and signaling pathways, stability analysis of a model of gradient sensing found that polarized cells are most sensitive to signals at angles of about 60 degrees relative to their polarization axis (Chapter 2). This off-axis sensitivity is suggestive of the zig-zag motion that cells during motion up a chemical gradient. Our analysis of center-of-mass motion showed that cells move persistently, but not ballistically, over minute timescales (Chapter 3). These observations are again consistent with a zig-zag motion pattern. We found that a directional signal is required to maintain this persistence for longer times, although it does not straighten the tracks significantly. Individual cells maintained this migratory ability for a range of signal strengths, as well as across a variety of surface adhesivities (Chapter 4). At the multicellular scale, the persistent motion observed in individual cells was also found in cells moving collectively inside streams, indicating that streams do not speed cells up or provide more straightness to cell tracks. In addition, collective cell motion depends on surface adhesiveness, showing that the compensation methods used by individual cells to move on adhesive surfaces alter collective dynamics. Below we expand upon

these findings, and we propose future directions based on the research presented in this thesis.

5.2. *Conclusions and Future Work*

5.2.1. Stability Analysis of a Model of Gradient Sensing

In Chapter 2 we explored a theoretical model of gradient sensing applicable to *Dictyostelium discoideum* cells.

Linear stability analysis on an initially unpolarized (quiescent) state demonstrated that the model was linearly stable to spatially uniform concentrations, but its stability to a gradient perturbation depended on the model parameters. This result highlights one strength of perturbation analysis: qualitative changes in stability are apparent in different regions of parameter space. In a real cell, parameters could potentially vary due to protein expression levels, drugs, or other factors, and thus the cell could respond differently to perturbations, such as signals from nearby cells. Therefore, adjusting the biochemical parameters of gradient-sensing may potentially cause a transition, for example, between states in which receptor noise is or is not sufficient to cause a sustained polarizing response. In fact, recent experimental work by Arai et al. demonstrated that the gradient-sensing pathway of *Dictyostelium* can weakly self-organize (i.e. polarize) transiently, lasting only seconds [75]. However, when caffeine treated, the gradient-sensing pathway can self-organize for minutes or longer, even without an external gradient. As caffeine is known to alter the activity of the PI3K pathway, it potentially alters the cell's sensing parameters into a regime sensitive to polarization due to noise.

Experimental means to test predictions about responses of the signaling pathway are now becoming viable. Spinning-disk confocal microscopes are able to image three-dimensional cells with sub-micron accuracy in seconds [259], which would allow for imaging of fluorescently-labeled proteins in quiescent (rounded) *Dictyostelium* cells. Simply imaging cells at high resolution, without any external stimulus, would allow for testing of instability to perturbations in gradient-sensing as well as discovery of timescales of perturbation die-off. If either of these methods were applied to cell populations, it would indicate the parameter space spanned by real cells.

In Chapter 2 we also performed linear stability analysis on an initially polarized cell and found that the least stable mode corresponded to perturbations that were ~60 degrees off of the axis of polarization. This result suggested sensitivity to stimuli in that direction. Therefore, we subjected our model to an external point-source stimulus at various distances and angles (with respect to the initial polarization) and found that the model responded most strongly in the 40-80 degree region. That is, the angle of strongest response 'overshot' small-angle perturbations and 'undershot' large-angle perturbations. This result demonstrated that for our model, linear stability analysis provided a good intuition about the response of the complete model.

Testing the stability of real cells in a gradient could be performed with microfluidic devices able to create finely tunable gradients. These devices allow for the creation of well-defined temporal and spatial chemical environments. Combining these devices with confocal microscopy would allow for the testing of response to changing gradients, and indeed this work is currently in progress in *Dictyostelium*

[109]. Combining these two devices with photo-uncaging technology [187] could test the exact setup simulated with the model: an initially polarized cell exposed to pulses of cAMP at defined angles and distances. Furthermore, different angles could be tested with a single cell, not only testing undershoot and overshoot of response but also probing timescale and parameter variation among different individuals. Thus the technology exists to test most of the stability predictions made by this model.

An interesting extension of the model itself would be to investigate how cell shape affects sensing. Testing the model on a different geometry, e.g. one that mimics the shape of an elongated *Dictyostelium* cell, could facilitate predictions about the response of the model to various external stimuli as a function of aspect ratio. Although gradient-sensing experiments on immobilized elongated cells have not yet been carried out, they present an interesting test of the model's (and any gradient-sensing model's) predictive power.

An important question is how gradient sensing is coupled to cell motion. We showed how the off-polarization axis sensitivity of the gradient sensing pathway is suggestive of actual zig-zag motion of cells in a linear gradient. However, fully understanding how gradient sensing feeds into motion first requires some idea of how cells propel themselves. A possible next step in studying the coupling of gradient sensing and motion is to track the boundaries of cells in which the gradient-sensing machinery has been fluorescently labeled. This approach could illuminate the cause-effect relationship between gradient-sensing and motion and reveal the time required to go from signal to protrusion. Recent studies have indicated that signaling molecules localize to the membrane before protrusion and remain at the protrusion

site until the protrusion stops growing [109], although not all signaling molecule localization resulted in protrusions and not all protrusions showed signaling molecule localization. In addition to purely observational experiments, researchers have recently created photo-activatable variants of molecules downstream of gradient-sensing and shown that their artificial activation is able to drive localized protrusion in HeLa cells [260].

Modeling motion caused by localized generation of curvature waves *in silico* and coupling it to a steering system such as that of Chapter 2 could potentially produce a model that generates realistic chemotactic motion. Such a model in turn would drive experiments to test predictions of the model, leading to a much greater understanding of the rules governing chemotaxis and cell motion in general.

5.2.2. Cell-Cell Signaling and Collective Motion

In Chapter 3 we presented quantitative analyses on cells performing collective migration.

We found that cells displayed persistent, but not straight-line, motion over short time scales (< 3 min). A 'zig-zag' type of protrusive activity (where cells extend pseudopods in an alternating left-right pattern [74]), is consistent with this center-of-mass motion. Over longer time scales the cell is unable to maintain a consistent direction during random migration, leading to lowered directional persistence. Additionally, the speed of cells did not depend on the external gradient, indicating that gradient-sensing does not directly drive protrusion. These data provide guidance for modeling *Dictyostelium* motion. Models containing intrinsic motile activity

which is biased by a chemical gradient match well with our data, such as that found by Driscoll et al. [74] or proposed by Insall's 'pseudopod-centric' view of migration [77].

In Chapter 3 we showed that the ability to properly steer cells to an aggregation center is an important effect of collective signal relay. We found that cells are directed towards aggregation centers via signal relay on length scales on the order of millimeters (or even longer), while individual cells have size on order of 10 μm. Without signal relay, even a sustained source that is two orders of magnitude larger than what individual cells can periodically secrete (10 μM versus 100 nM [261]) only caused cells to aggregate over 800 μm. Therefore, signal relay provides amplification to a signal source, and allows a robust response to a large range of initial signal strengths. Not only is the signal relayed, but the direction of the source is also relayed, allowing cells to move toward an aggregation center from great distances.

Signal relay leads to the formation of 'streams', which are head-to-tail chains of migrating cells. Our results indicate that that the mechanical cell-cell interactions due to streaming did not speed them up or increase their directional persistence. Cell motion was essentially the same inside and outside of streams, a finding that can inform streaming models. The rules followed by agent-based models, in which cells are individual deformable objects obeying physical rules, are directly comparable to our findings for cells inside of and outside of streams. Notably, a recent model of *Dictyostelium* aggregation indicated that cell-cell mechanical interactions in the streams should lead to a speeding up of cells inside [96]. Our findings show that this effect does not occur, and that cells inside the stream behave much like cells outside

the stream. One possible change to the model is lowering the cell-cell adhesion force, so that cells behave more like individuals even inside a stream.

Previous work has suggested that cells release cAMP from their posteriors [105], and it is possible that such a localized release would make a difference in the aggregation process. In Chapter 3, we argued based on diffusion that it is plausible that localized release could make a difference on length scales of order 50 μm, which would become apparent when cells are near one another. Combining boundary-tracking methods, such as those of [74], with high-magnification experiments on aggregating cells could show that new protrusions tend to be biased in the direction of the backs of other cells, or toward cell-cell junctions in a stream. If localized signal secretion is found to exist, models of collective motion would again have to be updated to reflect this reality.

5.2.3. Cell-Surface Adhesion

Chapter 4 described experiments in which cell-surface adhesion was varied through changes in surface properties.

We used cells in which actin polymerization was pharmacologically disabled to calculate the adhesion energy of the cell-surface bond for each surface, and we found that the adhesion energies spanned nine orders of magnitude. We investigated the response of individual cells to these surfaces, first by using cells that were genetically modified so as to exert little contractile force. In comparison to cells lacking actin polymerization, these cells showed increased contact area on less adhesive surfaces and equal or less contact area on more adhesive surfaces. This result highlights the

role that actin-based protrusion and cortex stability have in regulating contact with surfaces of very different adhesivities.

Future work could improve on quantifying cell-surface adhesion on various surfaces. Setups currently exist that could conduct these experiments, the simplest being a combination of a microfluidic flow chamber with an inverted microscope [230]. This setup allows for imaging of contact area for a given shear flow, and could test adhesion energies for wild-type cells and other mutants. The adhesion energies for other commonly used surfaces for migration could also be tested, such as plastic or collagen, in order to better understand cell-surface interactions.

Surprisingly, wild-type cells were able to adapt to the different surfaces so as to maintain consistent contact area, speed, and elongation. F-actin staining indicated that this capability was established through adhesion-dependent strengthening of actin polymerization on more adhesive surfaces. This effect should impart mechanical stability to resist spreading as well as an increase in actomyosin-based contractile ability to allow proper regulation of detachment. Combined with findings from Chapter 3, we found that *Dictyostelium* cells have remarkable motile machinery that is able to move under many different conditions, such as high/low adhesive surfaces, weak/strong chemical signals, and inside/outside streams. In fact, recent work by Barry and Bretscher has shown that *Dictyostelium* can even swim [262], indicating that the ability to 'go' remains robust in a wide variety of situations.

We found that cells were able to adjust to a new surface in times on the order of 1 minute. When presented with two different surfaces, they were able to move from less adhesive surfaces to more adhesive ones, and vice versa; however, they displayed

a tendency to move toward the less adhesive surface. In effect, the cells showed a 'preference' for the less adhesive surface. To further elucidate how cells adapt to new surfaces, fluorescently-tagged actin would allow for live-cell imaging, and the kinetics of actin regulation for cells crossing an interface could be found. Another possibility would be to create interfaces between other surfaces, such as BSA and PLL, so that cells would cross between extreme surface adhesivities. This experiment would accentuate the necessary adaptation needed by a cell when crossing to a new surface.

Intriguingly, although individual wild-type cells showed no phenotype on any of the surfaces, populations of aggregating cells did show phenotypic change based on the adhesive properties of the surface. On less adhesive substrates, cells tended to form elongated streams that led to stable aggregation centers; in contrast, cells on more adherent surfaces formed small clumps, and these clumps gradually coalesced into larger and larger aggregates. The final aggregates formed in either case were of similar sizes, indicating the robustness of the process. The fact that the emergent collective behavior depended on an environmental property, but individual behavior did not, is an interesting outcome of how cells regulate their motility.

Results of the cell-surface adhesion studies suggest tests of models of cell motion. In *Dictyostelium*, the characteristic biphasic dependence of speed on adhesion (see Introduction) does not seem to hold, at least for a wide range of adhesion energies. Future models of motion should reproduce the relative independence of the motion cycle on adhesion ability. Similarly, mathematical models of collective *Dictyostelium* motion may need alteration, as they are generally

tuned to produce streaming behavior. It remains to be seen whether the cell-cell to

cell-surface adhesion ratio can be changed to influence the transition between

streaming or clumping aggregation dynamics.

A. Appendix: Experimental and Computational Methods

Portions of this chapter are adapted from [73, 74, 188].

A.1. <u>Experimental Methods</u>

A.1.1. Cell Culture

Wild-type (WT) *Dictyostelium discoideum* (strain AX3), adenylyl cyclase A null (*aca*⁻) mutant cells (in an AX3 background), and myosin-II null cells (*myoII*⁻) (in an Ax3 background) were grown in HL-5 medium in exponential phase to $4\text{-}5*10^6$ cells/ml [263]. For experiments, cells were developed for 4.5 (WT) or 5 hrs (*aca*⁻) in development buffer [pH 6.2] (DB; 5 mM NaH_2PO_4, 2 mM $MgSO_4$, and 0.2 mM $CaCl_2$) at $2*10^7$ cells/ml, with exogenous pulses of 75 nM cAMP every 6 min as previously described [264]. Where specifically mentioned, either a fraction of the cells or all cells were fluorescently labeled by adding 25 µM CellTracker Green CDMFA (Invitrogen) to cells and shaking for 30 min as previously described [265]. Experiments requiring Latrunculin A (Invitrogen) treatment involved resuspending cells in 5 µM Latrunculin A for five minutes before placing them in a chamber, in which the buffer also contained the same concentration of Latrunculin A.

A.1.2. Microscopy

Low-magnification (2.5-10X) cell imaging was performed on a Zeiss Axiovert S100 microscope (Carl Zeiss AG, Oberkochen, Germany) equipped with a CoolSnap

HQ CCD camera (Roper Scientific) and an automated moveable stage, using a 2.5X

(NA 0.075), 5X (NA 0.16), or 10X (NA 0.3) objective. For 4X images a 1.6X optivar

was used with the 2.5X objective. IPLab (Scanalytics, Fairfax, VA) or Axiovision

(Zeiss) software was used to operate the microscope and camera. Fluorescent light

was provided by a FluoArt mercury lamp with appropriate optical filters. Phase-

contrast microscopy was used in all non-fluorescent imaging. Phase-contrast imaging

was adjusted so that objects (cells and streams) appeared bright on a black

background (dark-field microscopy), providing sufficient contrast for automated

tracking routines to easily identify objects. Individual dark-field frames were taken

every 10 seconds for recording individual cell motion metrics, or every 3 minutes for

recording population behaviors, for at least 90 minutes. If fluorescent imaging was

used, an interleaved fluorescent image was captured every 30 seconds.

Interference reflection microscopy (IRM; also known as Reflection

Interference Contrast Microscopy, RICM) is a microscopy technique that indicates

the distance of an object from the surface. As shown in Figure A.1, when a cell is in

close contact with the coverslip, the reflecting light rays interfere destructively,

showing up as a darkened area (see Chapter 4 for sample IRM images). The

grayscale values of the reflections can be used to quantify the distance of the cell

from the coverslip, though that was not done in this thesis. IRM was performed on a

Zeiss Meta 510 microscope with a 40X (NA 1.3) objective. A HeNe laser provided

the excitation line of 488 nm, which was then imaged in three channels: transmitted

light, > 510 nm (for CellTracker or FITC-labeled surface signature) and < 510 nm

(for IRM signature). Images were acquired every 2 or 4 seconds.
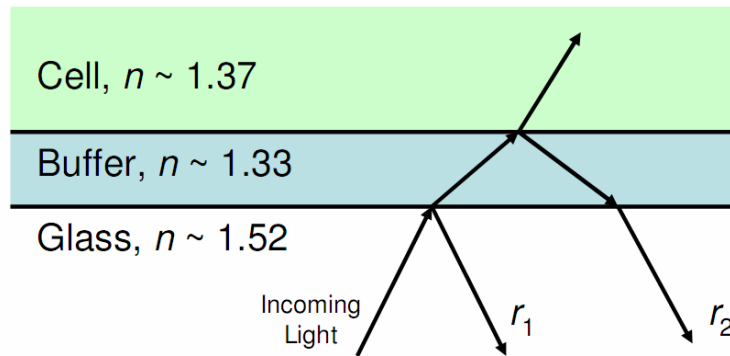
Figure A.1 – Schematic of Interference Reflection Microscopy (IRM)

A light ray enters the sample area from below, where there is a reflection at the glass-buffer interface (r_1). If a cell is present, the incoming light is further reflected at the buffer-cell interface (r_2), and the phase is shifted by 180 degrees. Therefore, when the two reflections interfere, a small glass-cell distance results in nearly perfectly destructive interference, thus darkening areas of close cell-glass contact. The reflected light is collected via a CCD camera. Image adapted from [266]. Note that ray refractions are not to scale.

For contact area and cell polarity experiments, fluorescence, bright-field, and internal reflection microscopy (IRM) images were captured with the same illumination, using the 40× objective, every 2 or 4 seconds. For the remaining experiments, fluorescence images were obtained every 4 seconds.

F-actin labeling experiments were carried out with the following protocol. Cells were fixed by adding 200 μL of 2X fixation stock (4% formaldehyde, 0.4% glutaradehyde, Triton) and 100 μL of 20 μM TRITC phalloidin stock to each well, incubating for 30 minutes under aluminum foil, and rinsing 5 times in PBS buffer (pH 7.2) with Tween 20.

A.1.3.   Surface Preparation

For most experiments Lab-Tek eight-chamber slides (Lab-Tek, Nunc, NY) were used. Each chamber had 400 μL of 1 M HCl placed inside for 15 minutes and were then rinsed three times with deionized water. For Bovine Serum Albumin (BSA) (Sigma) or poly-L-lysine (PLL) (Sigma), 1% w/v solutions were placed inside for four hours. For perfluorinated carbon chain coating (FCC), tridecafluoro-1,1,2,2-tetra hydrooctyl dimethyl chlorosilane (Gelest SIT8170.0) was allowed to vapor deposit on a dry chamber for four hours in an evacuated vacuum chamber. After coating, surfaces were washed three times with deionized water to prepare for use. Static contact angles were measured with 5 μL drops of water with a goniometer. The angles for BSA, glass, Poly-L-Lysine, and FCC were ~10°, 45°, 30°, and 120°, respectively.

For experiments with a glass-poly-L-lysine interface, Lab-Tek two-chamber slides were used. Slides were acid-washed as described above. Ibidi 2-chamber insert with an adhesive bottom (Ibidi, Munchen, Germany) were then placed into dry chambers. One chamber in the insert was filled with 1% w/v FITC-Poly-L-Lysine (Invitrogen) for four hours, aspirated, and then rinsed three times with deionized water. Any surface not immediately used was placed in a 4° Celsius refrigerator for less than three days before use.

A.1.4.   Other Assays

In all experiments, cells were taken from development and centrifuged at 9000 rpm for 4 min using an Eppendorf microfuge. The supernatant was aspirated and the

pellet was washed twice with phosphate buffer (PB; 5 mM Na_2HPO_4, 5 mM

NaH_2PO_4 [pH 6.2]). For density and fluid height self-aggregation studies, cells at the

stated concentration were plated onto Lab-Tek eight-chamber slides (dimensions: 7.5

mm width, 7.5 mm length, 11 mm height) and allowed to adhere for 5 min. A precise

volume of PB was added to achieve the final fluid height. The presence or absence of

streams was scored by identifying head-to-tail chains of several cells (~10) in length.

For micropipette migration assays, cells at a density of ~40 μm between cells (700

cells/mm^2) were plated onto Lab-Tek two-chamber slides, allowed to settle for 5 min,

and 1.5 ml PB was added to reach the final volume. An Eppendorf Femtojet system

(Eppendorf, Hamburg, Germany) was used to continuously release cAMP from a

Femtojet I micropipette at a pressure of 80 hPa as previously described [105]. At the

onset of experiments, a short pulse of high pressure was applied to ensure proper

working of the pipette during the course of the experiment. CellTracker

concentration and light exposure were minimized and the speeds of fluorescent and

non-fluorescent cells in the same experiment were identical (data not shown).

The shaking adhesion assay was performed as follows. 300 μL with 5e5 cells

were allowed to settle in an 8-well Lab-Tek chamber (1 cm^2 surface area) treated with

a given surface coating for 15 minutes. The buffer was replaced to eliminate non-

adherent cells. The cells were then placed on an orbital shaker with a 1 cm radius of

gyration at 200 rpm. After 15 minutes, the buffer was aspirated, and the number of

cells in the supernatant was counted with a hemocytometer. Finally, buffer was

added to the chamber and repeatedly aspirated, and the number of cells in this buffer

was counted with a hemocytometer. The surfaces were visually inspected on a microscopy to ensure that few cells remained after this aspiration.

A.2.   *Computational Methods*

A.2.1.   Gradient-Sensing Model Simulation

The original implementation of the model was programmed using C, but the version presented here was developed using Python. Specifically, FiPy [267], a finite volume partial differential equation solver developed at the National Institute of Standards and Technology (NIST, Gaithersburg, MD), was used for simulations of the system, finding steady-state values, and solving the equations in the presence of the point source stimulus. SciPy [171], an open-source scientific toolkit for Python, was used to find all of the eigenvalues and their corresponding eigenvectors.
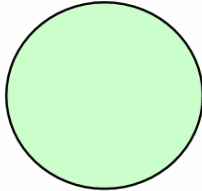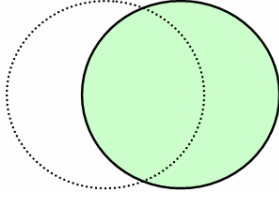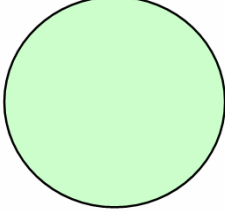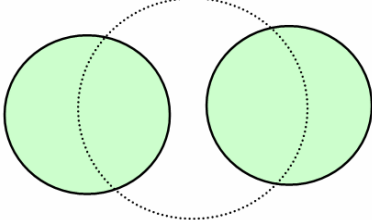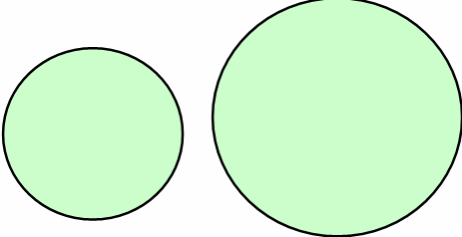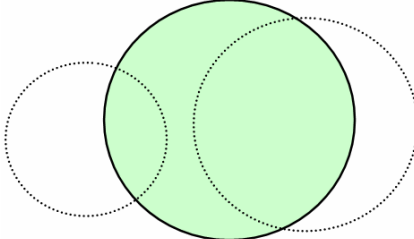
A.2.2.   Center-of-Mass Image Processing and Tracking Algorithm

Images were binarized using ImageJ software [268]. For phase contrast images, the background was subtracted using a rolling ball algorithm and the remaining image thresholded. For fluorescent images, bandpassing and thresholding were performed. To identify the position of cells in each frame and track the motion of fluorescent cells from frame to frame, a publicly available algorithm was used [269]. Identification of cells in phase-contrast images as well as tracking was carried out using custom Matlab code (explained below). This procedure allowed for fully automated cell tracking, as the software kept track of individual cells and only

counted those cells in the statistics that were not part of a larger group. No subjective measures were used to include or exclude specific cells from the population analyses.

In order to track the individual motions of cells in a large population, custom image analysis routines had to be developed, as most standard particle tracking routines fail in this situation. Specifically, cells can deform their shape and merge with other cells, breaking the assumptions held by particle-tracking algorithms. In addition, many of the pre-processing steps (such as bandpass filtering) fail to identify the objects in an image, as cells in streams present objects that can vary in size up to the order of the image size. Therefore, a new method was used, described below and shown in Figure A.2.

In brief, objects of any size greater than a noise threshold (typically on the order of 4 pixels for a low-magnification image) were identified. Objects that overlapped from frame to frame one a one-to-one basis were considered to be the same object. If multiple objects in one frame merged in the next, a merge event was documented, and the number of cells in the resultant object was stored. If one object in a frame split into multiple objects in the subsequent frame, a split event was documented, and the number of cells in the splitting object was stored. If an object was considered to be too large to be a single cell, a guess of the number of cells in that object was stored. By combining data on merges, splits, and sizes in a data set, objects that were individual cells were identified. The center-of-mass translocation data of these objects were the only ones used in generating statistics of single cells.

Frame N	Frame N+1	Event
		Motion
		Split
		Merge

Figure A.2 – Explanation of the Cell Tracking Algorithm

Illustration of the cell tracking algorithm. The position of an object in frame N (left; shown in green) is compared to the overlapping objects in frame N+1 (right; shown in green; object in frame N is shown in dotted outline). If one object overlaps (top row), then the object has moved. If an object is now overlapped by two (middle row), then a split occurred, and we mark the original object as a group (i.e. composed of more than one cell). If two objects are now overlapped by one (bottom row), a merge occurred, and we mark the new object as a group.

A.2.3.   Cell Metrics

Cell centroids were calculated by finding the center-of-mass of individual objects in the binarized images. These positions were then smoothed using a 3-frame (30 sec) unweighted sliding window – a time that corresponds to a distance of about 1.5 pixel (at 4X magnification), comparable to the uncertainty of our tracking algorithm at this lowest resolution (see below).   For fluorescent images, no smoothing was performed, as the time between frames was already 30 secs.

Velocities were determined by finding the displacement between smoothed center positions in each frame: $\vec{u}_i(t,i) = \vec{x}_i(t) - \vec{x}_i(t-\Delta t)$, where $\vec{x}_i(t)$ is the smoothed centroid of cell i at time t, and Δt is the time between frames. Velocity was only counted in averages during a timeframe in which cells had a net displacement of 20 μm over a 5 min period. This procedure reduced noise and eliminated the contribution of cells that essentially moved in place. After a non-fluorescent cell touched another cell or entered a stream it was ignored, and speeds of streams or other cell groups were not computed. Errors in finding cell centers are presumed to be ≤ 1 pixel in x and y, and therefore overall $\delta\vec{x} \leq 1.4$ pixels. This distance corresponds to less than 4.4 μm (at 4X magnification), 3.5 μm (5X), or 1.8 μm (10X). Using smoothed centers presumably reduced this uncertainty further.

The mean squared displacement (MSD) gives a measure for the type of motion displayed by cells, and is computed as $\text{MSD}(\tau) = \langle \vec{x}_i(t) - \vec{x}_i(t-\tau) \rangle_{t,i}$, where the brackets indicate averages over all times t and all cells i. Unlike the calculation of velocities, cells were only counted if they had a net displacement of 20 μm over the entire cell track. Otherwise, the (stricter) criteria used in calculating velocity introduced an artificial persistence over short timescales. We also note that MSDs that were smaller than the noise value, considered to be one pixel, were ignored. The MSD values were assumed to locally take the form $\text{MSD}(\tau) = C * \tau^\alpha$. The exponent α gives the information about the type of motion that the cell displays: $\alpha=1$ defines diffusive motion, $1<\alpha<2$ is superdiffusive motion, and $\alpha=2$ is straight-line motion.

The instantaneous chemotactic index (CI) for cell i at time t is defined as

$CI(t,i) = [\vec{u}_i(t) \circ \hat{r}_i(t)]/|\vec{u}_i(t)| = \cos[\theta_i(t)]$, where $\hat{r}_i(t)$ is the unit direction vector from

cell i to the pipette at time t and $\theta_i(t)$ is the angle between cell i's motion vector at

time t and the vector pointing to the pipette. With this definition, CI = 1 means a cell

is moving directly towards the pipette, CI = 0 means a cell is moving perpendicular to

the direction to the pipette, and CI = −1 means a cell is moving directly away from

the pipette.

Signal recruitment range for non-streaming cells was computed by first binning

the instantaneous CI of cells in all frames based on distance from the pipette. These

indices were then averaged for each bin. When the average CI for a bin was above a

certain threshold (0.1), that bin was considered to be directed toward the pipette. The

distance from the pipette to the farthest bin above the threshold was considered to be

the 'signal range' of the pipette.

Polarization, a measure of object elongation, is given by

$$\varepsilon = \frac{P^2}{4\pi A} \qquad\qquad (A.1)$$

where P is the object perimeter and A is the object area. This definition of ε means

that polarization is 1 for a circle and greater than 1 for other objects, with larger

values corresponding to more elongated objects.

A.2.4.　　　Use of Algorithms

This section explains the use of the tracking software developed during the research presented in this thesis. Note that the software package itself comes with a README.TXT file that contains much of the following information, and each function's usage and logic is commented inside each function file. This software was developed to be run on MATLAB, a matrix-based scientific computing programming language. All software runs on version R2009a (and potentially older versions) and requires the 'Image Analysis' toolbox. **Note that all functions listed below have a very thorough commented header explaining their use.** Type 'help (function)' or 'doc (function)' at the MATLAB command line to view these comments.

PIV capabilities require the mpiv toolbox to be in a subdirectory called 'mpiv'. This toolbox requires access to the DACE tools. The mpiv toolbox can be found here: http://www.oceanwave.jp/softwares/mpiv/.

Running the analysis suite (specifically, the file 'makeInitialize.m') creates a directory structure, where each subdirectory contains organized files corresponding to each function's output. This output can then later be retrieved by the user (so that the function does not have to be run again) and is used automatically by subsequent functions. Specifically, the directory structure is the following:

'Image Directory': the directory containing the original images

'Image Directory/data': directory containing MATLAB-readable files written by each function

'Image Directory/figures': directory containing MATLAB figures written by functions that generate plots

'Image Directory/movies': contains JPEG-compressed or uncompressed AVI files written by functions that generate movies

'Image Directory/temp': contains temporary files that are deleted when read

A.2.4.1   Quick Start: Go from Images to Single Cell Statistics

1. Convert your images to WHITE cells on a BLACK background (using ImageJ or another program). Save these files as individually named UNCOMPRESSED files (e.g. 'tif' files) in a directory.

2. In MATLAB, change to the directory with all the Cell Tracking program files.

3. Edit 'defaultParameters.m' (e.g. type 'open defaultParameters.m') and make sure

     --->   baseDirectory = 'Your Directory Here';

     --->   parameterSet = 1;

     Then save the file.

4. At the MATLAB prompt, type

     ---> makeInitialize;

Follow the on-screen commands. If you do not know the pixel size or frame rate, just type '1' for those values and remember that they are in pixels and frames!

5. At the MATLAB prompt, type

     ---> makeRegions;

6. At the MATLAB prompt, type

     ---> makeTracks;

7. At the MATLAB prompt, type

---> makeVelocities;

Follow the on-screen commands. I recommend a smoothing window of 3.

8. At the MATLAB prompt, type

---> plotVelocityStatistics;

Follow the on-screen prompts and you're done!

To make a movie with your tracks, type

---> plotTracksMovie

from the command prompt. Follow the on-screen instructions!

To make the data from a figure into a Microsoft Excel (tm) readable file, click on the figure, then type

---> dumpFigureToExcel

which will create a file that Excel (tm) can open.

A.2.4.2   A More Thorough Explanation

Here is a list of all the functions available. **Every function marked with a bullet requires that all previous bulleted functions have been run. All functions marked with a check require that all previous bulleted (but not checked) functions have been run.**

FOR SINGLE CELL TRACKS:

- Edit 'defaultParameters' to set up the image directory and the parameter set number. This must be properly done before running ANY of the programs below.

- Run 'makeInitialize' to interactively set up the analysis process.

- Run 'makeRegions' to threshold and find objects in the original image sequence.

- Run 'makeTracks' to identify cells by joining the objects from frame to frame to create cell tracks. If interrupted, run with second argument as 'true' to resume tracking where it left off. ALTERNATIVE: run 'makeManualTracks' to identify tracks by hand. Does not identify groups. ALTERNATIVE: run 'makeSimpleTracks' for sparsely-populated data that move a lot from frame to frame. Does not identify groups.

  - ✓ Run 'plotTracksMovie' to make a movie showing the cells and all the tracks

  - ✓ Run 'plotSingleTracksMovie' to make a movie showing single cells' motion

  - ✓ Run 'plotTracksDiagram' to make a figure showing all single tracks starting from the origin

  - ✓ Run 'plotMSDs' to show MSD and logarithmic derivative (alpha) values for the tracks.

  - ✓ Run 'findTrackedDensity' to find the number of cells and surface density in a given frame

- Run 'makeVelocities' to smooth position information and calculate velocities

  - ✓ Run 'plotVelocityStatistics' to plot all sorts of information about the cell population

✓ Run 'plotGradientStatistics' to see how well cells move up an IMAGED gradient.

✓ Run 'plotSingleStatistics' to plot statistics for individual cells.

- Run 'makeTrackSync' to synchronize a brightfield and fluorescent data set

FOR CELL FIELDS USING PIV (Particle Image Velocimetry):

- Edit 'defaultPIVParameters' to set up the image directory and the parameter set number. This must be properly done before running ANY of the programs below.

- Run 'makePIVInitialize' to interactively set up the analysis process.

- Run 'makePIV' to run the PIV. This may take a while...

✓ Run 'plotPIVMovie' to make a movie with the PIV overlaid on the original images.

✓ Run 'plotPIVCI' to find the chemotactic index of the cell field

MISCELLANEOUS FILES:

Run 'findUntrackedDensity' to find the cell density in an image. A rough estimate, at best.

A.2.4.3   File-by-file Explanation

THE MEANING OF NAMES:

o do_____.m -> generally an internal function, not for external use.

o make_____.m -> does grunt work of doing the basic image analysis and setting up variables

o find_____.m -> will do some sort of analysis that gives a single-line answer

o plot_____.m -> does more advanced analysis, plots and saves the results (as well as the plots)

o qad_____.m -> stands for 'quick and dirty', is a one-shot (temporary) file doing some analysis quickly. Untested, undocumented

o recover_____.m -> for manual-input programs, this picks up if the process was interrupted.

o view_____.m -> view the output of a 'make' function. Doesn't necessarily save anything.

ALPHABETICAL LIST OF FUNCTIONS

o doGetGoodTracks - return a list of tracks that matches user-specified criteria

o doGradientCenter - prompt the user to identify sources of chemoattractant.

o doInsideROI - takes an ROI and tracks, and returns the rows that are inside the ROI

o doMSD - returns the MSD and MSD log-log slopes for a set of input tracks

o doPlotError - takes a structure and performs errorbar() on various values of that structure

o doPlotLog - takes a structure and performs loglog() on various values of that structure

o doPlotStats - takes a structure and performs plot() on various values of that structure

- doRegions - takes a grayscale image and ROI and return an appropriately thresholded image

- doROI - return a user-selected Region of Interest (ROI)

- findTrackedDensity - finds the cell surface density in a particular frame

- findUntrackedDensity - takes an image file, binarizes it, and guesses at the cell surface density

- InvertIm - inverts an arbitrary image. Written by Stead Kiger - see the HELP for this funciton.

- makeInitialize - begins the analysis process and sets up the subdirectory structure

- makeManualTracks - make cell tracks, by hand. Requires patience and perseverance, and does not identify groups.

- makePIV - does the grunt work of making velocity matrices from input images.

- makePIVInitialize - begins the analysis process and sets up the subdirectory strucutre

- makeRegions - makes thresholded images from the input images

- makeSimpleTracks - makes tracks by combinatorially matching region centers. Use for sparsely populated images.

- makeTracks - identifies cells, groups, numbers in each group, etc. The main workhorse. Can also resume if interrupted.

- makeTrackSync - synchronize a brightfield and fluorescent data set

- makeVelocities - takes track position information and calculates velocities

- plotMSDs - plots MSD and the logarithmic derivative (alpha) for a set of tracks

- plotPIVCI - analyzes the PIV movie in the context of cells moving up a chemoattractant gradient

- plotPIVMovie - makas a movie overlaying the PIV analysis on top of the original data

- plotSingleStatistics - plots statistics of individual cells.

- plotSingleTracksMovie   - plots zoomed-in movie of single tracks

- plotTracksDiagram - makes a plot showing the tracks of all cells, where each cell starts at the origin

- plotTracksMovie - make a movie of moving cells. All sorts of settable options.

- plotVelocityStatistics - plots various statistics of a cell population

- track - Implementation of Weeks's tracking algorithm. See file for contact info and other information.

Bibliography

1. Moussaid, M., Garnier, S., Theraulaz, G., and Helbing, D. (2009). Collective Information Processing and Pattern Formation in Swarms, Flocks, and Crowds. Topics in Cognitive Science *1*, 469-497.

2. Vicsek, T., and Zafiris, A. (2010). Collective Motion. arXiv:1010.5017v1.

3. Romanczuk, P., Couzin, I.D., and Schimansky-Geier, L. (2009). Collective motion due to individual escape and pursuit response. Phys Rev Lett *102*, 010602.

4. Ward, A.J., Sumpter, D.J., Couzin, I.D., Hart, P.J., and Krause, J. (2008). Quorum decision-making facilitates information transfer in fish shoals. Proc Natl Acad Sci U S A *105*, 6948-6953.

5. Sárová, R., Spinka, M., Panamá, J.L.A., and Simecek, P. Graded leadership by dominant animals in a herd of female beef cattle on pasture. Animal Behaviour *79*, 1037-1045.

6. Dyer, J.R., Johansson, A., Helbing, D., Couzin, I.D., and Krause, J. (2009). Leadership, consensus decision making and collective behaviour in humans. Philos Trans R Soc Lond B Biol Sci *364*, 781-789.

7. Dorigo, M., Birattari, M., Di Caro, G., Doursat, R., Engelbrecht, A., Floreano, D., Gambardella, L., Groß, R., Sahin, E., Sayama, H., et al. (2010). Opinion Dynamics for Decentralized Decision-Making in a Robot Swarm. In Swarm Intelligence, Volume 6234. (Springer Berlin / Heidelberg), pp. 251-262-262.

8. Couzin, I.D. (2009). Collective cognition in animal groups. Trends Cogn Sci *13*, 36-43.

9. Couzin, I.D., Krause, J., Franks, N.R., and Levin, S.A. (2005). Effective leadership and decision-making in animal groups on the move. Nature *433*, 513-516.

10. Sokolov, A., Goldstein, R.E., Feldchtein, F.I., and Aranson, I.S. (2009). Enhanced mixing and spatial instability in concentrated bacterial suspensions. Phys Rev E Stat Nonlin Soft Matter Phys *80*, 031903.

11. Bindschadler, M., and McGrath, J.L. (2007). Sheet migration by wounded monolayers as an emergent property of single-cell dynamics. J Cell Sci *120*, 876-884.

12. Rorth, P. (2009). Collective cell migration. Annu Rev Cell Dev Biol *25*, 407-429.

13. Bagorda, A., and Parent, C.A. (2008). Eukaryotic chemotaxis at a glance. J Cell Sci *121*, 2621-2624.

14. Deisboeck, T.S., and Couzin, I.D. (2009). Collective behavior in cancer cell populations. BioEssays *31*, 190-197.

15. Friedl, P., and Gilmour, D. (2009). Collective cell migration in morphogenesis, regeneration and cancer. Nat Rev Mol Cell Biol *10*, 445-457.

16. Gaggioli, C., Hooper, S., Hidalgo-Carcedo, C., Grosse, R., Marshall, J.F., Harrington, K., and Sahai, E. (2007). Fibroblast-led collective invasion of carcinoma cells with differing roles for RhoGTPases in leading and following cells. Nat Cell Biol *9*, 1392--1400.

17. Vitorino, P., Hammer, M., Kim, J., and Meyer, T. (2011). A steering model of endothelial sheet migration recapitulates monolayer integrity and directed collective migration. Mol Cell Biol *31*, 342-350.

18. de Kievit, T.R., and Iglewski, B.H. (2000). Bacterial quorum sensing in pathogenic relationships. Infect Immun *68*, 4839-4849.

19. Jin, H., and Varner, J. (2004). Integrins: roles in cancer development and as treatment targets. Br J Cancer *90*, 561-565.

20. Friedl, P., Hegerfeldt, Y., and Tusch, M. (2004). Collective cell migration in morphogenesis and cancer. Int J Dev Biol *48*, 441--449.

21. Sokolov, A., Aranson, I.S., Kessler, J.O., and Goldstein, R.E. (2007). Concentration dependence of the collective dynamics of swimming bacteria. Phys Rev Lett *98*, 158102.

22. Wilson, P.A., and Melton, D.A. (1994). Mesodermal patterning by an inducer gradient depends on secondary cell-cell communication. Curr Biol *4*, 676-686.

23. Cohen, M.H., and Robertson, A. (1971). Chemotaxis and the early stages of aggregation in cellular slime molds. J Theor Biol *31*, 119-130.

24. Swaney, K.F., Huang, C.H., and Devreotes, P.N. (2010). Eukaryotic chemotaxis: a network of signaling pathways controls motility, directional sensing, and polarity. Annu Rev Biophys *39*, 265-289.

25. Iglesias, P.A., and Devreotes, P.N. (2008). Navigating through models of chemotaxis. Curr Opin Cell Biol *20*, 35-40.

26. Alberts, B., Johnson, A., Lewis, J., Raff, M., Roberts, K., and Walter, P. eds. (2007). Molecular Biology of the Cell, 5th Edition, 5 Edition.

27. Llopis, J., McCaffery, J.M., Miyawaki, A., Farquhar, M.G., and Tsien, R.Y. (1998). Measurement of cytosolic, mitochondrial, and Golgi pH in single living cells with green fluorescent proteins. Proc Natl Acad Sci U S A *95*, 6803-6808.

28. Howard, J. (2001). Mechanics of Motor Proteins and the Cytoskeleton, (Sinauer Associates).

29. Heit, B., Tavener, S., Raharjo, E., and Kubes, P. (2002). An intracellular signaling hierarchy determines direction of migration in opposing chemotactic gradients. J Cell Biol *159*, 91-102.

30. Macnab, R.M., and Koshland, D.E., Jr. (1972). The gradient-sensing mechanism in bacterial chemotaxis. Proc Natl Acad Sci U S A *69*, 2509-2512.

31. Tsang, N., Macnab, R., and Koshland, D.E., Jr. (1973). Common mechanism for repellents and attractants in bacterial chemotaxis. Science *181*, 60-63.

32. Endres, R.G., and Wingreen, N.S. (2008). Accuracy of direct gradient sensing by single cells. Proc Natl Acad Sci U S A *105*, 15749-15754.

33. Ridley, A.J., Schwartz, M.A., Burridge, K., Firtel, R.A., Ginsberg, M.H., Borisy, G., Parsons, J.T., and Horwitz, A.R. (2003). Cell migration: integrating signals from front to back. Science *302*, 1704--1709.

34. Song, L., Nadkarni, S.M., Bodeker, H.U., Beta, C., Bae, A., Franck, C., Rappel, W.J., Loomis, W.F., and Bodenschatz, E. (2006). Dictyostelium discoideum chemotaxis: threshold for directed motion. Eur J Cell Biol *85*, 981-989.

35. Skupsky, R. (2005). Distinguishing Modes of Eukaryotic Gradient Sensing. PhD Thesis. (College Park, Maryland: University of Maryland).

36. Eagle, H. (1955). Nutrition needs of mammalian cells in tissue culture. Science *122*, 501-514.

37. Geiger, J., Wessels, D., and Soll, D.R. (2003). Human polymorphonuclear leukocytes respond to waves of chemoattractant, like Dictyostelium. Cell Motil Cytoskeleton *56*, 27-44.

38.   Wang, F., Herzmark, P., Weiner, O.D., Srinivasan, S., Servant, G., and Bourne, H.R. (2002). Lipid products of PI(3)Ks maintain persistent cell polarity and directed motility in neutrophils. Nat Cell Biol *4*, 513--518.

39.   Annesley, S.J., and Fisher, P.R. (2009). Dictyostelium discoideum--a model for many reasons. Mol Cell Biochem *329*, 73-91.

40.   Kessin, R.H. (2010). Dictyostelium: Evolution, Cell Biology, and the Development of Multicellularity, (Cambridge University Press).

41.   King, J.S., and Insall, R.H. (2009). Chemotaxis: finding the way forward with Dictyostelium. Trends Cell Biol *19*, 523-530.

42.   van Haastert, P.J., De Wit, R.J., and Konijn, T.M. (1982). Antagonists of chemoattractants reveal separate receptors for cAMP, folic acid and pterin in Dictyostelium. Exp Cell Res *140*, 453-456.

43.   Eichinger, L., Pachebat, J.A., Glockner, G., Rajandream, M.A., Sucgang, R., Berriman, M., Song, J., Olsen, R., Szafranski, K., Xu, Q., et al. (2005). The genome of the social amoeba Dictyostelium discoideum. Nature *435*, 43-57.

44.   Yarger, J., Stults, K., and Soll, D.R. (1974). Observations on the growth of Dictyostelium discoideum in axenic medium: evidence for an extracellular growth inhibitor synthesized by stationary phase cells. J Cell Sci *14*, 681-690.

45.   Varnum, B., Edwards, K.B., and Soll, D.R. (1986). The developmental regulation of single-cell motility in Dictyostelium discoideum. Dev Biol *113*, 218-227.

46.   Lippincott-Schwartz, J., and Patterson, G.H. (2003). Development and Use of Fluorescent Protein Markers in Living Cells. Science *300*, 87-91.

47.   Zimmer, M. (2009). GFP: from jellyfish to the Nobel prize and beyond. Chem Soc Rev *38*, 2823-2832.

48.   Prasher, D.C. (1995). Using GFP to see the light. Trends Genet *11*, 320-323.

49.   Parent, C.A., and Devreotes, P.N. (1999). A cell's sense of direction. Science *284*, 765--770.

50.   Parent, C.A., Blacklock, B.J., Froehlich, W.M., Murphy, D.B., and Devreotes, P.N. (1998). G protein signaling events are activated at the leading edge of chemotactic cells. Cell *95*, 81-91.

51.   Xu, X., Meier-Schellersheim, M., Jiao, X., Nelson, L.E., and Jin, T. (2005). Quantitative imaging of single live cells reveals spatiotemporal dynamics of

multistep signaling events of chemoattractant gradient sensing in Dictyostelium. Mol Biol Cell *16*, 676--688 (http://www.molbiolcell.org/cgi/content/abstract/616/672/676).

52.   Janetopoulos, C., Ma, L., Devreotes, P.N., and Iglesias, P.A. (2004). Chemoattractant-induced phosphatidylinositol 3,4,5-trisphosphate accumulation is spatially amplified and adapts, independent of the actin cytoskeleton. Proc Natl Acad Sci U S A *101*, 8951--8956.

53.   Meinhardt, H. (1999). Orientation of chemotactic cells and growth cones: models and mechanisms. J Cell Sci *112 (Pt 17)*, 2867-2874.

54.   Manahan, C.L., Iglesias, P.A., Long, Y., and Devreotes, P.N. (2004). Chemoattractant signaling in dictyostelium discoideum. Annu Rev Cell Dev Biol *20*, 223-253.

55.   Iijima, M., and Devreotes, P. (2002). Tumor suppressor PTEN mediates sensing of chemoattractant gradients. Cell *109*, 599--610.

56.   Devreotes, P., and Janetopoulos, C. (2003). Eukaryotic chemotaxis: distinctions between directional sensing and polarization. J Biol Chem *278*, 20445-20448.

57.   Huang, Y.E., Iijima, M., Parent, C.A., Funamoto, S., Firtel, R.A., and Devreotes, P. (2003). Receptor-mediated regulation of PI3Ks confines PI(3,4,5)P3 to the leading edge of chemotaxing cells. Mol Biol Cell *14*, 1913-1922.

58.   Insall, R., and Andrew, N. (2007). Chemotaxis in Dictyostelium: how to walk straight using parallel pathways. Curr Opin Microbiol *10*, 578--581.

59.   Rericha, E.C., and Parent, C.A. (2008). Steering in quadruplet: the complex signaling pathways directing chemotaxis. Sci Signal *1*, pe26.

60.   Stephens, L., Milne, L., and Hawkins, P. (2008). Moving towards a better understanding of chemotaxis. Curr Biol *18*, R485--R494.

61.   Veltman, D.M., and van Haastert, P.J. (2008). The role of cGMP and the rear of the cell in Dictyostelium chemotaxis and cell streaming. J Cell Sci *121*, 120-127.

62.   King, J.S., and Insall, R.H. (2008). Chemotaxis: TorC before you Akt. Curr Biol *18*, R864-866.

63.   Hoeller, O., and Kay, R.R. (2007). Chemotaxis in the absence of PIP3 gradients. Curr Biol *17*, 813--817.

64.   Janetopoulos, C., and Firtel, R.A. (2008). Directional sensing during chemotaxis. FEBS Lett *582*, 2075-2085.

65.   Weiner, O.D. (2002). Regulation of cell polarity during eukaryotic chemotaxis: the chemotactic compass. Curr Opin Cell Biol *14*, 196-202.

66.   Meyers, J., Craig, J., and Odde, D.J. (2006). Potential for control of signaling pathways via cell size and shape. Curr Biol *16*, 1685--1693.

67.   Devreotes, P.N., and Zigmond, S.H. (1988). Chemotaxis in eukaryotic cells: a focus on leukocytes and Dictyostelium. Annu Rev Cell Biol *4*, 649-686.

68.   Segel, L.A., Goldbeter, A., Devreotes, P.N., and Knox, B.E. (1986). A mechanism for exact sensory adaptation based on receptor modification. J Theor Biol *120*, 151-179.

69.   Skupsky, R., Losert, W., and Nossal, R.J. (2005). Distinguishing modes of eukaryotic gradient sensing. Biophys J *89*, 2806--2823.

70.   Narang, A., Subramanian, K.K., and Lauffenburger, D.A. (2001). A mathematical model for chemoattractant gradient sensing based on receptor-regulated membrane phospholipid signaling dynamics. Ann Biomed Eng *29*, 677-691.

71.   Levine, H., Kessler, D.A., and Rappel, W.J. (2006). Directional sensing in eukaryotic chemotaxis: a balanced inactivation model. Proc Natl Acad Sci U S A *103*, 9761-9766.

72.   Xiong, Y., Huang, C.H., Iglesias, P.A., and Devreotes, P.N. (2010). Cells navigate with a local-excitation, global-inhibition-biased excitable network. Proc Natl Acad Sci U S A *107*, 17079-17086.

73.   Skupsky, R., McCann, C., Nossal, R., and Losert, W. (2007). Bias in the gradient-sensing response of chemotactic cells. J Theor Biol *247*, 242--258.

74.   Driscoll, M., McCann, C.P., Kopace, R., Homan, T., Fourkas, J., Parent, C.A., and Losert, W. (2011). Cell Shape Dynamics: From Waves to Migration. Submitted.

75.   Arai, Y., Shibata, T., Matsuoka, S., Sato, M.J., Yanagida, T., and Ueda, M. (2010). Self-organization of the phosphatidylinositol lipids signaling system for random cell migration. Proc Natl Acad Sci U S A *107*, 12399-12404.

76. Schroth-Diez, B., Gerwig, S., Ecke, M., Hegerl, R., Diez, S., and Gerisch, G. (2009). Propagating waves separate two states of actin organization in living cells. HFSP J *3*, 412-427.

77. Insall, R.H. (2010). Understanding eukaryotic chemotaxis: a pseudopod-centred view. Nat Rev Mol Cell Biol *11*, 453-458.

78. Heinrich, D., Youssef, S., Schroth-Diez, B., Engel, U., Aydin, D., Blummel, J., Spatz, J.P., and Gerisch, G. (2008). Actin-cytoskeleton dynamics in non-monotonic cell spreading. Cell Adh Migr *2*, 58-68.

79. Beta, C. (2010). Bistability in the actin cortex. PMC Biophys *3*, 12.

80. Dormann, D., Libotte, T., Weijer, C.J., and Bretschneider, T. (2002). Simultaneous quantification of cell motility and protein-membrane-association using active contours. Cell Motil Cytoskeleton *52*, 221--230.

81. Mahadeo, D.C., and Parent, C.A. (2006). Signal relay during the life cycle of Dictyostelium. Curr Top Dev Biol *73*, 115-140.

82. Brazill, D.T., Gundersen, R., and Gomer, R.H. (1997). A cell-density sensing factor regulates the lifetime of a chemoattractant-induced G alpha-GTP conformation. FEBS Lett *404*, 100--104.

83. Gregor, T., Fujimoto, K., Masaki, N., and Sawai, S. (2010). The onset of collective behavior in social amoebae. Science *328*, 1021-1025.

84. Devreotes, P. (1989). Dictyostelium discoideum: a model system for cell-cell interactions in development. Science *245*, 1054-1058.

85. Tomchik, K.J., and Devreotes, P.N. (1981). Adenosine 3',5'-monophosphate waves in Dictyostelium discoideum: a demonstration by isotope dilution--fluorography. Science *212*, 443--446.

86. Roisin-Bouffay, C., Jang, W., Caprette, D.R., and Gomer, R.H. (2000). A precise group size in Dictyostelium is generated by a cell-counting factor modulating cell-cell adhesion. Mol Cell *6*, 953--959.

87. Gomer, R.H. (2001). Not being the wrong size. Nat Rev Mol Cell Biol *2*, 48-54.

88. Umeda, T. (1989). A mathematical model for cell sorting, migration and shape in the slug stage of *Dictyostelium discoideum*. Bulletin of Mathematical Biology *51*, 485-500-500.

89.   Hofer, T., Sherratt, J.A., and Maini, P.K. (1995). Dictyostelium discoideum: cellular self-organization in an excitable biological medium. Proc Biol Sci *259*, 249-257.

90.   Goldstein, R.E. (1996). Traveling-Wave Chemotaxis. Phys Rev Lett *77*, 775-778.

91.   Savill, N.J., and Hogeweg, P. (1997). Modelling Morphogenesis: From Single Cells to Crawling Slugs. Journal of Theoretical Biology *184*, 229-235.

92.   Alber, M., Chen, N., Lushnikov, P.M., and Newman, S.A. (2007). Continuous macroscopic limit of a discrete stochastic model for interaction of living cells. Phys Rev Lett *99*, 168102.

93.   Levine, H. (1994). Modeling spatial patterns in Dictyostelium. Chaos *4*, 563--568.

94.   Levine, H., Tsimring, L., and Kessler, D. (1997). Computational modeling of mound development in Dictyostelium. Physica D: Nonlinear Phenomena *106*, 375-388.

95.   Dallon, J.C., and Othmer, H.G. (2004). How cellular movement determines the collective force generated by the Dictyostelium discoideum slug. J Theor Biol *231*, 203-222.

96.   Palsson, E., and Othmer, H.G. (2000). A model for individual and collective cell movement in Dictyostelium discoideum. Proc Natl Acad Sci U S A *97*, 10448--10453.

97.   van Oss, C., Panfilov, A.V., Hogeweg, P., Siegert, F., and Weijer, C.J. (1996). Spatial pattern formation during aggregation of the slime mould Dictyostelium discoideum. J Theor Biol *181*, 203--213.

98.   Kessler, and Levine (1993). Pattern formation in Dictyostelium via the dynamics of cooperative biological entities. Phys Rev E Stat Phys Plasmas Fluids Relat Interdiscip Topics *48*, 4801--4804.

99.   Höfer, T., Sherratt, J.A., and Maini, P.K. (1995). Cellular pattern formation during Dictyostelium aggregation. Physica D: Nonlinear Phenomena *85*, 425-444.

100.   Rappel, W.-J., Nicol, A., Sarkissian, A., Levine, H., and Loomis, W.F. (1999). Self-organized Vortex State in Two-Dimensional Dictyostelium Dynamics. Physical Review Letters *83*, 1247 [http://link.aps.org/doi/1210.1103/PhysRevLett.1283.1247].

101. Palsson, E. (2008). A 3-D model used to explore how cell adhesion and stiffness affect cell sorting and movement in multicellular systems. J Theor Biol *254*, 1-13.

102. Dallon, J.C., and Othmer, H.G. (1997). A discrete cell model with adaptive signalling for aggregation of Dictyostelium discoideum. Philos Trans R Soc Lond B Biol Sci *352*, 391--417.

103. Levine, H., and Reynolds, W. (1991). Streaming instability of aggregating slime mold amoebae. Phys Rev Lett *66*, 2400--2403.

104. Vicker, M.G., and Grutsch, J.F. (2008). Dual chemotaxis signalling regulates Dictyostelium development: intercellular cyclic AMP pulses and intracellular F-actin disassembly waves induce each other. Eur J Cell Biol *87*, 845-861.

105. Kriebel, P.W., Barr, V.A., and Parent, C.A. (2003). Adenylyl cyclase localization regulates streaming during chemotaxis. Cell *112*, 549-560.

106. Kriebel, P.W., Barr, V.A., Rericha, E.C., Zhang, G., and Parent, C.A. (2008). Collective cell migration requires vesicular trafficking for chemoattractant delivery at the trailing edge. J Cell Biol *183*, 949-961.

107. Siegert, F., and Weijer, C.J. (1991). Analysis of optical density wave propagation and cell movement in the cellular slime mould Dictyostelium discoideum. Physica D: Nonlinear Phenomena *49*, 224-232.

108. Postma, M., and van Haastert, P.J. (2009). Mathematics of experimentally generated chemoattractant gradients. Methods Mol Biol *571*, 473-488.

109. Skoge, M., Adler, M., Groisman, A., Levine, H., Loomis, W.F., and Rappel, W.J. (2010). Gradient sensing in defined chemotactic fields. Integr Biol (Camb) *2*, 659-668.

110. van Haastert, P.J., and Postma, M. (2007). Biased random walk by stochastic fluctuations of chemoattractant-receptor interactions at the lower limit of detection. Biophys J *93*, 1787-1796.

111. Dallon, J.C., and Othmer, H.G. (1998). A continuum analysis of the chemotactic signal seen by Dictyostelium discoideum. J Theor Biol *194*, 461-483.

112. Hilgardt, C., Cejkova, J., Hauser, M.J., and Sevcikova, H. (2008). Streamless aggregation of Dictyostelium in the presence of isopropylidenadenosin. Biophys Chem *132*, 9-17.

113.   Engler, A.J., Sen, S., Sweeney, H.L., and Discher, D.E. (2006). Matrix elasticity directs stem cell lineage specification. Cell *126*, 677-689.

114.   Stroka, K.M., and Aranda-Espinoza, H. (2009). Neutrophils display biphasic relationship between migration and substrate stiffness. Cell Motil Cytoskeleton *66*, 328-341.

115.   Saneinejad, S., and Shoichet, M.S. (1998). Patterned glass surfaces direct cell adhesion and process outgrowth of primary neurons of the central nervous system. J Biomed Mater Res *42*, 13-19.

116.   Buenemann, M., Levine, H., Rappel, W.J., and Sander, L.M. (2010). The role of cell contraction and adhesion in dictyostelium motility. Biophys J *99*, 50-58.

117.   Friedl, P., Borgmann, S., and Brocker, E.B. (2001). Amoeboid leukocyte crawling through extracellular matrix: lessons from the Dictyostelium paradigm of cell movement. J Leukoc Biol *70*, 491-509.

118.   Renkawitz, J., Schumann, K., Weber, M., Lammermann, T., Pflicke, H., Piel, M., Polleux, J., Spatz, J.P., and Sixt, M. (2009). Adaptive force transmission in amoeboid cell migration. Nat Cell Biol *11*, 1438-1443.

119.   Jay, P.Y., Pham, P.A., Wong, S.A., and Elson, E.L. (1995). A mechanical function of myosin II in cell motility. J Cell Sci *108 (Pt 1)*, 387-393.

120.   Gallant, N.D., and Garcia, A.J. (2007). Quantitative analyses of cell adhesion strength. Methods Mol Biol *370*, 83-96.

121.   Cornillon, S., Gebbie, L., Benghezal, M., Nair, P., Keller, S., Wehrle-Haller, B., Charette, S.J., Bruckert, F., Letourneur, F., and Cosson, P. (2006). An adhesion molecule in free-living Dictyostelium amoebae with integrin beta features. EMBO Rep *7*, 617-621.

122.   Fey, P., Stephens, S., Titus, M.A., and Chisholm, R.L. (2002). SadA, a novel adhesion receptor in Dictyostelium. J Cell Biol *159*, 1109-1119.

123.   Benghezal, M., Cornillon, S., Gebbie, L., Alibaud, L., Bruckert, F., Letourneur, F., and Cosson, P. (2003). Synergistic control of cellular adhesion by transmembrane 9 proteins. Mol Biol Cell *14*, 2890-2899.

124.   Owens, N.F., Gingell, D., and Trommler, A. (1988). Cell adhesion to hydroxyl groups of a monolayer film. J Cell Sci *91 (Pt 2)*, 269-279.

125. Socol, M., Lefrou, C., Bruckert, F., Delabouglise, D., and Weidenhaupt, M. (2010). Synchronization of Dictyostelium discoideum adhesion and spreading using electrostatic forces. Bioelectrochemistry *79*, 198-210.

126. Cornillon, S., Froquet, R., and Cosson, P. (2008). Involvement of Sib proteins in the regulation of cellular adhesion in Dictyostelium discoideum. Eukaryot Cell *7*, 1600-1605.

127. Uchida, K.S., and Yumura, S. (2004). Dynamics of novel feet of Dictyostelium cells during migration. J Cell Sci *117*, 1443-1455.

128. Abedin, M., and King, N. (2010). Diverse evolutionary paths to cell adhesion. Trends Cell Biol *20*, 734-742.

129. Siu, C.-H., Harris, T.J.C., Wang, J., and Wong, E. (2004). Regulation of cell-cell adhesion during Dictyostelium development. Semin Cell Dev Biol *15*, 633--641.

130. Siu, C.H., and Kamboj, R.K. (1990). Cell-cell adhesion and morphogenesis in Dictyostelium discoideum. Dev Genet *11*, 377-387.

131. Bozzaro, S., and Ponte, E. (1995). Cell adhesion in the life cycle of Dictyostelium. Experientia *51*, 1175-1188.

132. Sesaki, H., and Siu, C.H. (1996). Novel redistribution of the Ca(2+)-dependent cell adhesion molecule DdCAD-1 during development of Dictyostelium discoideum. Dev Biol *177*, 504-516.

133. Ponte, E., Bracco, E., Faix, J., and Bozzaro, S. (1998). Detection of subtle phenotypes: the case of the cell adhesion molecule csA in Dictyostelium. Proc Natl Acad Sci U S A *95*, 9360-9365.

134. Meili, R., Alonso-Latorre, B., del Alamo, J.C., Firtel, R.A., and Lasheras, J.C. (2010). Myosin II is essential for the spatiotemporal organization of traction forces during cell motility. Mol Biol Cell *21*, 405-417.

135. Del Alamo, J.C., Meili, R., Alonso-Latorre, B., Rodriguez-Rodriguez, J., Aliseda, A., Firtel, R.A., and Lasheras, J.C. (2007). Spatio-temporal analysis of eukaryotic cell motility by improved force cytometry. Proc Natl Acad Sci U S A *104*, 13343-13348.

136. Niewohner, J., Weber, I., Maniak, M., Muller-Taubenberger, A., and Gerisch, G. (1997). Talin-null cells of Dictyostelium are strongly defective in adhesion to particle and substrate surfaces and slightly impaired in cytokinesis. J Cell Biol *138*, 349-361.

137. Schindl, M., Wallraff, E., Deubzer, B., Witke, W., Gerisch, G., and Sackmann, E. (1995). Cell-substrate interactions and locomotion of Dictyostelium wild-type and mutants defective in three cytoskeletal proteins: a study using quantitative reflection interference contrast microscopy. Biophys J *68*, 1177-1190.

138. Weber, I., Wallraff, E., Albrecht, R., and Gerisch, G. (1995). Motility and substratum adhesion of Dictyostelium wild-type and cytoskeletal mutant cells: a study by RICM/bright-field double-view image analysis. J Cell Sci *108 (Pt 4)*, 1519-1530.

139. Noegel, A.A., and Schleicher, M. (2000). The actin cytoskeleton of Dictyostelium: a story told by mutants. J Cell Sci *113 (Pt 5)*, 759-766.

140. Weber, I., Niewohner, J., and Faix, J. (1999). Cytoskeletal protein mutations and cell motility in Dictyostelium. Biochem Soc Symp *65*, 245-265.

141. DiMilla, P.A., Barbee, K., and Lauffenburger, D.A. (1991). Mathematical model for the effects of adhesion and mechanics on cell migration speed. Biophys J *60*, 15-37.

142. Nossal, R., and Zigmond, S.H. (1976). Chemotropism indices for polymorphonuclear leukocytes. Biophys J *16*, 1171-1182.

143. Firtel, R.A., and Meili, R. (2000). Dictyostelium: a model for regulated cell movement during morphogenesis. Curr Opin Genet Dev *10*, 421-427.

144. Isbister, C.M., Mackenzie, P.J., To, K.C., and O'Connor, T.P. (2003). Gradient steepness influences the pathfinding decisions of neuronal growth cones in vivo. J Neurosci *23*, 193-202.

145. Olson, T.S., and Ley, K. (2002). Chemokines and chemokine receptors in leukocyte trafficking. Am J Physiol Regul Integr Comp Physiol *283*, R7-28.

146. Yang, X., Dormann, D., Munsterberg, A.E., and Weijer, C.J. (2002). Cell movement patterns during gastrulation in the chick are controlled by positive and negative chemotaxis mediated by FGF4 and FGF8. Dev Cell *3*, 425-437.

147. Zeller, P.J., Skalak, T.C., Ponce, A.M., and Price, R.J. (2001). In vivo chemotactic properties and spatial expression of PDGF in developing mesenteric microvascular networks. Am J Physiol Heart Circ Physiol *280*, H2116-2125.

148. Devreotes, P.N., and Zigmond, S.H. (1988). Chemotaxis in eukaryotic cells: a focus on leukocytes and Dictyostelium. Annu Rev Cell Biol *4*, 649--686.

149.   Fisher, P.R., Merkl, R., and Gerisch, G. (1989). Quantitative analysis of cell motility and chemotaxis in Dictyostelium discoideum by using an image processing system and a novel chemotaxis chamber providing stationary chemical gradients. J Cell Biol *108*, 973--984.

150.   Jin, T., Zhang, N., Long, Y., Parent, C.A., and Devreotes, P.N. (2000). Localization of the G protein betagamma complex in living cells during chemotaxis. Science *287*, 1034--1036.

151.   Moghe, P.V., and Tranquillo, R.T. (1994). Stochastic model of chemoattractant receptor dynamics in leukocyte chemosensory movement. Bull Math Biol *56*, 1041-1093.

152.   Iijima, M., Huang, Y.E., and Devreotes, P. (2002). Temporal and spatial regulation of chemotaxis. Dev Cell *3*, 469--478.

153.   Levchenko, A., and Iglesias, P.A. (2002). Models of eukaryotic gradient sensing: application to chemotaxis of amoebae and neutrophils. Biophys J *82*, 50-63.

154.   Ma, L., Janetopoulos, C., Yang, L., Devreotes, P.N., and Iglesias, P.A. (2004). Two complementary, local excitation, global inhibition mechanisms acting in parallel can explain the chemoattractant-induced regulation of PI(3,4,5)P3 response in dictyostelium cells. Biophys J *87*, 3764-3774.

155.   Postma, M., and Van Haastert, P.J. (2001). A diffusion-translocation model for gradient sensing by chemotactic cells. Biophys J *81*, 1314-1323.

156.   Rappel, W.J., Thomas, P.J., Levine, H., and Loomis, W.F. (2002). Establishing direction during chemotaxis in eukaryotic cells. Biophys J *83*, 1361-1367.

157.   Subramanian, K.K., and Narang, A. (2004). A mechanistic model for eukaryotic gradient sensing: spontaneous and induced phosphoinositide polarization. J Theor Biol *231*, 49--67.

158.   Gamba, A., de Candia, A., Di Talia, S., Coniglio, A., Bussolino, F., and Serini, G. (2005). Diffusion-limited phase separation in eukaryotic chemotaxis. Proc Natl Acad Sci U S A *102*, 16927-16932.

159.   Levine, H., Kessler, D.A., and Rappel, W.-J. (2006). Directional sensing in eukaryotic chemotaxis: a balanced inactivation model. Proc Natl Acad Sci U S A *103*, 9761--9766.

160.   Zigmond, S.H. (1974). Mechanisms of sensing chemical gradients by polymorphonuclear leukocytes. Nature *249*, 450-452.

161. Weiner, O.D., Neilsen, P.O., Prestwich, G.D., Kirschner, M.W., Cantley, L.C., and Bourne, H.R. (2002). A PtdInsP(3)- and Rho GTPase-mediated positive feedback loop regulates neutrophil polarity. Nat Cell Biol *4*, 509-513.

162. Czupalla, C., Culo, M., Muller, E.C., Brock, C., Reusch, H.P., Spicher, K., Krause, E., and Nurnberg, B. (2003). Identification and characterization of the autophosphorylation sites of phosphoinositide 3-kinase isoforms beta and gamma. J Biol Chem *278*, 11536-11545.

163. Vazquez, F., Ramaswamy, S., Nakamura, N., and Sellers, W.R. (2000). Phosphorylation of the PTEN tail regulates protein stability and function. Mol Cell Biol *20*, 5010-5018.

164. Brock, C., Schaefer, M., Reusch, H.P., Czupalla, C., Michalke, M., Spicher, K., Schultz, G., and Nurnberg, B. (2003). Roles of G beta gamma in membrane recruitment and activation of p110 gamma/p101 phosphoinositide 3-kinase gamma. J Cell Biol *160*, 89-99.

165. Vanhaesebroeck, B., Leevers, S.J., Ahmadi, K., Timms, J., Katso, R., Driscoll, P.C., Woscholski, R., Parker, P.J., and Waterfield, M.D. (2001). Synthesis and function of 3-phosphorylated inositol lipids. Annu Rev Biochem *70*, 535-602.

166. Welch, H.C., Coadwell, W.J., Stephens, L.R., and Hawkins, P.T. (2003). Phosphoinositide 3-kinase-dependent activation of Rac. FEBS Lett *546*, 93-97.

167. Jackson, T.R., Kearns, B.G., and Theibert, A.B. (2000). Cytohesins and centaurins: mediators of PI 3-kinase-regulated Arf signaling. Trends Biochem Sci *25*, 489-495.

168. Comer, F.I., and Parent, C.A. (2002). PI 3-kinases and PTEN: how opposites chemoattract. Cell *109*, 541--544.

169. Funamoto, S., Meili, R., Lee, S., Parry, L., and Firtel, R.A. (2002). Spatial and temporal regulation of 3-phosphoinositides by PI 3-kinase and PTEN mediates chemotaxis. Cell *109*, 611-623.

170. Janetopoulos, C., Jin, T., and Devreotes, P. (2001). Receptor-mediated activation of heterotrimeric G-proteins in living cells. Science *291*, 2408-2411.

171. Jones, E., Oliphant, T., Peterson, P., and Others (2001-). SciPy: Open Source Scientific Tools for Python.

172. Cross, M.C., and Hohenberg, P.C. (1993). Pattern formation outside of equilibrium. Reviews of Modern Physics *65*, 851.

173. Turing, A.M. (1952). The Chemical Basis of Morphogenesis. Philosophical Transactions of the Royal Society of London. Series B, Biological Sciences *237*, 37-72.

174. Satnoianu, R.A., Menzinger, M., and Maini, P.K. (2000). Turing instabilities in general systems. J Math Biol *41*, 493-512.

175. Levine, H., and Rappel, W.-J. (2005). Membrane-bound Turing patterns. Phys Rev E Stat Nonlin Soft Matter Phys *72*, 061912.

176. Meinhardt, H., and Gierer, A. (2000). Pattern formation by local self-activation and lateral inhibition. Bioessays *22*, 753-760.

177. Foxman, E.F., Campbell, J.J., and Butcher, E.C. (1997). Multistep navigation and the combinatorial control of leukocyte chemotaxis. J Cell Biol *139*, 1349-1360.

178. Tranquillo, R.T., Lauffenburger, D.A., and Zigmond, S.H. (1988). A stochastic model for leukocyte random motility and chemotaxis based on receptor binding fluctuations. J Cell Biol *106*, 303--309.

179. Korohoda, W., Madeja, Z., and Sroka, J. (2002). Diverse chemotactic responses of Dictyostelium discoideum amoebae in the developing (temporal) and stationary (spatial) concentration gradients of folic acid, cAMP, Ca(2+) and Mg(2+). Cell Motil Cytoskeleton *53*, 1-25.

180. Killich, T., Plath, P.J., Wei, X., Bultmann, H., Rensing, L., and Vicker, M.G. (1993). The locomotion, shape and pseudopodial dynamics of unstimulated Dictyostelium cells are not random. J Cell Sci *106 (Pt 4)*, 1005-1013.

181. Janmey, P.A. (1998). The cytoskeleton and cell signaling: component localization and mechanical coupling. Physiol Rev *78*, 763-781.

182. Xu, J., Wang, F., Van Keymeulen, A., Herzmark, P., Straight, A., Kelly, K., Takuwa, Y., Sugimoto, N., Mitchison, T., and Bourne, H.R. (2003). Divergent signals and cytoskeletal assemblies regulate self-organizing polarity in neutrophils. Cell *114*, 201-214.

183. Eddy, R.J., Pierini, L.M., and Maxfield, F.R. (2002). Microtubule asymmetry during neutrophil polarization and migration. Mol Biol Cell *13*, 4470-4483.

184. Mullins, R.D., Heuser, J.A., and Pollard, T.D. (1998). The interaction of Arp2/3 complex with actin: nucleation, high affinity pointed end capping, and

formation of branching networks of filaments. Proc Natl Acad Sci U S A *95*, 6181-6186.

185. Svitkina, T.M., and Borisy, G.G. (1999). Arp2/3 complex and actin depolymerizing factor/cofilin in dendritic organization and treadmilling of actin filament array in lamellipodia. J Cell Biol *145*, 1009-1026.

186. Ali, H., Richardson, R.M., Tomhave, E.D., Didsbury, J.R., and Snyderman, R. (1993). Differences in phosphorylation of formylpeptide and C5a chemoattractant receptors correlate with differences in desensitization. J Biol Chem *268*, 24247-24254.

187. Samadani, A., Mettetal, J., and van Oudenaarden, A. (2006). Cellular asymmetry and individuality in directional sensing. Proc Natl Acad Sci U S A *103*, 11549--11554.

188. McCann, C.P., Kriebel, P.W., Parent, C.A., and Losert, W. (2010). Cell speed, persistence and information transmission during signal relay and collective migration. J Cell Sci *123*, 1724-1731.

189. Bagorda, A., Mihaylov, V.A., and Parent, C.A. (2006). Chemotaxis: moving forward and holding on to the past. Thromb Haemost *95*, 12-21.

190. Garcia, G.L., and Parent, C.A. (2008). Signal relay during chemotaxis. J Microsc *231*, 529-534.

191. Weijer, C.J. (2009). Collective cell migration in development. J Cell Sci *122*, 3215-3223.

192. Franca-Koh, J., Kamimura, Y., and Devreotes, P. (2006). Navigating signaling networks: chemotaxis in Dictyostelium discoideum. Curr Opin Genet Dev *16*, 333--338.

193. Kimmel, A.R., and Parent, C.A. (2003). The signal to move: D. discoideum go orienteering. Science *300*, 1525--1527.

194. Cohen, M.H., and Robertson, A. (1971). Wave propagation in the early stages of aggregation of cellular slime molds. J Theor Biol *31*, 101-118.

195. Hashimoto, Y., Cohen, M.H., and Robertson, A. (1975). Cell density dependence of the aggregation characteristics of the cellular slime mould Dictyostelium discoideum. J Cell Sci *19*, 215-229.

196. Gingle, A.R. (1976). Critical density for relaying in Dictyostelium discoideum and its relation to phosphodiesterase secretion into the extracellular medium. J Cell Sci *20*, 1--20.

197.	Raman, R.K., Hashimoto, Y., Cohen, M.H., and Robertson, A. (1976). Differentiation for aggregation in the cellular slime moulds: the emergence of autonomously signalling cells in Dictyostelium discoideum. J Cell Sci *21*, 243-259.

198.	Weijer, C.J. (2004). Dictyostelium morphogenesis. Curr Opin Genet Dev *14*, 392--398.

199.	Postma, M., Roelofs, J., Goedhart, J., Gadella, T.W., Visser, A.J., and Van Haastert, P.J. (2003). Uniform cAMP stimulation of Dictyostelium cells induces localized patches of signal transduction and pseudopodia. Mol Biol Cell *14*, 5019-5027.

200.	Postma, M., Roelofs, J., Goedhart, J., Loovers, H.M., Visser, A.J., and Van Haastert, P.J. (2004). Sensitization of Dictyostelium chemotaxis by phosphoinositide-3-kinase-mediated self-organizing signalling patches. J Cell Sci *117*, 2925-2935.

201.	Li, L., Driscoll, M., Kumi, G., Hernandez, R., Gaskell, K.J., Losert, W., and Fourkas, J.T. (2008). Binary and gray-scale patterning of chemical functionality on polymer films. J Am Chem Soc *130*, 13512-13513.

202.	Andrew, N., and Insall, R.H. (2007). Chemotaxis in shallow gradients is mediated independently of PtdIns 3-kinase by biased choices between random protrusions. Nat Cell Biol *9*, 193-200.

203.	Bosgraaf, L., and Van Haastert, P.J. (2010). Quimp3, an automated pseudopod-tracking algorithm. Cell Adh Migr *4*, 46-55.

204.	Gomer, R.H., Yuen, I.S., and Firtel, R.A. (1991). A secreted 80 x 10(3) Mr protein mediates sensing of cell density and the onset of development in Dictyostelium. Development *112*, 269--278.

205.	Dworkin, M., and Keller, K.H. (1977). Solubility and diffusion coefficient of adenosine 3':5'-monophosphate. J Biol Chem *252*, 864-865.

206.	Gao, T., Ehrenman, K., Tang, L., Leippe, M., Brock, D.A., and Gomer, R.H. (2002). Cells respond to and bind countin, a component of a multisubunit cell number counting factor. J Biol Chem *277*, 32596--32605.

207.	Franke, J., and Kessin, R.H. (1992). The cyclic nucleotide phosphodiesterases of Dictyostelium discoideum: molecular genetics and biochemistry. Cell Signal *4*, 471-478.

208. Conkling, B.L., and Blanchar, R.W. (1986). Estimation of Calcium Diffusion Coefficients from Electrical Conductance. Soil Sci Soc Am J *50*, 1455-1459.

209. Pitt, G.S., Milona, N., Borleis, J., Lin, K.C., Reed, R.R., and Devreotes, P.N. (1992). Structurally distinct and stage-specific adenylyl cyclase genes play different roles in Dictyostelium development. Cell *69*, 305-315.

210. Takagi, H., Sato, M.J., Yanagida, T., and Ueda, M. (2008). Functional analysis of spontaneous cell movement under different physiological conditions. PLoS One *3*, e2648.

211. Li, L., Norrelykke, S.F., and Cox, E.C. (2008). Persistent cell motion in the absence of external signals: a search strategy for eukaryotic cells. PLoS One *3*, e2093.

212. Selmeczi, D., Li, L., Pedersen, L.I.I., Nrrelykke, S.F., Hagedorn, P.H., Mosler, S., Larsen, N.B., Cox, E.C., and Flyvbjerg, H. (2008). Cell motility as random motion: A review. The European Physical Journal - Special Topics *157*, 1-15-15.

213. Dieterich, P., Klages, R., Preuss, R., and Schwab, A. (2008). Anomalous dynamics of cell migration. Proceedings of the National Academy of Sciences of the United States of America *105*, 459-463.

214. Palsson, E., Lee, K.J., Goldstein, R.E., Franke, J., Kessin, R.H., and Cox, E.C. (1997). Selection for spiral waves in the social amoebae Dictyostelium. Proc Natl Acad Sci U S A *94*, 13719-13723.

215. Dormann, D., Vasiev, B., and Weijer, C.J. (2002). Becoming Multicellular by Aggregation; The Morphogenesis of the Social Amoebae Dicyostelium discoideum. Journal of Biological Physics *28*, 765-780-780.

216. Gruver, J.S., Wikswo, J.P., and Chung, C.Y. (2008). 3'-phosphoinositides regulate the coordination of speed and accuracy during chemotaxis. Biophys J *95*, 4057-4067.

217. Rietdorf, J., Siegert, F., and Weijer, C.J. (1996). Analysis of optical density wave propagation and cell movement during mound formation in Dictyostelium discoideum. Dev Biol *177*, 427-438.

218. Fisher, P.R. (1990). Pseudopodium activation and inhibition signals in chemotaxis by Dictyostelium discoideum amoebae. Semin Cell Biol *1*, 87-97.

219. Arrieumerlou, C., and Meyer, T. (2005). A local coupling model and compass parameter for eukaryotic chemotaxis. Dev Cell *8*, 215-227.

220. Soll, D.R., Wessels, D., Heid, P.J., and Zhang, H. (2002). A contextual framework for characterizing motility and chemotaxis mutants in Dictyostelium discoideum. J Muscle Res Cell Motil *23*, 659--672.

221. Bowers-Morrow, V.M., Ali, S.O., and Williams, K.L. (2004). Comparison of molecular mechanisms mediating cell contact phenomena in model developmental systems: an exploration of universality. Biol Rev Camb Philos Soc *79*, 611-642.

222. McCann, C.P., Rericha, E.R., Losert, W., and Parent, C.A. (In Preparation). Impact of Surface Adhesiveness on Amoeboid Adhesion, Migration, and Aggregation Patterns.

223. Lammermann, T., and Sixt, M. (2009). Mechanical modes of 'amoeboid' cell migration. Curr Opin Cell Biol *21*, 636-644.

224. Ananthakrishnan, R., and Ehrlicher, A. (2007). The forces behind cell movement. Int J Biol Sci *3*, 303-317.

225. Lunt, S.J., Chaudary, N., and Hill, R.P. (2009). The tumor microenvironment and metastatic disease. Clin Exp Metastasis *26*, 19-34.

226. Renkawitz, J., and Sixt, M. (2010). Mechanisms of force generation and force transmission during interstitial leukocyte migration. EMBO Rep *11*, 744-750.

227. Soon, L.L. (2007). A discourse on cancer cell chemotaxis: where to from here? IUBMB Life *59*, 60-67.

228. Ponte, E., Rivero, F., Fechheimer, M., Noegel, A., and Bozzaro, S. (2000). Severe developmental defects in Dictyostelium null mutants for actin-binding proteins. Mech Dev *91*, 153-161.

229. Lauffenburger, D. (1989). A simple model for the effects of receptor-mediated cell--substratum adhesion on cell migration. Chemical Engineering Science *44*, 1903-1914.

230. Simson, R., Wallraff, E., Faix, J., Niewohner, J., Gerisch, G., and Sackmann, E. (1998). Membrane bending modulus and adhesion energy of wild-type and mutant cells of Dictyostelium lacking talin or cortexillins. Biophys J *74*, 514-522.

231. Bhattacharya, S., Datta, A., Berg, J.M., and Gangopadhyay, S. (2005). Studies on surface wettability of poly(dimethyl) siloxane (PDMS) and glass under oxygen-plasma treatment and correlation with bond strength. Microelectromechanical Systems, Journal of *14*, 590-597.

232. Lombardi, M.L., Knecht, D.A., and Lee, J. (2008). Mechano-chemical signaling maintains the rapid movement of Dictyostelium cells. Exp Cell Res *314*, 1850-1859.

233. Cooper, K.M., Bennin, D.A., and Huttenlocher, A. (2008). The PCH family member proline-serine-threonine phosphatase-interacting protein 1 targets to the leukocyte uropod and regulates directed cell migration. Mol Biol Cell *19*, 3180-3191.

234. Van Dulm, P., and Norde, W. (1983). The adsorption of human plasma albumin on solid surfaces, with special attention to the kinetic aspects. Journal of Colloid and Interface Science *91*, 248-255.

235. Kowalczynska, H.M., Nowak-Wyrzykowska, M., Szczepankiewicz, A.A., Dobkowski, J., Dyda, M., Kaminski, J., and Kolos, R. Albumin adsorption on unmodified and sulfonated polystyrene surfaces, in relation to cell-substratum adhesion. Colloids and Surfaces B: Biointerfaces *84*, 536-544.

236. Marks, P.W., Hendey, B., and Maxfield, F.R. (1991). Attachment to fibronectin or vitronectin makes human neutrophil migration sensitive to alterations in cytosolic free calcium concentration. The Journal of Cell Biology *112*, 149-158.

237. Wessels, D., Vawter-Hugart, H., Murray, J., and Soll, D.R. (1994). Three-dimensional dynamics of pseudopod formation and the regulation of turning during the motility cycle of Dictyostelium. Cell Motil Cytoskeleton *27*, 1--12.

238. Thomas, N.E., and Coakley, W.T. (1995). Localized contact formation by erythrocyte membranes: electrostatic effects. Biophys J *69*, 1387-1401.

239. Jaszewski, R.W., Schift, H., Schnyder, B., Schneuwly, A., and Gröning, P. (1999). The deposition of anti-adhesive ultra-thin teflon-like films and their interaction with polymers during hot embossing. Applied Surface Science *143*, 301-308.

240. Wischerhoff, E., Uhlig, K., Lankenau, A., Borner, H.G., Laschewsky, A., Duschl, C., and Lutz, J.F. (2008). Controlled cell adhesion on PEG-based switchable surfaces. Angew Chem Int Ed Engl *47*, 5666-5668.

241. Zigmond, S.H. (1993). Recent quantitative studies of actin filament turnover during cell locomotion. Cell Motil Cytoskeleton *25*, 309-316.

242. Ayscough, K.R., Stryker, J., Pokala, N., Sanders, M., Crews, P., and Drubin, D.G. (1997). High rates of actin filament turnover in budding yeast and roles for actin in establishment and maintenance of cell polarity revealed using the actin inhibitor latrunculin-A. J Cell Biol *137*, 399-416.

243. Evans, E., and Rawicz, W. (1990). Entropy-driven tension and bending elasticity in condensed-fluid membranes. Phys Rev Lett *64*, 2094-2097.

244. Kramer, R.H., McDonald, K.A., Crowley, E., Ramos, D.M., and Damsky, C.H. (1989). Melanoma cell adhesion to basement membrane mediated by integrin-related complexes. Cancer Res *49*, 393-402.

245. Wilkemeyer, M.F., Sebastian, A.B., Smith, S.A., and Charness, M.E. (2000). Antagonists of alcohol inhibition of cell adhesion. Proc Natl Acad Sci U S A *97*, 3690-3695.

246. Bukharova, T., Weijer, G., Bosgraaf, L., Dormann, D., van Haastert, P.J., and Weijer, C.J. (2005). Paxillin is required for cell-substrate adhesion, cell sorting and slug migration during Dictyostelium development. J Cell Sci *118*, 4295-4310.

247. Murrell, M., Pontani, L.L., Guevorkian, K., Cuvelier, D., Nassoy, P., and Sykes, C. (2011). Spreading dynamics of biomimetic actin cortices. Biophys J *100*, 1400-1409.

248. Neumann, A.K., Itano, M.S., and Jacobson, K. Understanding lipid rafts and other related membrane domains. F1000 Biol Rep *2*, 31.

249. Baumgart, T., Hess, S.T., and Webb, W.W. (2003). Imaging coexisting fluid domains in biomembrane models coupling curvature and line tension. Nature *425*, 821-824.

250. Disanza, A., and Scita, G. (2008). Cytoskeletal regulation: coordinating actin and microtubule dynamics in membrane trafficking. Curr Biol *18*, R873-875.

251. Hamill, O.P., and Martinac, B. (2001). Molecular Basis of Mechanotransduction in Living Cells. Physiological Reviews *81*, 685-740.

252. Bruckert, F., Decave, E., Garrivier, D., Cosson, P., Brechet, Y., Fourcade, B., and Satre, M. (2002). Dictyostelium discoideum adhesion and motility under shear flow: experimental and theoretical approaches. J Muscle Res Cell Motil *23*, 651-658.

253. Chaudhuri, O., Parekh, S.H., Lam, W.A., and Fletcher, D.A. (2009). Combined atomic force microscopy and side-view optical imaging for mechanical studies of cells. Nat Methods *6*, 383-387.

254. Keren, K., Pincus, Z., Allen, G.M., Barnhart, E.L., Marriott, G., Mogilner, A., and Theriot, J.A. (2008). Mechanism of shape determination in motile cells. Nature *453*, 475-480.

255. de la Roche, M.A., and Cote, G.P. (2001). Regulation of Dictyostelium myosin I and II. Biochim Biophys Acta *1525*, 245-261.

256. Butt, H.-J., Graf, K., and Kappl, M. (2003). Physics and Chemistry of Interfaces, (Berlin: WILEY-VCH).

257. Fischer, R.S., Gardel, M., Ma, X., Adelstein, R.S., and Waterman, C.M. (2009). Local Cortical Tension by Myosin II Guides 3D Endothelial Cell Branching. Current Biology *19*, 260-265.

258. Fukui, Y., Murray, J., Riddelle, K.S., and Soll, D.R. (1991). Cell behavior and actomyosin organization in Dictyostelium during substrate exploration. Cell Struct Funct *16*, 289-301.

259. Graf, R., Rietdorf, J., and Zimmermann, T. (2005). Live cell spinning disk microscopy. Adv Biochem Eng Biotechnol *95*, 57-75.

260. Wu, Y.I., Frey, D., Lungu, O.I., Jaehrig, A., Schlichting, I., Kuhlman, B., and Hahn, K.M. (2009). A genetically encoded photoactivatable Rac controls the motility of living cells. Nature *461*, 104-108.

261. Martiel, J.L., and Goldbeter, A. (1987). A Model Based on Receptor Desensitization for Cyclic AMP Signaling in Dictyostelium Cells. Biophys J *52*, 807-828.

262. Barry, N.P., and Bretscher, M.S. (2010). Dictyostelium amoebae and neutrophils can swim. Proc Natl Acad Sci U S A *107*, 11376-11380.

263. Sussman, M. (1987). Cultivation and synchronous morphogenesis of Dictyostelium under controlled experimental conditions. Methods Cell Biol *28*, 9-29.

264. Devreotes, P., Fontana, D., Klein, P., Sherring, J., and Theibert, A. (1987). Transmembrane signaling in Dictyostelium. Methods Cell Biol *28*, 299-331.

265. Dormann, D., and Weijer, C.J. (2006). Chemotactic cell movement during Dictyostelium development and gastrulation. Curr Opin Genet Dev *16*, 367--373.

266. Barr, V.A., and Bunnell, S.C. (2009). Interference reflection microscopy. Curr Protoc Cell Biol *Chapter 4*, Unit 4 23.

267. Guyer, J.E., Wheeler, D., and Warren, J.A. (2009). FiPy: Partial Differential Equations with Python. Computing in Science *&* Engineering *11*, 6-15.

268.   Rasband, W.S. (2009). ImageJ. (Bethesda, MD, USA: National Institutes of Health).

269.   Blair, D., and Dufresne, E. (2008). The Matlab Particle Tracking Code Repository.